A multiwavelength follow-up study of the enigmatic 3C 220.3 lensed system

A senior thesis presented by

Sóley Ósk Hyman

to the Department of Astronomy

in partial fulfillment of the requirements for the

degree of Bachelor of Arts

Harvard College

12 April 2019

ABSTRACT

During a 2012 survey with the *Herschel Space Observatory*, the radio galaxy 3C 220.3 ($z = 0.685$) was discovered to be gravitationally lensing a submillimeter galaxy (SMG) at a redshift of $z = 2.221$. Initial lens models indicated that 3C 220.3 (source A) is part of a double-lens system with a third object of unknown redshift (source B). Since then, deeper data from the *Chandra X-Ray Observatory* and the *Hubble Space Telescope* (*HST*) have been obtained, showing diffuse X-ray emission and a full Einstein ring in the optical/infrared bands. Using the new three-color *HST* data, we report updated stellar masses for sources A and B ($M_A^* \sim \left(1.1^{+17}_{-0.17}\right) \times 10^{10} M_\odot$ and $M_B^* \sim \left(5.4^{+90}_{-1.1}\right) \times 10^9 M_\odot$), restframe blackbody temperatures for sources A and B and the SMG ($T_{A,\mathrm{rest}} \sim 4430$ K, $T_{B,\mathrm{rest}} \sim 4340$ K, and $T_{\mathrm{SMG,rest}} \sim 8570$ K), and preliminary dark matter fractions for sources A and B ($f_A \sim 0.97^{+0.01}_{-0.48}$ and $f_B \sim 0.96^{+0.01}_{-0.75}$). We also report the first measurements of the internal magnetic fields of 3C 220.3's radio lobes, which have strengths of approximately $1.5 - 3$ nT. These values are a factor of $\sim 2 - 3$ below the strengths of the corresponding equipartition field. Updated lens modeling using the more recent *Chandra* and *HST* data is forthcoming and will generate a new reconstruction of the SMG and provide improved total masses for dark matter fraction estimations.

ACKNOWLEDGEMENTS

First and foremost, I would like to thank my thesis advisor, Dr. Belinda Wilkes, for her unparalleled mentoring and the countless hours she has spent guiding me through this thesis. Many thanks also to the others in her group, Drs. Joanna Kuraszkiewicz and Mojegan Azadi, for teaching me how to use the BEHR and FAST programs and for their help throughout the research process, my readers Drs. Jonathan McDowell and Aneta Siemiginowska for their thoughtful and thorough comments, and Dr. Dave Charbonneau and the rest of the Astronomy 99 class for their feedback throughout this year.

Contents

LIST OF ABBREVIATIONS

3C: Third Cambridge Catalogue of Radio Sources

3CR: Revised Third Cambridge Catalogue of Radio Sources

ACIS: Advanced CCD Imaging Spectrometer

AGN: active galactic nucleus/nuclei

AO: adaptive optics

ARF: ancillary response file

BEHR: Bayesian Estimation of Hardness Ratios

BLR: broad-line region

BLRG: broad-line radio galaxy

CARMA: Combined Array for Research in Millimeter Astronomy

CIAO: *Chandra* Interactive Analysis of Observations

CXC: *Chandra* X-Ray Center

DDT: Director's Discretionary Time

FAST: Fitting and Assessment of Synthetic Templates

FIR: far-infrared

FR I/II: Faranoff and Riley Class I/II

HETG: High Energy Transmission Grating

HR: hardness ratio

HSO: *Herschel Space Observatory*

HST: *Hubble Space Telescope*

IGM: intergalactic medium

IMF: initial mass function

IR: infrared

IRAC: Infrared Array Camera

ISM: interstellar medium

JVLA: Jansky Very Large Array

LGS: laser guide star

MIPS: Multiband Imaging Photometer

NIRC2: Near Infrared Camera 2

NGS: natural guide star

NLR: narrow-line region

NLRG: narrow-line radio galaxy

PACS: Photodetector Array Camera and Spectrometer

PIMMS: Portable, Interactive Multi-Mission Simulator

POG: Proposers' Observatory Guide

PRG: powerful radio galaxy

QSO: quasi-stellar object

QSR: quasi-stellar radio source

RA: right ascension

RMF: redistribution matrix file

SED: spectral energy distribution

SFH: star formation history

SFR: star formation rate

SMBH: supermassive black hole

SMG: submillimeter galaxy

SMA: Submillimeter Array

SPIRE: Spectral and Photometric Imaging Receiver

SSP: single-stellar population

UV: ultraviolet

WFC3: Wide-Field Camera 3

WFPC2: Wide-Field Planetary Camera 2

1. INTRODUCTION

NOT FAR FROM THE NORTH STAR, just over six billion light years from Earth,[1] lies the radio galaxy 3C 220.3. With a mass of almost one billion times that of our Sun (Westhues et al. 2016), the black hole at the center of 3C 220.3 is actively devouring nearby matter and spewing resulting radiation far outside its host galaxy along relativistic jets.

A little over four billion light years farther beyond and almost directly behind 3C 220.3, lies the galaxy SMMJ0939+8315 (Haas et al. 2014) (which we will refer to as SMMJ0939). A member of a relatively rare and elusive type of galaxy called submillimeter galaxies (SMGs), SMMJ0939 belongs to the earlier universe and may contain clues about galaxy evolution and star formation at that time. While SMGs like SMMJ0939 are typically difficult to detect due to their distance, a phenomenon known as gravitational lensing has caused a magnified (albeit distorted) image of SMMJ0939 (the source) to be visible around the closer radio galaxy 3C 220.3 (the lens).

For this lensing to occur, 3C 220.3 must have a considerably large mass. Using recent X-ray and optical data paired with older multiwavelength data, we seek to better understand the radiative structure of 3C 220.3 and its dark matter content, in addition to obtaining a reconstructed image of SMMJ0939 in order to discover what it can tell us about the universe then.

The following sections provide a brief background and overview of the components that comprise the 3C 220.3 system.

[1] Calculated using Ned Wright's Cosmology Calculator (Wright 2006) and adopting a standard ΛCDM cosmology with $H_0 = 70.0$ km s^{-1} Mpc^{-1}, $\Omega_\Lambda = 0.721$, and $\Omega_m = 0.279$ (Bennett et al. 2013).

1.1. *Active Galactic Nuclei and Host Galaxies*

At the center of almost every large galaxy, there lies a supermassive black hole (SMBH), which can be up to a billion solar masses. For most galaxies in our local Universe, including our own Milky Way, the central black holes are essentially dormant and emit very little radiation (Jones et al. 2015).

However, for the type of galaxies called *active galaxies*, the SMBHs at their centers are vigorously accreting gas and dust. Between the gravitational and frictional forces that rip apart material as it falls onto the accretion disks around these SMBHs, the material becomes very hot, radiating in the infrared (IR), ultraviolet (UV), and X-ray regimes. This causes galaxies with accreting SMBHs to be unusually luminous across the electromagnetic spectrum, which gives them the name *active galaxies*. The accreting black hole systems at the centers of these galaxies are similarly named *active galactic nuclei* (AGN[2]).

1.1.1. *AGN Structure and Features*

Although the actual AGN are too small to spatially resolve (except in a handful of nearby cases), analyses at different wavelengths help probe the behavior in the compact central region. Currently, the widely-accepted model is that at the center of the host galaxy is a supermassive black hole which is encircled by an accretion disk and then a torus comprised of gas and dust. Due to the extreme heating of the infalling gas and dust around the SMBH, the accretion disk is likely the source of the majority of X-ray and UV radiation throughout the AGN (which is one of the reasons that X-rays are particularly useful in probing the innermost structure of AGN). Outside of the accretion disk, the dusty torus absorbs some of the UV and X-ray radiation and re-emits in the IR regime. Typically, the dusty torus extends inward to the *sublimation radius*, where temperatures exceed 2000 K and vaporize the dust particles (Jones et al. 2015).

[2]Note that AGN can refer to the singular form (active galactic nucleus) or the plural form (active galactic nuclei).

In some AGN, long narrow structures called *jets* form. These features extend from the SMBH (perpendicular to the accretion disk) and are thought to be caused by the magnetic fields from the black hole's rotation, which accelerates charged particles to relativistic speeds. The accelerated particles emit synchrotron radiation primarily at radio wavelengths (see Chapter 4 for explanation). These jets can be hundreds of kiloparsecs in length, often extending well outside the host galaxy. In many cases, they entrain obstructing material outside as well and into the intergalactic medium (IGM), forming radio lobes (which are visible in radio observations). Radio lobes can also lie within their host galaxies when the jets are slowed down by intervening material or are very young and have not reached the edge of the galaxy yet.

One of the best ways to separate active galaxies from normal galaxies is by looking at their multiwavelength spectral energy distributions (SEDs), which show excess radiation at high energies. Optical and UV emission lines have also been a key to understanding AGN and are important in active galaxy classifications.

Around the torus lie two regions: the *broad-line region* (BLR) and the *narrow-line region* (NLR). These regions derive their names from the Doppler broadening due to the velocity dispersion of their gas. Located around the opening of the torus, the NLR produces both "permitted" and "forbidden" emission lines, which have line widths of less than 1000 km s^{-1}. Even closer to the SMBH, the BLRs are almost exclusively devoid of forbidden lines and have line widths of up to 10 000 km s^{-1} (Jones et al. 2015; Rosswog & Brüggen 2007).

The so-called "forbidden" lines involve transitions from very long-lived excited states to lower energy levels (Rosswog & Brüggen 2007). Forbidden transitions are able to occur in the very low-density gas of NLRs since excited atoms in such areas do not interact very often and can remain in an excited state for a long time. As a result, very low probability transitions, such as the forbidden lines of doubly-ionized oxygen [OIII] of $\lambda = 4959$ Å and 5007 Å, are able to occur.

For areas of higher density gas, which can be found in both NLRs and BLRs, interactions between atoms are more frequent, and so the low-probability "forbidden" transitions do not occur. In these regions, the spectrum is dominated by the regular "permitted" lines, such as the Balmer lines of hydrogen. For AGN, the permitted lines are often the result of recombination, following the photoionization by photons from the AGN continuum.

Although the NLRs in active galaxies are visible from all viewing angles, the BLRs, which lie within the inner radius of the dusty torus, are obscured from view when the galaxy is viewed edge-on. In AGN spectra, broad lines can actually be visible amid the narrow lines via scattered light. This scattering results in a different polarization of the light corresponding to the broad lines, which indicates that the clouds that make up BLRs are likely closer to the SMBH than the accretion disk.

1.1.2. *Active Galaxy Classifications*

Active galaxies are broken into four main categories: Seyfert galaxies, quasars, blazars, and radio galaxies. The *unified models* suggest that all active galaxies have essentially the same structure but are viewed from Earth at different angles (Antonucci 1993). In these generally-accepted models, active galaxies are sorted into two groups: radio quiet galaxies, which have no relativistic jets, and radio loud galaxies, which do possess jets. Both *Seyfert galaxies* and *quasars* can be radio quiet or radio loud and are sub-classified depending on the viewing angle, which is determined by whether BLRs are visible (Type 2 and face-on vs. Type 1 and edge-on). Historically, the difference between Seyfert galaxies and quasars was whether the host galaxy was visible (Seyferts) or not (quasars), but with the development of larger telescopes, some quasar host galaxies became visible. Nevertheless, it has become standard to use a cutoff bolometric luminosity to distinguish between a quasar and a Seyfert galaxy.

Additionally, while Seyfert AGN were always known to lie within galaxies, quasars appear as point-like sources in the sky and can outshine their galaxy hosts, which caused them to

originally be called "quasi-stellar objects" (QSOs) or "quasi-stellar radio sources" (QSRs). Quasars are typically found at mid to high redshifts and only about 10% have been found to be radio loud (Jones et al. 2015). *Blazars*, which are similar to quasars, are exclusively radio loud. Since their relativistic jets are almost directly aligned with our line-of-sight, their emission is relativistically boosted and they appear to be extremely luminous.

The final category of active galaxies, *radio galaxies*, are of particular interest for this investigation since 3C 220.3 is classified as such. Since they possess powerful jets, radio galaxies fall in the radio loud category. Radio galaxies are oriented more edge-on to Earth and can be sub-classified based on the presence of BLRs. However, unlike Seyfert galaxies, almost all radio host galaxies have been found to be elliptical galaxies (Jones et al. 2015). In observations at radio frequencies, the radio lobes are typically visible, as well as the accompanying jets and the point-like AGN. The following section discusses the components and classifications of radio galaxies in more details.

1.2. *Radio Galaxies*

Radio galaxies have several classification systems, each of which focus on different components. Much like with Seyfert galaxies, radio galaxies can be categorized by their spectra. Since the BLRs of an AGN lie in the hole of the dusty torus, they are obscured when viewed at certain angles. The NLRs, which lie above and below the accretion disk and torus, are always visible. As a result, radio galaxies that have both broad-lines and narrow-lines in their spectra are called *broad-line radio galaxies*, or BLRGs. Radio galaxies with only narrow emission lines are called *narrow-line radio galaxies*, or NLRGs. Since the dusty torus obscures the BLRs as they are viewed at more oblique angles, NLRGs are viewed much closer to edge-on than BLRGs. Since 3C 220.3 has no broad-line emissions in its spectra, it is classified as a NLRG (Hardcastle & Worrall 1999), which implies that we see it mostly edge-on from Earth.

In the large picture of active galaxy classification, BLRGs and quasars are the radio-loud counterparts of Type 1 Seyfert galaxies and Type 1 QSOs (radio-quiet quasars). Similarly, NLRGs are the radio-loud counterparts of Type 2 Seyfert galaxies and Type 2 QSOs. Much like the distinction between Seyfert galaxies and quiet-quasars, the difference between BLRGs and radio-loud quasars is historical, based on whether the source was observed to be located within a galaxy (BLRG) or whether it appeared as a point source (radio-loud quasar).

Another system used to describe radio galaxies is the Faranoff-Riley Classification (Fanaroff & Riley 1974), which focuses on the ratio ($R_{\rm FR}$) of the distance between the "hotspots" (brightest areas) of the radio lobes to the distance from end-to-end of the radio lobes. Radio galaxies with ratios $R_{\rm FR} < 0.5$ are known as Class I or FR I galaxies, while radio galaxies with ratios $R_{\rm FR} > 0.5$ are known as Class II or FR II galaxies. Of the two classes, FR I galaxies are less luminous but have visible jets and AGN cores. The hotspots in the lobes of FR I galaxies are typically closer towards the AGN core, which causes the far-out edges of the lobes to be less distinct, corresponding to the older and cooler areas of the lobes. FR II galaxies, on the other hand, are much more luminous than their FR I counterparts and have so-called "edge-darkened" lobes (lobes that are more sharply defined at the outer edges, away from the AGN core, and have hotspots at the extremities). Although the radio lobes, AGN cores, and jets are more luminous in FR II galaxies, the lobes are much brighter than the two other components, and it is common not to see any jets. In fact, jets are visible in less than 10% of FR II galaxies (Kembhavi & Narlikar 1999). Since 3C 220.3 has noticeable hotspots, edge-darkened lobes, and lacks observable jets, it is classified as a FR II galaxy (Laing et al. 1983).

For particularly luminous radio galaxies, there is an additional classification. Powerful radio galaxies (PRGs) are FR II radio galaxies with luminosities $L_{178\ \rm MHz} > 10^{27}$ W Hz^{-1} sr^{-1}. PRGs are typically expected to be found in large galaxy clusters with big dark matter halos (White & Rees 1978) and are often some of the more massive galaxies at their redshifts (Lilly & Longair 1984). With a reported flux density of 15.7 Jy (Laing et al. 1983) and

redshift of $z = 0.685$, the luminosity of 3C 220.3 at 178 MHz is $L_{178\ \mathrm{MHz}} = 10^{27.39}$ W Hz^{-1} sr^{-1} (Cleary et al. 2007) and so it is considered a PRG (Simpson et al. 1999) (although the FR II classification is more commonly used).

1.3. *The Revised Third Cambridge Catalogue*

After the discovery of the first radio galaxy, Cygnus A, in 1946, researchers began conducting extensive radio surveys. While the first radio survey (done by the University of Cambridge and known as the 1C Catalogue) only found 50 radio sources, it was a precursor to larger surveys to come. In the 1950s, two surveys were performed at 81 MHz – a second survey in Cambridge (2C), which consisted of four antennas and maximum baselines of 1900 ft (east-west) and 168 ft (north-south) and had a flux density limit of 100 Jy and beamwidth of 1° by 15° (Hewish & Ryle 1955; Shakeshaft et al. 1955), and a survey in Australia with the Mills Cross interferometer, which consisted of two perpendicular 1500 ft arrays with two rows of 250 half-dipole antennas (Mills et al. 2005) and had a flux density limit of 20 Jy and beamwidth of 50′ (Mills & Slee 1957; Mills et al. 1958). Although the two surveys overlapped part of the sky, subsequent comparisons of the radio sources discovered found almost no matches. It soon became clear that due to low resolution, the Cambridge survey suffered from a great deal of confusion between nearby radio sources that could not be resolved (Veron 1977; Norris 2017).

To eliminate the confusion of sources in the 2C survey, the collaboration at Cambridge reconfigured the 4-antenna interferometer to observe at 159 MHz with a beamwidth of 1.2° by 7° (Edge et al. 1959). The survey counted sources with flux densities greater than 7.45 Jy and covered two regions of the sky: one with declinations $37° < \delta < 57°$ and right ascension (RA) of $0^{\mathrm{h}} < \alpha < 24^{\mathrm{h}}$ and the other with declinations $-10° < \delta < +10°$ and RA of $0^{\mathrm{h}} < \alpha < 8^{\mathrm{h}}$. The 471 sources were published as the Third Cambridge Catalogue of Radio Sources, or 3C Catalogue (Edge et al. 1959). In the catalog, sources are numbered as integers in ascending order based on their right ascension (RA).

However, source confusion still persisted and the positions of many of the sources had high uncertainties, so the interferometer at Cambridge was reconfigured once again to observe with higher resolution at 178 MHz. The survey, which covered all areas of the sky with declination $\delta > 5°$ and accepted sources with flux densities of at least 9.0 Jy, was used as an independent check of the 3C sources. With the improved resolution and higher flux density threshold, this survey removed 93 of the 3C sources that had overestimated flux densities and added 90 sources, many of which were located outside of the original 3C survey regions or were newly resolved by the 178 MHz observations. The 328 sources, which are among the brightest radio sources in the sky, were published by Bennett (1962) as the Revised Third Cambridge Catalogue of Radio Sources, or the 3CR Catalogue. The new 3CR sources were added to the 3C numbering scheme with decimal numbers to avoid naming confusion with other sources. With a declination of 85:15:25.90 (J2000) for its radio core, 3C 220.3 was well outside of the original 3C survey region and was discovered during the 3CR survey.

1.4. *Submillimeter Galaxies*

Unlike radio galaxies, which are obvious with their immense lobes in the radio sky, submillimeter galaxies, or SMGs, are very faint. They remained unseen until 1998, when they were first detected by the Submillimeter Common User Bolometer Array (SCUBA) (Holland et al. 1999), not long after the advent of submillimeter astronomy. Soon after, several surveys to catalog and analyze the SMG population began with SCUBA and the Max-Planck Millimeter Bolometer (MAMBO) (Bertoldi et al. 2000), as well as later ones by *Herschel* (Leung & Riechers 2016).

SMGs are characterized by their high infrared (IR) and far-infrared (FIR) emissions ($L_{IR} \sim 10^{12} L_{\odot}$), which are due to their high dust and gas contents ($M_{\rm gas} > 10^{10} M_{\odot}$) (Leung & Riechers 2016). Based on the surveys, SMGs are typically found at redshifts of $z = 1$ to $z = 3$ (Chapman et al. 2005), which places them at the epoch of galaxy formation and high star formation rates (SFR $\gtrsim 500 M_{\odot}$) (Blain et al. 2002). These high-redshift

galaxies give insight into early galaxy formation and are thought to be the progenitors of massive elliptical galaxies that reside in clusters (Tacconi et al. 2008).

However, between the fact that SMGs are so distant and that they are often much fainter in other, non-submillimeter wavelengths (Blain et al. 2002), multiwavelength follow-ups of this galaxy population are difficult and expensive in telescope time. As a result, other surveys are looking for SMGs that are magnified by gravitational lensing, usually by galaxy clusters (Chapman et al. 2005). Along with the strongly lensed SMGs HLSW-01 and the Cosmic Eyelash, the SMG lensed by 3C 220.3, SMMJ0939, is one of the brightest lensed SMGs in the sky (Leung & Riechers 2016), making it ideal for multiwavelength follow-up.

1.5. *Gravitational Lensing*

"Of course, there is no hope of observing this phenomenon directly," wrote Einstein (1936) in his famous letter on the possibility of gravitational lensing. Although the light-bending that causes gravitational lensing comes from Einstein's general relativity, he thought that any lensing effects would be too small to resolve with a telescope and too faint to detect. However, Einstein's statement only considered lensing by stars and not entire galaxies or galaxy clusters. Not long after, papers by Zwicky (1937) and others were published, discussing the probability of lensing by galaxies (which were thought to be nebulae at the time) and other large structures.

In 1979, the first gravitational lens was discovered by the observation of what seemed to be two quasars (Q0957+561 A and B) which were unusually close together and had the same redshift (Walsh et al. 1979). After additional analysis and the detection of the lensing galaxy, it became clear that the two quasars were actually multiple images of the same object. Just under ten years later, the first Einstein ring (which occurs when a background source is almost directly aligned with the lensing object and the observer) was discovered by Hewitt et al. (1988).

Gravitational lensing arises from the light bending described by general relativity. When a photon passes by a massive object, its path becomes curved due to the fact that the geodesic lines around the object become curved. This light deflection angle of $\delta\theta = 4GM/c^2b$[3] was observed by Eddington during the eclipse of 1919 and was one of the first major tests of general relativity.

The most basic gravitational lensing model uses a point mass approximation for the lens. The system is structured such that the observer lies a distance D_L from the lens (the foreground object with mass M) and distance D_S from the source (the background object). The lens and the source are separated by a distance D_{LS}.[4] β describes the angle (with respect to the observer) between the lens and the source in the sky and θ describes the angle between the observer and the lensed image(s) of the source in the sky (relative to the observer) (Kembhavi & Narlikar 1999). When the source is directly aligned with the observer and the lens ($\beta = 0$), a ring around the lens is visible. The resulting circular image has an angular radius of

$$\theta_E = \sqrt{\frac{4GMD_{SL}}{c^2 D_S D_L}} \tag{1}$$

and is known as an *Einstein ring*, where θ_E is the Einstein radius (Dodelson 2017). For the point mass approximation, we can also define the gravitational radius of the lens to be

$$R_{\text{lens}} = \frac{GM}{c^2} \tag{2}$$

which is the radius of a black hole of equivalent mass. The dimensionless ratio in Equation 3 can then be rewritten more clearly as

$$\theta_E = 2\sqrt{\frac{R_{\text{lens}} D_{SL}}{D_S D_L}} \tag{3}$$

Of course, in real systems, both the lenses and sources are often better described by extended regions rather than points. Unlike point source lenses, extended lenses are described

[3]Here, $\delta\theta$ is the deflection, M is the mass of the lens, G is the gravitational constant, c is the speed of light, and b is the impact parameter (Dodelson 2017)

[4]Note that the distances D_L, D_S, and D_{LS} are angular diameter distances (which are defined by the comoving distance divided by $1 + z$), and so on cosmological scales, $D_{LS} \neq D_S - D_L$.

by more complicated models of the mass distribution that result in critical lines or curves that cause additional pairs of images. Extended sources (like galaxies) also experience a shearing effect (related to the surface density of the lens) which distorts the lensed images into arcs (Dodelson 2017). In addition to multiple images, a gravitational lens can also magnify its source. The magnification factor μ is proportional to the ratio of the flux (and the angular size) of lensed to unlensed images.

There are two main categories of gravitational lensing: strong lensing and weak lensing. While strong lensing applies to systems with point-like or extended lenses or sources (e.g. stars or galaxies), weak lensing applies to systems with more diffuse, large-scale components like galaxy clusters. Typically, multiple images, rings, and magnification of sources are only observed in strongly lensed systems (Dodelson 2017).

Today, gravitationally lensed systems are very important in astrophysics. The observed images in the sky are very useful in determining structures of objects (both large and small-scale), regular and dark matter content, and spectral analysis through the geometries, time delays, and magnification of multiple images. See Barnacka (2018) for a more detailed discussion of these uses.

Lens modeling by computers is very useful for determining the physical properties of a gravitationally lensed system and of the lensing galaxy or galaxies. In essence, the modeling attempts to reconstruct the source object by minimizing the residuals of simulated images based on a set of physical quantities (e.g. mass distribution of the lens, redshifts, and distances). The particular method used to model the strongly lensed 3C 220.3 system is discussed in Section 4.3.

1.6. *The 3C 220.3 System*

At first glance, nothing seemed particularly unusual about 3C 220.3.[5] In a far-infrared (FIR) survey of 3C radio galaxies and quasars designed to probe the evolution of AGN and their host galaxies,[6] the NLRG was just another data point. However, the *Herschel Space Observatory* observations of 3C 220.3 showed that the galaxy was emitting much more infrared emission than is typical for radio galaxies at similar redshifts. Subsequent comparison with archival optical exposures from the *Hubble Space Telescope* (*HST*) at $\lambda =$ 702 nm explained the unusual brightness: an arc indicative of the presence of a background, gravitationally lensed source. In addition to the arc and the radio galaxy, the *HST* images showed another bright source near 3C 220.3 that lies within the radius of the Einstein ring arc. This source was labelled as source B.

As the first PRG to be discovered to be lensing another galaxy while unassociated with a massive galaxy cluster (Haas et al. 2014), 3C 220.3 is an object of great interest. The system's uniqueness made it a prime candidate for quickly compiling a multiwavelength data set through follow-up proposals, as well as with Director's Discretionary Time (DDT), on several telescopes. Photometric observations come from the following observatories/telescopes: *Herschel* (IR), *HST* (optical), the Karl G. Jansky Very Large Array (JVLA, radio), the Keck II telescope (IR), the *Spitzer Space Telescope* (IR), the Submillimeter Array (SMA), and the *Chandra X-ray Observatory*. Spectroscopic data were also taken by the Double Spectrograph on the Palomar 5 m Hale Telescope and the Low Resolution Imaging Spectrometer on the Keck I telescope and confirmed the redshift of 3C 220.3 to be $z = 0.685$, consistent with earlier calculations (Spinrad et al. 1985). The Keck spectra (Haas et al. 2014, Figure 4) also

[5]In Cleary et al. (2007), 3C 220.3 did stand out. In an analysis of *Spitzer* data for 33 3CRR sources, 3C 220.3 was the only target to have a detection at 136 μm. This is a high flux density, but the system was not investigated further.

[6]Haas, M., 2011, Herschel Proposal ID OT1_mhaas_2, "The Herschel Legacy of powerful 3C radio galaxies and quasars at $z < 1$."

made it possible to determine the redshift of the lensed galaxy (SMMJ0939) to be $z = 2.221$, but source B could not be resolved due to its proximity ($\sim 1.5''$) to 3C 220.3 (source A).

In the multiwavelength data set, an arc is visible in the archival *HST* image, while a close-to-complete Einstein ring is visible the Keck data and SMA image (Figure 1). The radio lobes and an unresolved core are also visible in the JVLA data (Figure 8). The *Chandra* X-ray data for the system showed very low-count, diffuse emissions (Figure 4, left).

Using the aforementioned data, Haas et al. (2014) performed the first analysis of the 3C 220.3 system, focusing on lens modeling, mass estimations, and spectral analysis. Since the redshift of source B is undetermined, the lensing simulations considered three possible cases with varying degrees of impact by source B: (1) as part of the lensed SMG, (2) in front of 3C 220.3 but too low mass to affect the image, and (3) as part of the lens (i.e. a double lens). Comparing these models with the observed images, Haas et al. (2014) found that the double lens model (Case 3) matched the observations the best, confirming that source B lies within the Einstein ring and is not part of the lensed SMG. Based on their simulations, the magnification factors of the source for 2.124 μm and 1 mm are $\mu_{2.124\mu\mathrm{m}} \sim 7 \pm 2$ and $\mu_{1\mathrm{mm}} \sim 10 \pm 2$, respectively. Although the reconstructed images of the source have fairly uniform stellar and dust emissions, there is a region of UV emissions in the northeast part of the galaxy. Combined with the analysis of the spectra, Haas et al. (2014) postulate that the SMG may host an obscured type-2 QSO AGN that is beginning to blow away obscuring

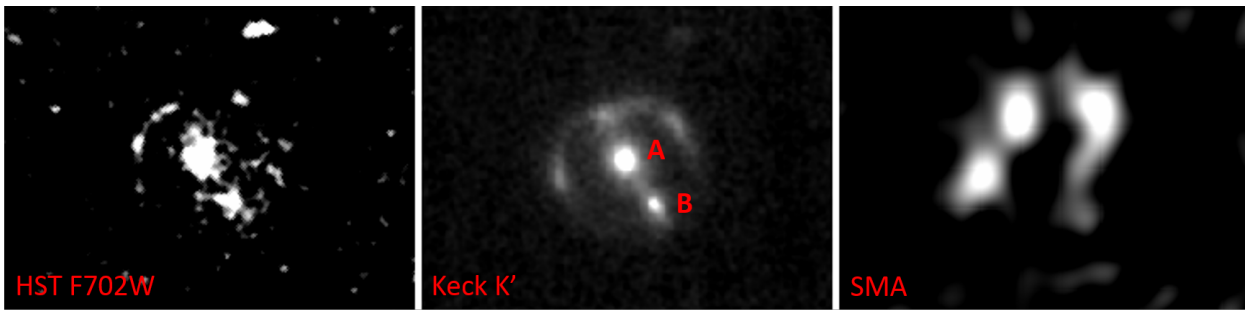

Figure 1: From left to right: Galaxy (source A), source B, and Einstein ring as seen with *HST* F702W (702 nm, archival), Keck II in the K' band (2.124 μm), and the SMA (1 mm).

dust, allowing the UV radiation to be seen. The double lens simulations also found the upper limits for the total masses (baryonic and dark matter) of 3C 220.3 (occasionally referred to as lens A or source A) and source B to be $M_A \sim 3.5 \times 10^{11} M_\odot$ and $M_B \sim 1.2 \times 10^{11} M_\odot$.

Haas et al. (2014) also estimated the luminous (stellar) masses of sources A and B by assuming a typical old-star dominated stellar population for radio galaxies. The calculations found the resulting stellar masses for the foreground components of the 3C 220.3 system to be $M_A^* \sim 2.2 \times 10^{11} M_\odot$ and $M_B^* \sim 5.5 \times 10^{10} M_\odot$, with dark-to-luminous mass ratios of 0.7 to 1.2 (dark matter fractions of 40% to 55%). Compared to other radio loud galaxies of similar masses and redshifts, the dark matter content of the 3C 220.3 system falls in the average to moderately high range (Haas et al. 2014, Section 5). In terms of X-rays, the initial, 10 ks *Chandra* data[7] for the system showed a very diffuse, low-count (16 photon) emission, which makes it extremely difficult to identify the X-rays with any structure of 3C 220.3.

In a second analysis of the 3C 220.3 system, Leung & Riechers (2016) focused specifically on SMMJ0939. Using observations with the Combined Array for Research in Millimeter-wave Astronomy (CARMA) at 104 GHz, Leung & Riechers (2016) detected the CO($J = 3 \rightarrow 2$) emission line in the SMG as well as the continuum emission from the radio galaxy. Since the CARMA data has much less spatial resolution than the JVLA data used in Haas et al. (2014), Leung & Riechers (2016) assume that the continuum emission is dominated by the radio galaxy and the CO($J = 3 \rightarrow 2$) emission line is from the SMG. Using the CO($J = 3 \rightarrow 2$) measurements in their spectral energy distribution (SED) fitting, Leung & Riechers (2016) calculated the dust and gas masses of the SMG to be $M_{\rm dust} = 50.5^{+20.4}_{-20.2} \times 10^8 M_\odot$ and $M_{\rm gas} = (2.74 \pm 0.57) \times 10^{10} M_\odot$. Using the infrared and far-infrared luminosities, Leung & Riechers (2016) calculated the star formation rate (SFR) to be $\mathrm{SFR_{FIR}} = 526 \pm 73\ M_\odot\ \mathrm{yr}^{-1}$ (consistent with the value of $\mathrm{SFR_{FIR}} = 555.8^{+62.5}_{-57.3}\ M_\odot\ \mathrm{yr}^{-1}$ reported in Table 14 of Westhues

[7]Kuraszkiewicz, Joanna, 2013, *Chandra* Cycle 14 Proposal #14700660, "The Herschel Legacy of powerful 3C radio galaxies and quasars II: observing Proposal."

et al. (2016)), with a gas depletion timescale ($M_{\rm gas}$/SFR) of $\tau_{\rm depl} = 52 \pm 8$ Myr. While these numbers are fairly consistent with surveys of other SMGs, both the SFR and gas-to-dust ratio are lower than the average for other SMGs. However, since the gas mass is similar to that found in galaxies hosting type-2 quasars, Leung & Riechers (2016) agreed with Haas et al. (2014) that the lensed SMG is transitioning from a phase of high star formation (a "starburst") to an unobscured quasar phase.

In the multiwavelength analysis done by Haas et al. (2014), the X-ray data had so few counts that it was impossible to make any analysis of the kinematics of the 3C 220.3 system. Additionally, since the optical *HST* observations were only in one filter (F702W), the mass calculations and lens modeling were limited. This thesis uses more recent data from *Chandra*,[8] with an effective exposure five times that of the X-ray data used in the first analysis (200 ks vs. 20 ks), and deeper data from *HST* in three different filters (F606W, F814W, F160W). These observations will allow for more accurate mass calculations of the 3C 220.3 system (useful in both dark matter and lensing calculations) and for the identification of X-ray origin (i.e. what areas of the system they come from). The more recent (2014) *HST* data set also reveals a full Einstein ring with a radius of approximately $2''$, rather than the partial arc seen in the archival *HST* images, which gives more information for the lens modeling.

While the deeper *Chandra* observations recorded many more photons (~ 200) than the observations used in Haas et al. (2014), the X-ray structure of the 3C 220.3 is not immediately clear. In order to determine the X-ray fluxes of the different components of the radio galaxy/lensed SMG system, we compare them to the components visible in the multiwavelength data set. These components are as follows: the AGN core (which appears as a point source due to its compactness), the double radio lobes (which extend above and below the

[8]Wilkes, B.J., 2014, *Chandra* Cycle 15 Proposal #15700378, "Probing dark matter in the luminous radio galaxy 3C220.3 and the structure of the z=2.22 SMG/AGN it is lensing."

accretion disk of the core and to the northwest and southeast of the core in the sky), the 3C 220.3 galaxy (optical and IR), source B (optical and IR), and the Einstein ring of the lensed SMG (optical, IR, and submillimeter). The northwest and southeast radio lobes have dimensions of about $4.5'' \times 3.5''$ (32 kpc × 25 kpc) and $4'' \times 3''$ (29 kpc × 22 kpc), respectively. The centers of both lobes are located about $3.5''$ (25 kpc) from the radio core. The analyses of these regions are discussed in Chapter 3.

1.7. *Introduction to X-Ray Astronomy*

Earth's atmosphere is opaque to X-rays, so X-ray measurements have to be conducted in the upper atmosphere or in space. The first extrasolar X-ray object (Scorpius X-1) was detected in 1962 by Riccardo Giacconi and his team during a Geiger-counter-equipped rocket launch intended to detect solar X-rays reflecting off the Moon (Giacconi et al. 1962). The discovery of Scorpius X-1 was confirmed by additional rocket flights with better detectors and follow-ups by optical telescopes, and the field of X-ray astronomy was born (Arnaud et al. 2011). However, while high-altitude balloons are still used as detectors, they can only detect the highest energy X-rays and gamma rays due to the atmosphere above them. To detect a wider energy range of X-ray photons, space-based telescopes are essential.

Space-based X-ray astronomy began in 1970, with the launch of the *Uhuru* satellite (Giacconi et al. 1971). After that, many other telescopes followed, notably the *Einstein Observatory* (Giacconi et al. 1979), which was the first orbiting telescope to focus X-rays for imaging using grazing-incidence mirrors, and *ROSAT* (Truemper 1990), which produced the first extensive all-sky X-ray survey. The *Chandra X-ray Observatory* (Weisskopf et al. 2000), which collected the X-ray data on the 3C 220.3 system, was launched in 1999 and has very high spatial and energy resolution for imaging and spectroscopy.

1.7.1. *X-Ray Data*

X-ray astronomy is fundamentally different from most other areas of astronomy. When an optical telescope takes an exposure, the resulting image is a cumulative picture of the

many, many photons that reached the camera over a specific period of time. The fluxes can be determined from the values that were recorded for each pixel, but nothing is known about the individual photons. The approach is similar to the mindset used in statistical mechanics – we know very little about each individual particle, but because there are so many of them, we can understand how they behave as a system.

By contrast, in X-ray astronomy, many fewer photons are recorded. Rather than observing the overall flux from a source, X-ray detectors count the individual photons (the "events") that are collected by the CCD. Although X-ray observations are often visualized as an image, the actual data are actually recorded in a table, called an *events list*. These lists log the time, energy, and position (both on the detector and in the sky) of each photon, providing a unique type of data. In addition to images, spectra, light curves, and source lists can also be extracted from event files.[9]

Similar to flat fielding, dark and bias exposures, and standard star observations in optical astronomy, X-ray observations are paired with additional files for calibration and analysis, most notably the ancillary response file (ARF) and the redistribution matrix file (RMF). The ARF reflects the effective area (i.e. sensitivity) of the mirrors of the telescope as a function of the energy of an event. The RMF describes the energy resolution of the instrument, giving the probability distribution for the energy at which an event of a specific intrinsic energy is recorded by the instrument.[9] Since both the ARF and RMF are functions of position on the detector, a particular ARF and RMF must be determined based on the position of the source in question. Figures 2 and 3 show a sample ARF and RMF for the combined[10] spectral analysis of the SE radio lobe.

[9]Lee, N.P., McDowell, J.C., Tingle, E.D., & Guardado, K.M. (Eds.). An X-ray Data Primer (*Chandra X-Ray Center*). cxc.cfa.harvard.edu/cdo/xray_primer.pdf

[10]The combined-observation ARF and RMF calibration files were produced as a result of the CIAO `combine_spectra` process for the spectral analysis (see Section 3.3).

1.7.2. *X-Ray Analysis*

As previously described, X-ray astronomy observes very few photons compared to other wavelengths and so the observations are photon-limited and the data is Poisson in nature. In X-ray imaging spectroscopy, it is standard to use a *forward-folding* approach, which convolves a model with the RMF and ARF before fitting the spectrum, rather than correcting the observed spectra by deconvolving the observations and the instrument response.[9]

It is also important to consider both instrumental and cosmic backgrounds. Typically, *Chandra* X-ray analyses only focus on events below 8 keV, since the cosmic X-ray background (which is comprised of unresolved AGN) dominates at higher energies. At low energies, analyses often ignore events below 0.3 keV or 0.5 keV, where instrumental noise dominates.

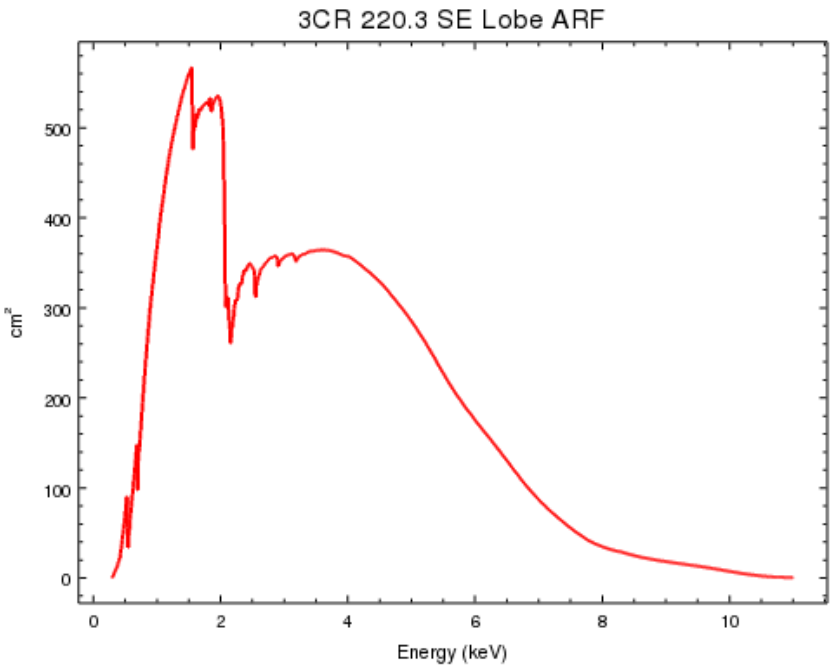

Figure 2: Combined-observation ARF for spectral analysis of the southeastern (SE) lobe of 3C 220.3 (described in Section 1.6)

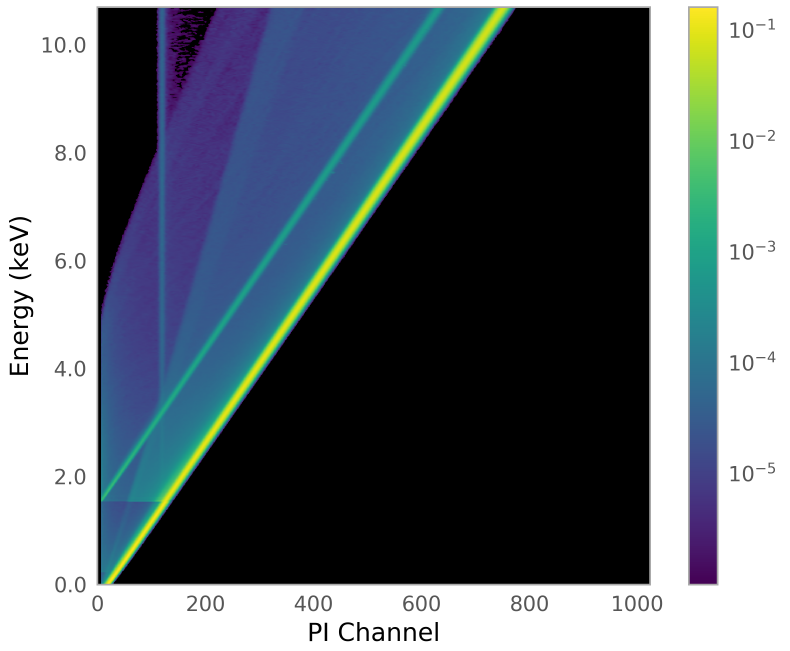

Figure 3: Combined-observation RMF for SE radio lobe spectral analysis. The colorscale shows the logarithmic probability that a photon of a specific intrinsic energy (indicated by the y-axis) will be recorded in a particular pulse-invariant (PI) channel. The PI channel is the gain-corrected energy recorded by the instrument (the pulse height amplitude, or PHA).

2. DATA AND OBSERVATIONS

An extensive, multiwavelength data set for 3C 220.3 already exists, with observations from a variety of different telescopes in radio, sub-millimeter, IR, optical, and UV bands, as well as optical spectroscopy. As discussed in Section 1.6, 3C 220.3 was discovered to be a gravitational lens when it appeared much brighter than expected in the far-IR data from the *Herschel Space Observatory*. Comparison to the available archival *Hubble Space Telescope* observations at 702 nm on the Wide-Field Planetary Camera 2 (WFPC2) revealed the tell-tale arc of gravitational lensing and explained the unexpected brightness.

The first analysis of 3C 220.3, a paper by Haas et al. (2014), used a combination of observations from *Herschel*, *HST*, the Karl G. Jansky VLA (JVLA), the Keck II telescope, the *Spitzer Space Telescope*, the Submillimeter Array (SMA), and *Chandra*. Redshift calculations of the various components of the system were performed with optical spectra taken by the Double Spectrograph on the Palomar 5 m Hale Telescope and the Low Resolution Imaging Spectrometer on the Keck I telescope, confirming the redshift of 3C 220.3 to $z = 0.685$ and finding the SMG's redshift to be $z = 2.221$. A third object, labeled source B, is also visible in the Keck, SMA, and *HST* images. Although the redshift of source B is unknown, it seems possible (from lens modeling) that it is close to the redshift of source A (3C 220.3). Haas et al. (2014)'s determinations of fluxes in the radio, submillimeter, and near-infrared bands are used in this analysis, as well as their calculated redshifts for the lensed galaxy SMMJ0939. Details on these observations are listed in Table 3.

Since the publication of Haas et al. (2014), our team has obtained deeper X-ray and optical observations of 3C 220.3. While the original *Chandra* data had very low photon counts and S/N (hindering the identification of the system components), the new observations (collected in 2014) have almost twenty times the total exposure time and many more counts[11].

[11] Wilkes, B.J., 2014, *Chandra* Cycle 15 Proposal #15700378, "Probing dark matter in the luminous radio galaxy 3C220.3 and the structure of the z=2.22 SMG/AGN it is lensing."

Similarly, while the archival *HST* data have only two exposures in the F702W filter, the 2014 *HST* data[12] have significantly longer exposures in three different filters (F160W, F814W, and F606W), which will help for estimating the mass of 3C 220.3 in order to do a more detailed reconstruction of the lensed SMG. Neither of these two data sets (Tables 1 and 2) have been extensively analyzed and are a primary focus of this thesis.

An additional analysis of the gaseous makeup of SMMJ0939 was published by Leung & Riechers (2016), but since the Combined Array for Research in Millimeter Astronomy (CARMA) data used by Leung & Riechers (2016) is much lower resolution than similar SMA observations, it will not be used in this analysis. With the availability of the much deeper and higher resolution 2014 *HST* data, the *Herschel* and *Spitzer* data, which do not resolve the lens from the primary galaxy, are also omitted.

2.1. *Chandra X-Ray Observatory*

Although *Chandra* observed 3C 220.3 on UT 21 January 2013 for 10 ks,[13] there were only 16 X-ray photons distributed across the whole, multiwavelength structure of the source, with 1.8 of the 16 counts expected from the background (Haas et al. 2014). In 2014, *Chandra*'s Advanced CCD Imaging Spectrometer (Garmire et al. 1986, ACIS) observed 3C 220.3 five times with the S-array (ACIS-S) for a total exposure of 198 ks (55 hours). These *Chandra* observations are listed in Table 1. Including the multiwavelength components (e.g. radio lobes, Einstein ring, etc.), the 3C 220.3 system has approximate dimensions of $14'' \times 6''$, with the position angle (PA) of the long (radio lobe) axis at about 130° and the PA of the shorter axis (intersecting the Einstein ring, AGN core, and source B) at about 40°.

The ACIS-S detector is one of the two components that make up the ACIS instrument. ACIS-S is a 1 × 6-chip CCD array that consists of four front-illuminated (FI) and two back-

[12]Wilkes, B.J., 2014, Hubble Space Telescope Cycle 21 Proposal #13506, "Probing dark matter in the luminous radio galaxy 3C220.3 and the structure of the z=2.22 SMG/AGN it is lensing."

[13]Kuraszkiewicz, Joanna, 2013, *Chandra* Cycle 14 Proposal #14700660, "The Herschel Legacy of powerful 3C radio galaxies and quasars II: observing Proposal."

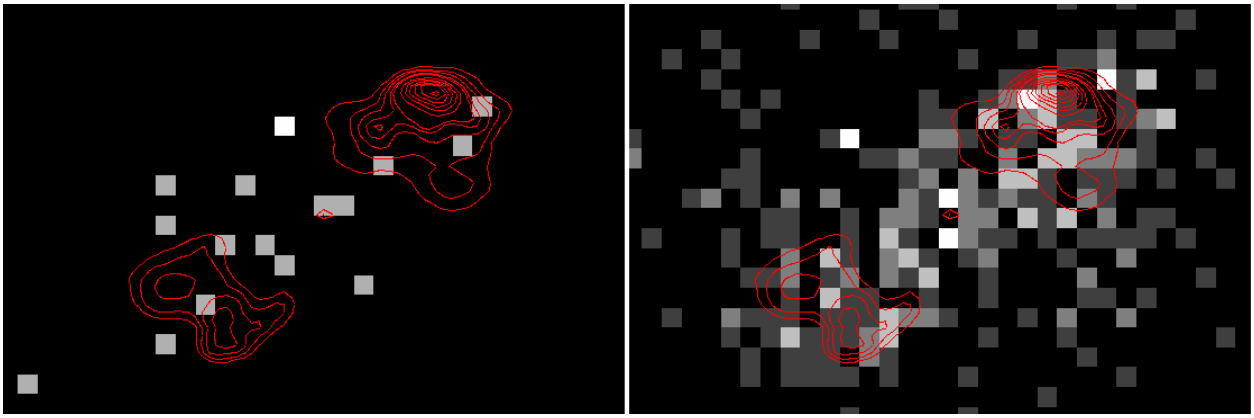

Figure 4: Left: 10 ks exposure of 3C 220.3 with *Chandra* (2013). Right: Merged 198 ks exposure with Chandra (2014). In both images, the diffuse distribution of X-ray counts is visible. The data are filtered to broadband energy range (0.3 - 8 keV). JVLA radio contours are shown in red.

illuminated (BI) CCDs. Tilted with respect to the telescope's focal surface to match the HETG Rowland circle,[14] ACIS-S has an $8' \times 8'$ field of view (smaller than the $16' \times 16'$ f.o.v. of its counterpart, ACIS-I) and can be used for both imaging spectrometry and high-resolution spectroscopy. Around half of *Chandra* ACIS imaging is done with ACIS-S since it has a better low (or soft) energy response. Our data were recorded on the ACIS-S3 chip, located at the focal point of the telescope. This chip is one of the two back-illuminated CCDs on ACIS. The BI design of S3 gives it better low-energy sensitivity than its front-illuminated companions. See Figure 5 for a diagram of the ACIS CCD layout.

[14]The High Energy Transmission Grating (HETG) provides high-resolution spectra for *Chandra* observations. The Rowland circle is a term used in X-ray spectroscopy. When spherical gratings like those in the HETG are used, the Rowland circle describes the points at which light focuses after passing through gratings located on the same circle. The radius of the Rowland circle is half that of the curvature of the spherical gratings. The gratings were not used for our *Chandra* observations of 3C 220.3 since the data are imaging spectroscopy rather than high-resolution spectroscopy.

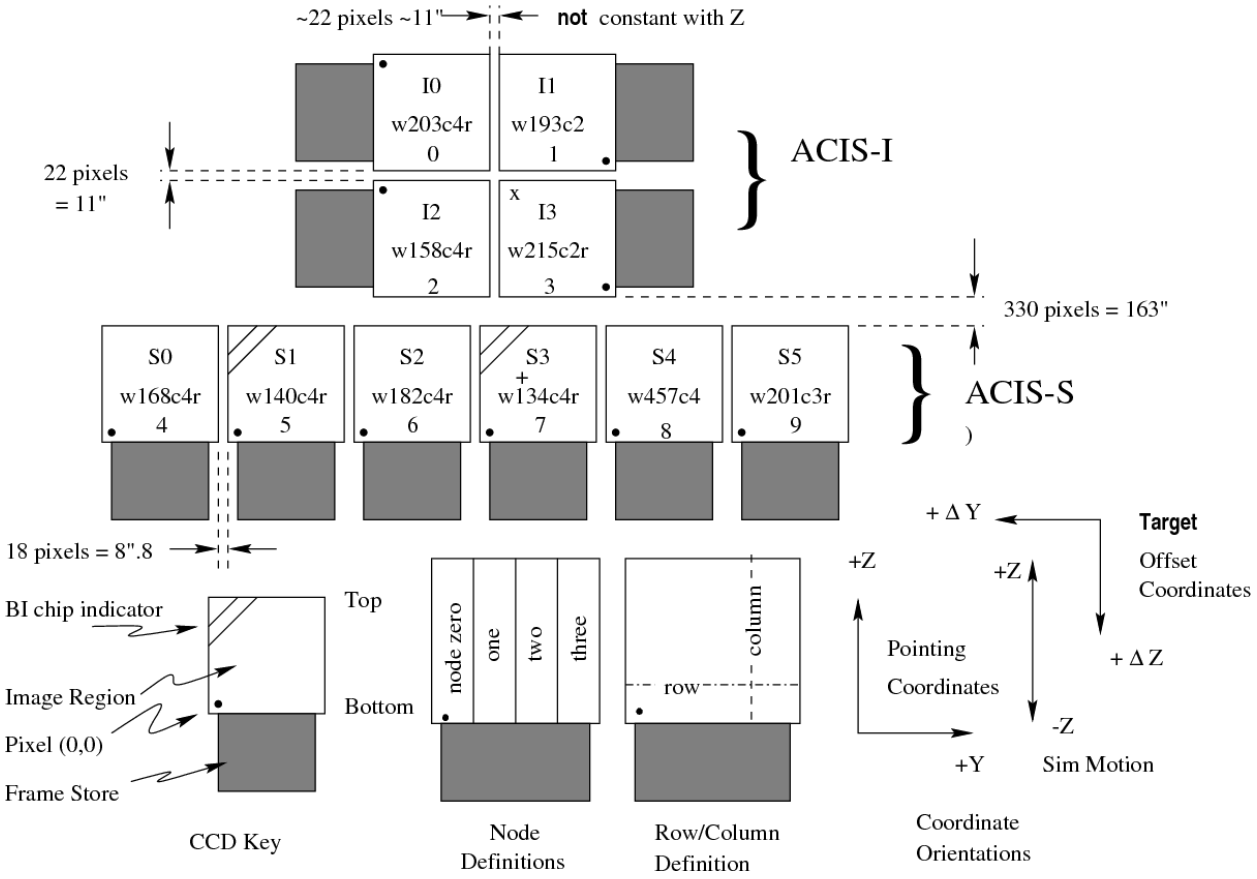

Figure 5: Schematic drawing of the ACIS CCD layout on the *Chandra X-Ray Observatory*. The top illustration is of the ACIS-I instrument, a 2 × 2 FI CCD array. The middle illustration represents the layout of ACIS-S with the numbered pixels. The S3 CCD can be seen in the middle with a plus sign ("+") that indicates the focal point. All of the ACIS CCDs have a field of view of $8' \times 8'$. Figure from Chapter 6 Section 1 of the *Chandra* Proposers' Observatory Guide (POG). The POG can be found online at: http://cxc.harvard.edu/proposer/POG/html/index.html

Although *Chandra* has a pixel size and spatial resolution of about 0.5″, the resolution of the images can be determined to better than that of the native pixel size. Since the images *Chandra* takes are dithered and since the arrival time, location and energy of each photon event is known, algorithms can reconstruct the image at resolutions smaller than 0.5″. This is called *sub-pixel binning*. An eighth-size (0.125″) sub-pixel binned image is shown in Figure 6.

In both the 2013 and 2014 *Chandra* data, the 3C 220.3 system appears to have very diffuse X-rays emission, which makes the analysis challenging. However, with the sub-pixel binning (Figure 6), several interesting features of 3C 220.3 seem to become visible. First, there seem to be no counts that coincide with the JVLA radio core, which indicates that the AGN is likely Compton thick (discussed in Section 3.2). Second, there seems to be a ring-like structure in the X-ray data that coincides with the Einstein ring in the *HST* contours. If these X-rays are from the SMG, it would provide further evidence suggesting the presence the SMG transitioning to an unobscured quasar phase. Finally, there appear to be some X-ray counts that overlap with source B in the *HST* contours, which could mean that source B also has an AGN. Furthermore, if source B is at the same redshift as 3C 220.3, then the two galaxies could be part of a binary quasar system in the process of merging.

Table 1: 2014 *Chandra* Data, Proposal #15700379, PI Wilkes

OBSID	Date	Exposure (ksec)
16081	2014-07-03	44.49
16082	2014-09-15	19.81
16520	2014-06-16	44.71
16521	2014-06-18	44.49
16522	2014-06-30	44.49

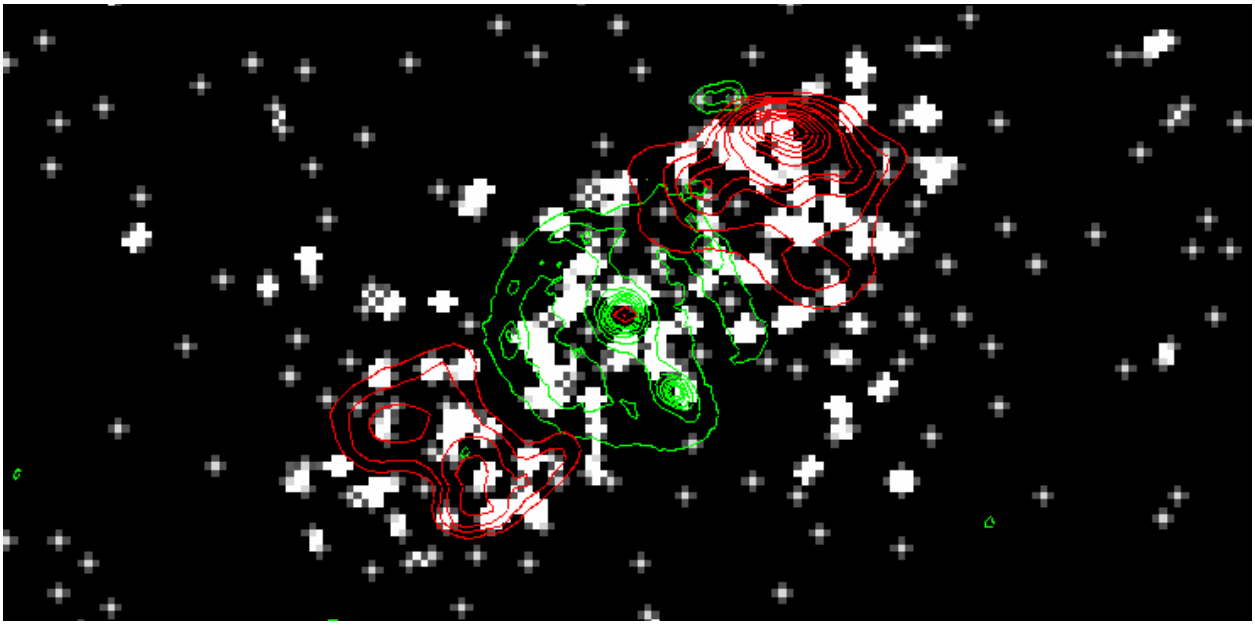

Figure 6: Sub-pixel binned, merged Chandra data of 3C 220.3 taken with ACIS-S3. The data are filtered to the broadband energy range (0.3 - 8 keV) and are binned to eighth-size pixels (0.125 ″). *HST* F160W contours are shown in green and JVLA contours are shown in red.

2.2. *Hubble Space Telescope*

Two archival *HST* images from 1994 were used in previous analyses of 3C 220.3. These images were taken with the F702W filter (702 nm) on UT 1994 March 1 and UT 1995 May 5 for 300 seconds each and show the arc of an Einstein ring to the northeast of the radio galaxy core (Figure 1).[15] The arc is approximately 2.3″ in length with a central angle of 65°. Deeper *HST* data were collected on 3C 220.3 on UT 2014 January 24. The observations were taken with the UVIS detector of the Wide Field Camera 3 (WFC3) in the F814W and F606W filters (814 nm and 606 nm respectively and the with the IR detector of the WFC3 in the F160W filter (1.60 μm). See Table 2 for specifics on the exposures. Figure 7 shows the new *HST* data for the three filters. A full Einstein ring is visible in all three exposures, and the high-resolution F814W and F606W clearly show that source B is located within the radius of the ring and is not part of the lensed SMG.

All of the *HST* images are dithered, and multiple exposures are taken for each filter in order to facilitate the removal of cosmic rays, correct for geometric distortions and background variations, and subsample the data during the reduction stage. Developed for *HST* data, drizzling algorithms like AstroDrizzle combine the dithered images for analysis. The drizzling and cosmic ray rejection for the data from the three *HST* filters was done by our collaborator Christian Leipski in 2014 using AstroDrizzle v.1.1.8, Numpy v.1.8.0, and PyFITS v.3.1.3.dev.

Table 2: 2014 *HST* Data, Proposal #13506, PI Wilkes

Filter	Wavelength	Instrument/Detector	Date	Exposure (sec)
F160W	1536.9176 nm	WFC3/IR	2014-01-24	605.87
F814W	804.810 nm	WFC3/UVIS	2014-01-24	1338.0
F606W	588.555 nm	WFC3/UVIS	2014-01-24	696.0

[15]Sparks, William, 1994, Hubble Space Telescope Cycle 4 Proposal #5476, "Continuum Snapshots of 3CR Radio Galaxies."

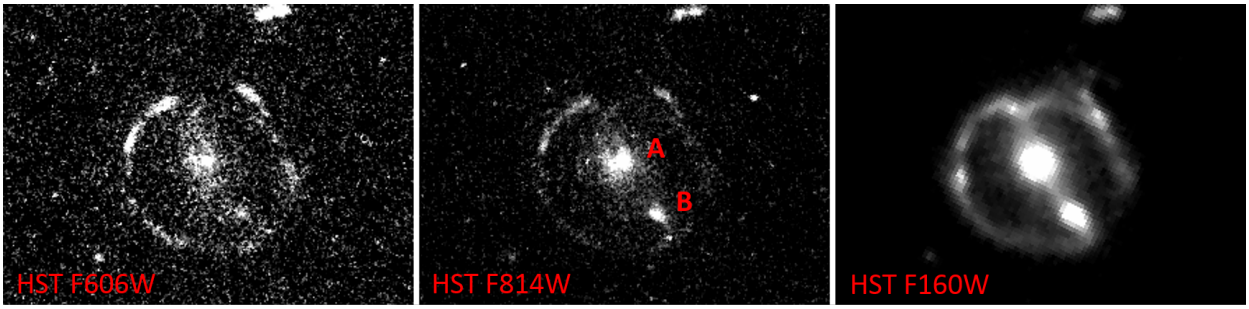

Figure 7: From left to right: Galaxy, source B, and Einstein ring as seen with *HST* with the F160W filter (1.60 μm), F814W filter (814 nm), and F606W filter (606 nm).

2.3. *Jansky Very Large Array*

Located near Socorro, New Mexico, the Karl G. Jansky Very Large Array (JVLA), is a radio interferometer that consists of 27 radio antennas that are each 25 m in diameter. The data obtained for the Haas et al. (2014) paper was collected on UT 2012 November 30 with the A configuration (long-baseline), using 25 of the 27 antennas in the X band (9 GHz).[16] Three components of the 3C 220.3 system are visible in the image: the two radio lobes (called the NW lobe and SE lobe based on orientation) and the AGN core (Figure 8). These 2012 JVLA observations marked the first time the radio core of 3C 220.3 was detected. This analysis uses the contours from this radio data and the fluxes calculated by Haas et al. (2014). Details on the radio data are given in Table 3, More information on the JVLA data are available in Haas et al. (2014).

[16]Barthel, Peter, 2012, Jansky Very Large Array Telescope DDT Proposal VLA/12B-398, "The radio structure of lensing radio galaxy 3C220.3."

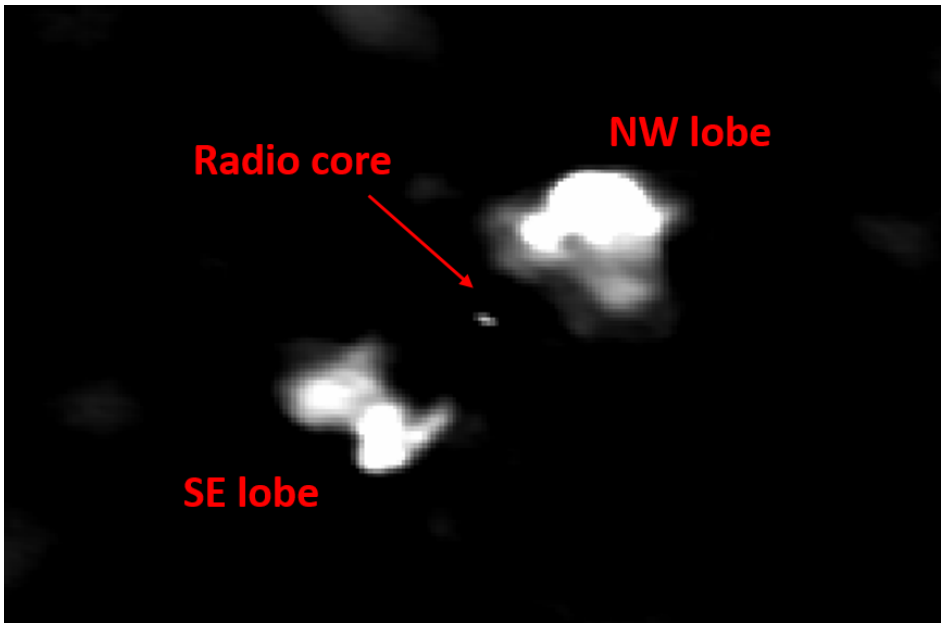

Figure 8: JVLA data of 3C 220.3 with radio core and northwest/southeast radio lobes marked.

Table 3: Radio, Submillimeter, and Infrared Data

Instrument	Config./Detector	Freq./Wavelength	Bandwidth	Date	Exposure
JVLA	A config.	9.00 GHz	2048 MHz	2012-11-30	37 min
SMA	Extended config.	302.927 GHz	8 GHz	2013-01-11	9.6 hr
SMA	Compact config.	302.927 GHz	8 GHz	2013-02-10	6.7 hr
Keck II	NIRC2	2.124 μm		2012-12-24	960.0 s

2.4. *Submillimeter Array*

The SAO Submillimeter Array (SMA) is a radio interferometer comprised of eight 6-meter dishes located atop Maunakea in Hawaii. The array can be rearranged into different configurations with baselines up to 509 m and operates between frequencies of 180 GHz and 418 GHz. After 3C 220.3 was discovered to be a gravitational lens, two exposures were taken by SMA with Director's Discretionary Time (DDT) on UT 2013 January 11 and UT 2013 February 10 in the extended array configuration (226 m baseline) and compact configuration

(76 m baseline), respectively. Specifics of the two exposures are listed in Table 3 and more information can be found in Haas et al. (2014). The two SMA exposures were combined, processed, and analyzed by Haas et al. (2014). The resulting contours and fluxes of 3C 220.3 are used in this analysis. As seen in Figure 1, part of the Einstein ring is visible, as well as part of source B.

2.5. *Keck II Near-Infrared with Adaptive Optics*

Infrared data was collected by the Near Infrared Camera 2 (NIRC2) on the Keck II telescope with DDT on UT 2012 December 24 with laser guide star adaptive optics. Located atop Maunakea, the 10-meter Keck II telescope is able to perform optical and near-infrared imaging and spectroscopy from 0.3 μm to 5 μm and is equipped with both natural guide star (NGS) adaptive optics (Wizinowich et al. 2000) and laser guide star (LGS) adaptive optics (Wizinowich et al. 2006) that correct for atmospheric distortions and improve seeing. The NIRC2 instrument is located behind the Adaptive Optics (AO) bench on Keck II and operates from 1 to 5 μm and can select from three cameras with pixel scales of 10, 20, and 40 milliarcsec/pixel.[17]

Observations of 3C 220.3 were taken in the *K'* band ($\lambda = 2.124$ μm) for a total of 960 seconds. As with *HST* observations, Keck images are dithered, and the observation was broken into nine exposures, each consisting of four, 30-second sub-exposures. The images were processed and analyzed by Haas et al. (2014), and the contours and flux calculations are used in this thesis. In the processed image, both the main galaxy and source B are clearly visible, as well as a significant part of the Einstein ring (Figure 1). Details on the Keck exposure are given in Table 3 and more information on the image reduction and photometry can be found in Haas et al. (2014).

[17]Additional information on the NIRC2 can be found at: https://www2.keck.hawaii.edu/inst/nirc2/

2.6. *Alignment*

As seen in Figure 9, the apparent AGN core in the *HST* and JVLA contours do not align. Additionally, there seems to be X-ray emission that comes from within the Einstein ring as seen by *HST*. In order to determine the appropriate regions from which to extract *Chandra* X-ray counts for flux calculations (see Section 3.1), the radio and optical contours need to be closely aligned for component identification.

Initially, we attempted to align the *HST* images directly with the *Chandra* data by looking for bright, point-like sources to match between frames. Aside from the fact that there are generally few sources that radiate in both X-ray and optical ranges, the field of view is essentially devoid of nearby sources, so the approach was ineffective.

Since the JVLA positions are more accurate than those of *HST*, we shifted the approximate AGN center location in the *HST* data to match the core in the JVLA data. The shifts for each image were obtained manually by measuring the right ascension (RA) and declination (Dec) centroids of the core in the JVLA image and the three optical images in DS9. After converting the RA/Dec differences to decimal degrees (Table 4), we edited the `CRVAL1` and `CRVAL2` in the headers of the *HST* FITS files to align the HST core with that in the EVLA data. Pre- and post-alignment images are shown in Figure 9.

Table 4: Reference pixel shifts[a] for *HST* filters in arcseconds

Filter	CRVAL1 (RA) shift ($''$)	CRVAL2 (δ) shift ($''$)
F160W	-1.3644	+0.12600
F814W	-0.5508	+0.17712
F606W	-0.8028	+0.19296

[a]Shifts are with respect to radio core in the JVLA data.

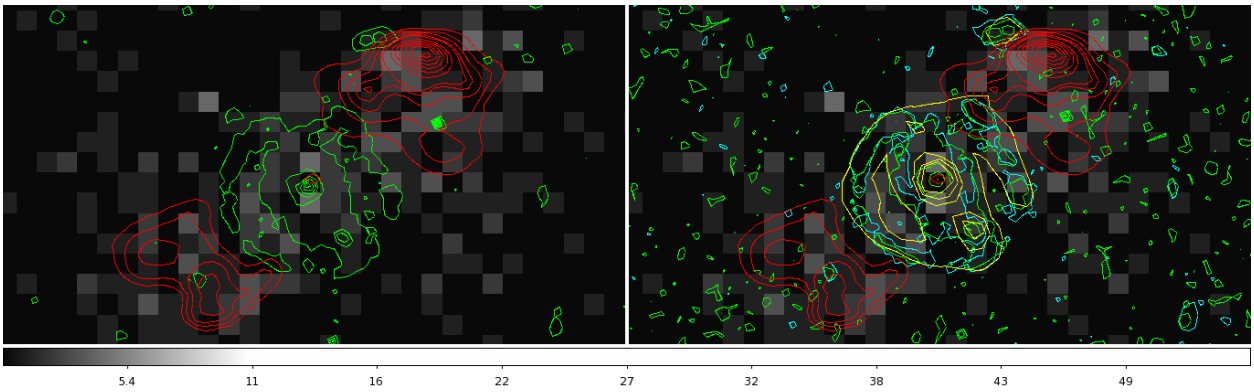

Figure 9: Left: AGN core in F814W *HST* contours (green) are misaligned with core in JVLA contours (red). The background is native pixel (0.5″) *Chandra* data and the field of view is approximately 15″by 8″. Right: AGN core in F160W (yellow), F814W (green), and F606W (cyan) *HST* contours are aligned with core in JVLA contours (red). The background is native pixel (0.5″) *Chandra* data and the field of view is approximately 15″by 8″.

3. ANALYSIS

Methods of analysis for X-ray astronomy are inherently different than those for other areas of astronomy. Unlike its counterparts, which have very large numbers of photons, the majority of X-ray sources rely on few counts but record detailed information for each captured photon. The spatial resolution of *Chandra* is 0.5″, which is comparable to the resolution of ground-based optical telescopes in conditions with good seeing. The native pixel size of the ACIS instrument used for imaging 3C 220.3 is 0.492″. To properly sample the PSF of a target, *Chandra* dithers in a Lissajous figure around the *nominal aimpoint* (the pixel coordinates of the target) on the detector (see Figure 10 for example). The default dither pattern for observations with the ACIS detector are 16″ peak-to-peak in the Y and Z directions. Since the dither pattern is recorded in the aspect solution file, the position of each photon can be determined more accurately than the size of a pixel when the sky pointing is reconstructed during data processing. This information can be accessed by *sub-pixel binning* the data. Different sub-pixel binnings (e.g. quarter- or eighth-size with respect to the native pixel) can be used, depending on the size of the target in the image and what features are being highlighted. Figure 11 shows the full-frame image of that was taken when observing 3C 220.3, and Figure 12 gives a visual example of sub-pixel binning (0.5″ vs. 0.125″).

In the sub-pixel binned data (Figures 12 through 15), there are several possible structures worth noting. First, there appears to be a ring-like structure in the X-rays close to the radius of the optical Einstein ring (see overlap with *HST* contours in Figure 6). If this is real, it would indicate that there are X-rays being emitted from SMMJ0939, which would be consistent with the AGN breakout suggested by Haas et al. (2014) as a result of their lens modeling (Section 1.6). There also seem to be X-ray photons that coincide with the *HST* contours for source B (see Figure 6), which could indicate that source B has an AGN. Although the true redshift of source B is unknown, if it is the same redshift as 3C 220.3

(discussed in Haas et al. (2014)), then 3C 220.3 and source B could be a binary quasar/AGN system that is in the process of merging.

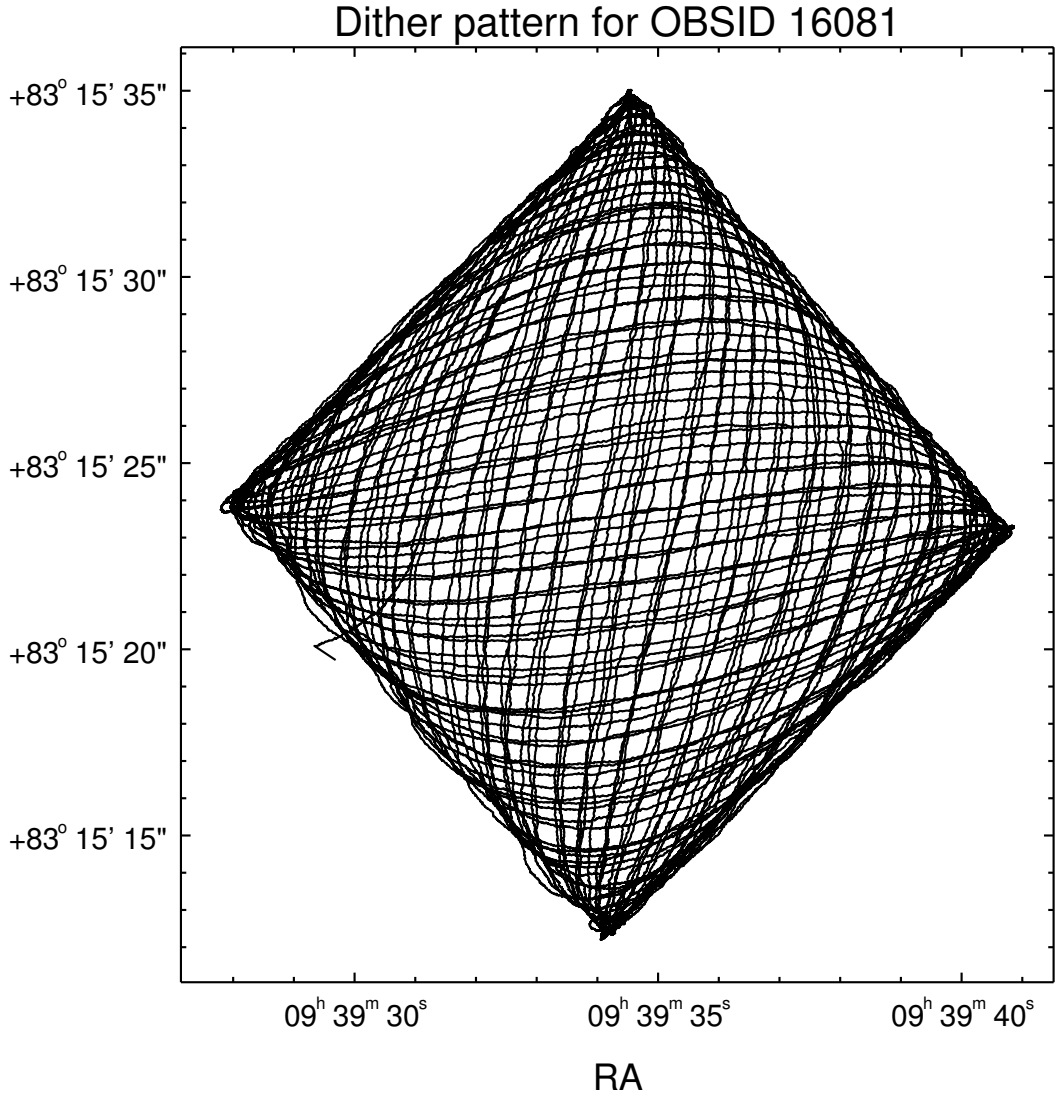

Figure 10: Lissajous dither pattern for *Chandra* data set OBSID 16081

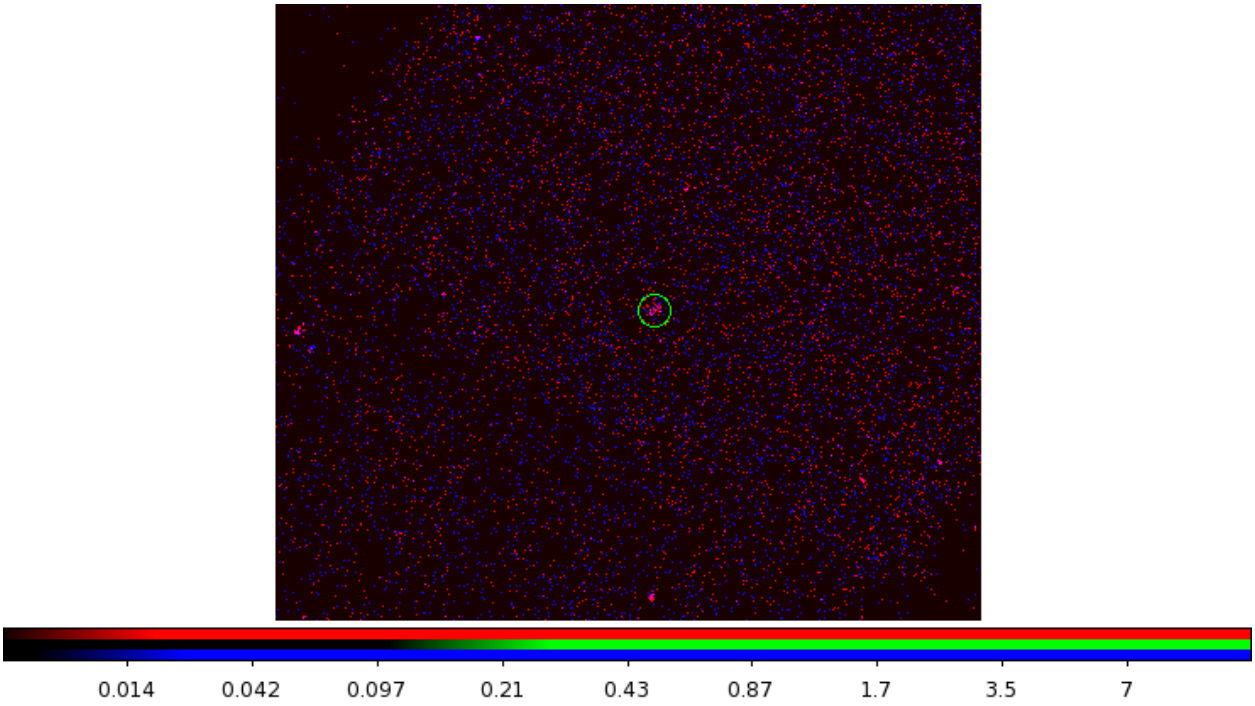

Figure 11: Full-frame, merged ACIS-S3 image of the five *Chandra* data sets (native pixel size, 0.3 - 8 keV). 3C 220.3 is marked by the green circle (12″ radius). Red indicates soft, low-energy X-rays (0.3 - 2 keV) and blue indicates hard, high-energy X-rays (2 - 8 keV).

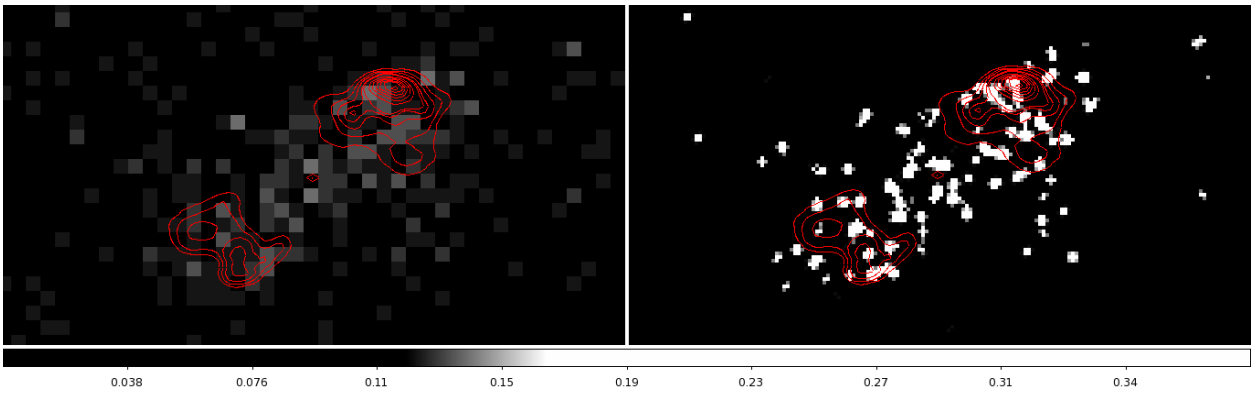

Figure 12: Comparison between *Chandra* native pixel binning (left) and eighth-size sub-pixel (0.125″) binning with smoothing (right). Smoothing is Gaussian with parameters $r = 2$ and $\sigma = 1.5$. The red contours are the JVLA radio contours for reference and scale. The data are filtered to the broadband energy range (0.3 - 8 keV).

3.1. *Contours and Regions*

The X-ray fluxes of different parts of the 3C 220.3 system are essential to understanding the structure and processes of the X-ray-producing areas. For a full discussion of the various components of 3C 220.3, see Chapter 1. With the presence of two radio lobes, an AGN core, an Einstein ring of a lensed SMG, and a source B of unknown redshift, however, the X-ray analysis of the 3C 220.3 system is unusually complex. The Einstein ring from the lensed SMG, which is visible in optical and infrared observations, has a radius of approximately $2''$ and overlaps with parts of the radio lobes. Additionally, the X-rays appear to originate all over the source, rather than in localized areas, which makes it difficult to determine which pixels correspond to which components. To overcome this, we overlay the contours from the other wavelength data sets, namely the JVLA radio contours and *HST* contours to determine the appropriate regions from which to extract the X-ray counts. The Keck and SMA contours are also useful, although they have lower spatial resolution. These regions are then used to extract the X-ray counts for each component in order to perform aperture photometry and spectroscopy on the X-ray data.

The following regions defined for the flux calculations are determined based on the visible components in the radio and optical contours: AGN core (radio/optical), Einstein ring (optical/infrared), galaxy with and without AGN core (optical/infrared/radio), NW radio lobe (radio), SE radio lobe (radio), source B (optical), AGN core with standard $1''$ radius circle region (radio/optical), and source B with standard $1''$ circle region (optical). Since the resolution of *Chandra* is similar to that of Keck and the *HST* F160W observations, the lower resolution data were used to define the Einstein ring region as an elliptical annulus with an average thickness of $0.86''$ (labeled "Einstein ring (thin)" in Table 5). To avoid contamination from counts from the galaxy and radio lobes, a thickness of $0.86''$ was the maximum annulus thickness we could use.

However, since the above regions are also used in the optical analysis, a second Einstein region with a thinner annulus with average thickness 0.79″ (labeled "Einstein ring (thick)" in Table 5) was also defined to take advantage of the higher resolution optical data. The 1″ circle regions are used as a secondary measure for the AGN and source B since the components are small regions with low counts and are used as the standard region size for PSFs in *Chandra* analysis. As with the thin Einstein ring region, the elliptical source B region is used for the optical analysis. Detailed parameter information for the regions used is available in Table 5 and images of the regions are shown in Figures 13 through 15.

Since sources A and B are very close together ($\sim$ 1.5″ apart), contamination between regions may seem like a concern. However, with an average off-axis angle of approximately 0.32′, only 10 to 15% of the counts from a point source will lie outside a 1″ radius.[18] Given that the counts for both the standard 1″ circles and ellipses (which are just under 1″ in size) for the core and source B are less than 20 and 10 counts respectively (Table 7), this corresponds to a maximum of 2 to 3 counts outside those regions. The overlap between the 1″ circles of the core and source B is approximately 0.4 square arcseconds. This results in a $\sim$ 0.1 count of contamination between the two regions, and so we can assume the contamination is negligible.

[18]Based on Figure 4.23 in the *Chandra* POG (http://cxc.harvard.edu/proposer/POG/html/chap4.html).

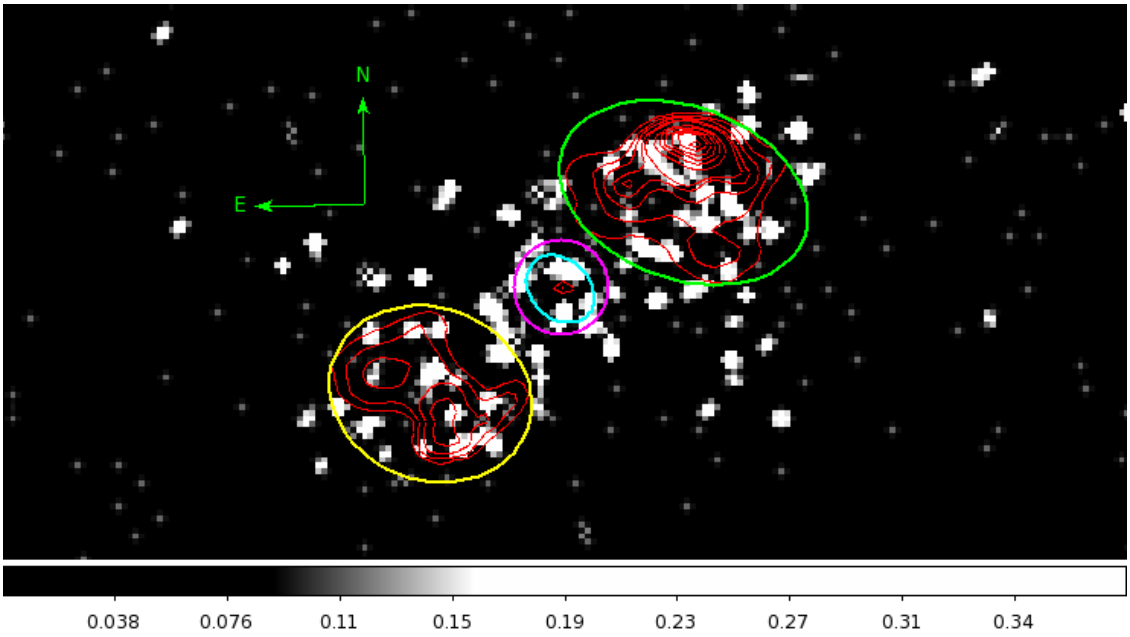

(a) Image showing the following regions: NW radio lobe (green), SE radio lobe (yellow), AGN core (elliptical region, cyan), AGN core (1″ circle, magenta). Radio contours red are shown in red and the background is *Chandra* data (0.3 - 8 keV) with eighth-size sub-pixel binning and Gaussian smoothing ($r = 2$, $\sigma = 1.5$).

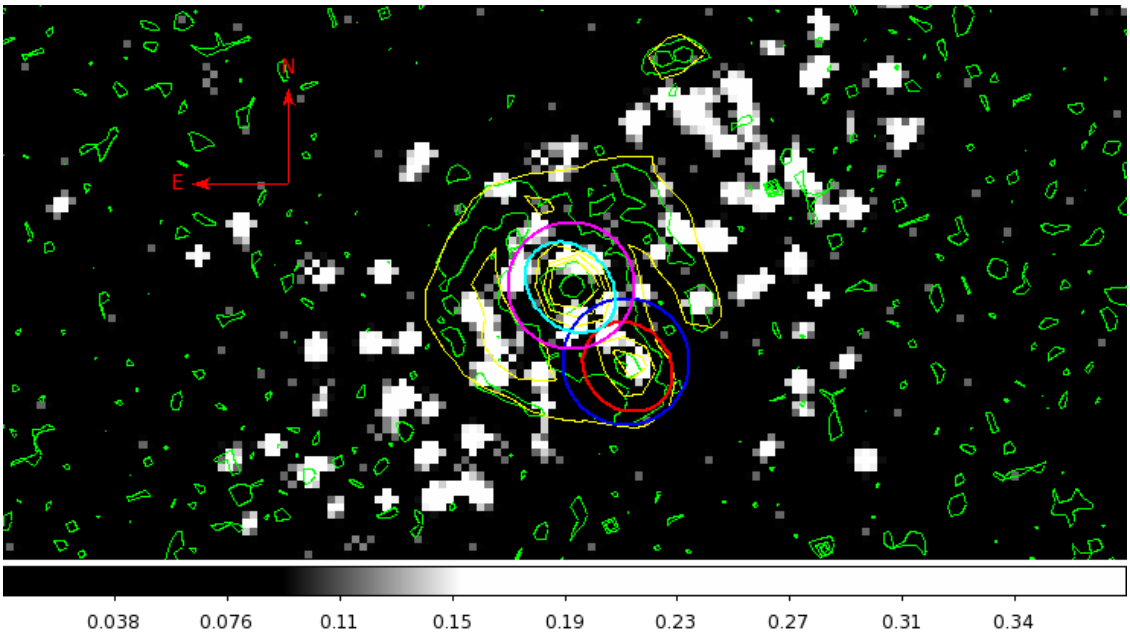

(b) Image showing the following regions: AGN core (elliptical region, cyan), AGN core (1″ circle, magenta), source B (elliptical region, red), source B (1″ circle, blue). *HST* contours are shown in yellow (F160W) and green (F814W). The background is *Chandra* data (0.3 - 8 keV) with eighth-size sub-pixel binning and Gaussian smoothing ($r = 2$, $\sigma = 1.5$).

Figure 13: Count extraction regions used in the X-ray data analysis.

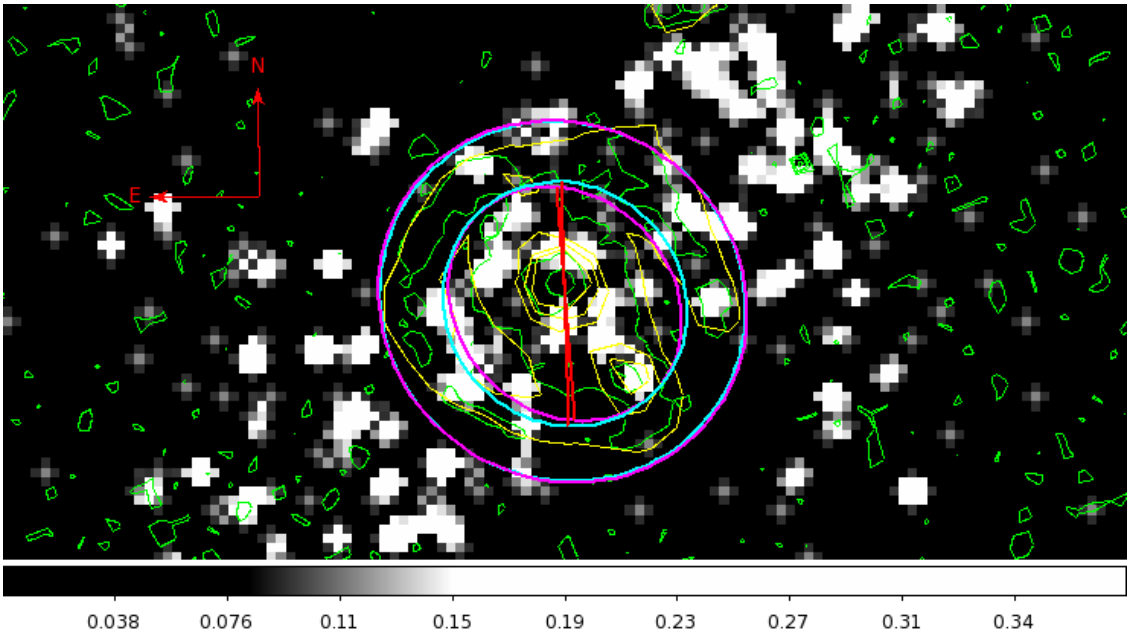

(a) Image showing the following regions: Einstein ring (thick), magenta) and Einstein ring (thin, cyan). The red slashes at the center indicate an excluded region. *HST* contours are shown in yellow (F160W) and green (F814W). The background is *Chandra* data (0.3 - 8 keV) with eighth-size sub-pixel binning and Gaussian smoothing ($r = 2$, $\sigma = 1.5$).

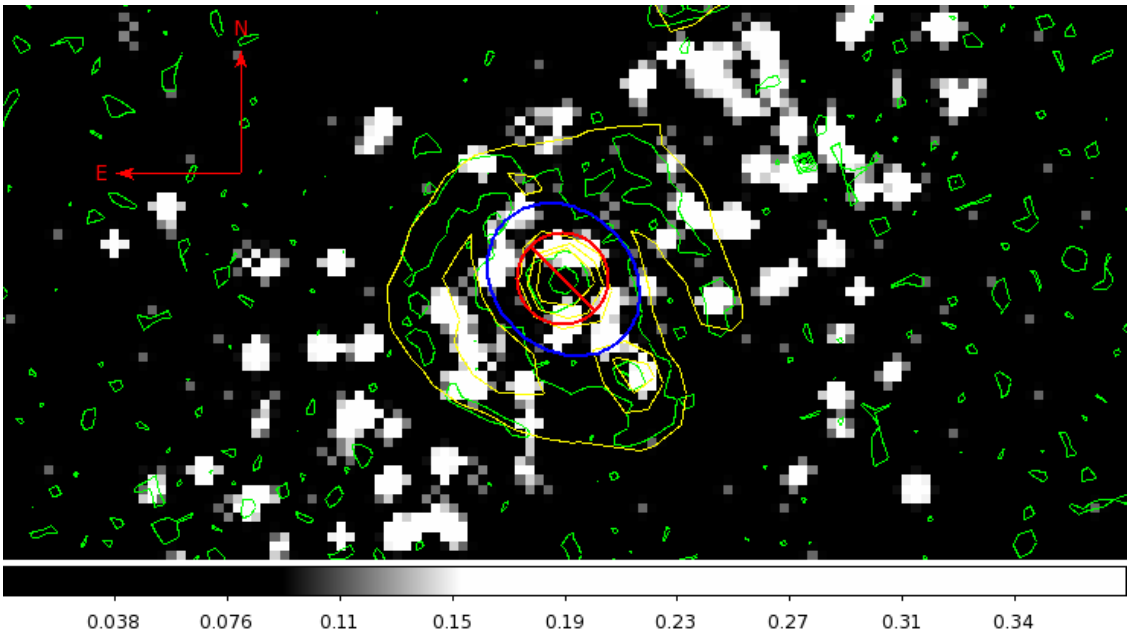

(b) Image showing the following regions: galaxy with AGN core (blue ellipse without red region) and galaxy without AGN core (blue ellipse less the red circular regions with a slash). *HST* contours are shown in yellow (F160W) and green (F814W). The background is *Chandra* data (0.3 - 8 keV) with eighth-size sub-pixel binning and Gaussian smoothing ($r = 2$, $\sigma = 1.5$).

Figure 14: Count extraction regions used in the X-ray data analysis.

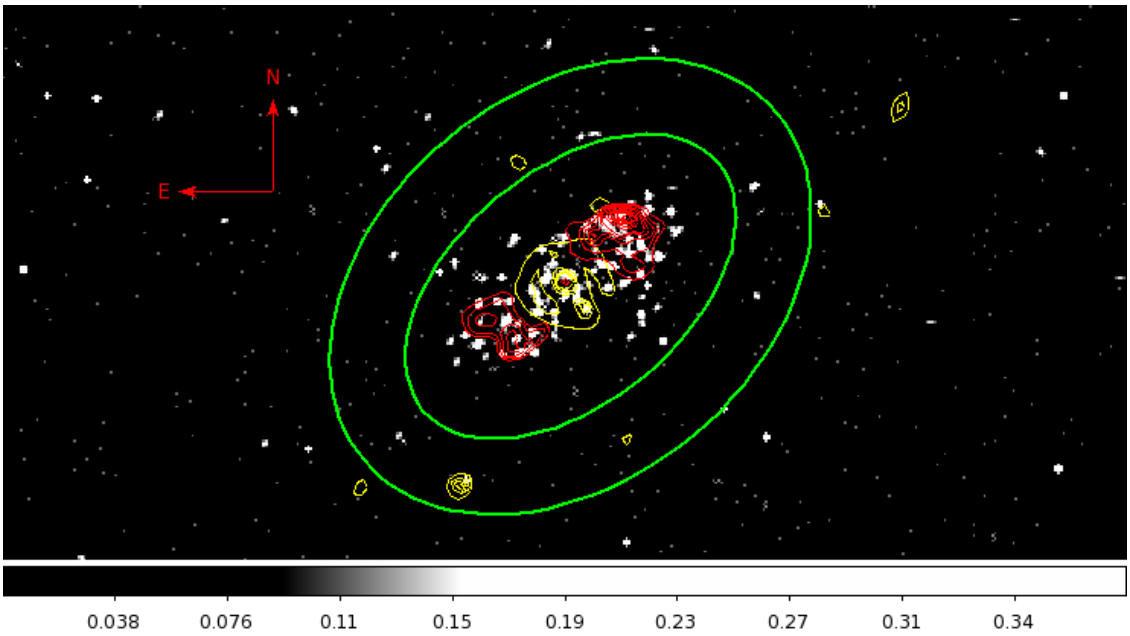

(a) Image showing the following regions: background region (elliptical annulus, green). Radio contours are shown in red and *HST* F160W contours are shown in yellow. The background is *Chandra* data (0.3 - 8 keV) with eighth-size sub-pixel binning and Gaussian smoothing ($r = 2$, $\sigma = 1.5$).

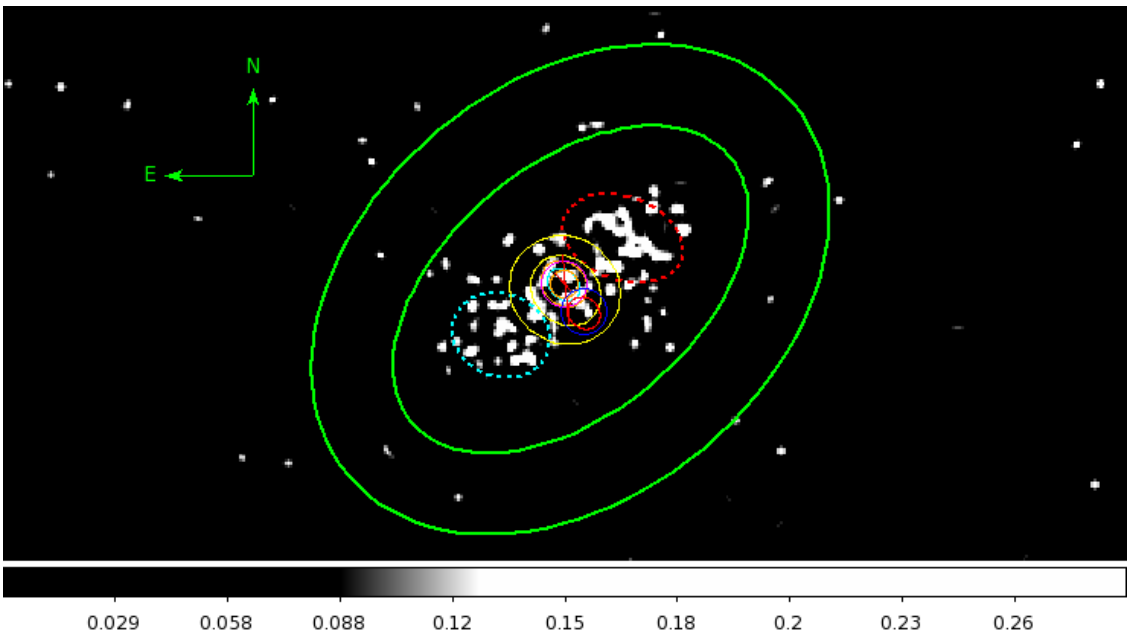

(b) Image showing all regions used the X-ray analysis, combining Figures 13, 14, and 15(a). The background is *Chandra* data (0.3 - 8 keV) with eighth-size sub-pixel binning and Gaussian smoothing ($r = 2$, $\sigma = 1.5$).

Figure 15: Count extraction regions used in the X-ray data analysis.

Table 5: Region parameters for X-ray flux analysis[a]

Region name	Region type	Position (RA and Dec, FK5)	Dimensions	PA[b]
	Elliptical	9:39:23.6892 +83:15:25.621	18.90″/9.00″	
Background	annulus	9:39:23.6892 +83:15:25.621	9.00″/5.40″	130°
Core	Ellipse	9:39:23.8653 +83:15:25.828	0.79″/0.61″	45°
	Elliptical	9:39:23.8321 +83:15:25.600	2.46″/2.30″	145°
Einstein ring (thick)	annulus	9:39:23.8134 +83:15:25.567	1.63″/1.40″	45°
	Elliptical	9:39:23.8321 +83:15:25.600	2.46″/2.30″	145°
Einstein ring (thin)	annulus	9:39:23.8134 +83:15:25.567	1.64″/1.54″	45°
	Ellipse with	9:39:23.8509 +83:15:25.864	1.08″/0.90″	
Galaxy (no core)	circular hole	9:39:23.8509 +83:15:25.864	0.60″	45°
Galaxy (with core)	Ellipse	9:39:23.8509 +83:15:25.864	1.08″/0.90″	45°
NW lobe	Ellipse	9:39:22.3978 +83:15:27.843	2.70″/1.80″	70°
SE lobe	Ellipse	9:39:25.4113 +83:15:23.636	1.80″/2.16″	70°
Source B	Ellipse	9:39:23.3578 +83:15:24.588	0.65″/0.75″	45°
Core (1″ circ.)	Circle	9:39:23.8509 +83:15:25.864	1.00″	
Source B (1″ circ.)	Circle	9:39:23.3666 +83:15:24.653	1.00″	

[a]For annular regions, the first line refers to the outer shape and the second line refers to the inner shape. Dimension entries that are a pair of numbers separated by a slash indicate the semi-major and semi-minor axes of an ellipse.

[b]PA, or Position Angle, is defined as the degrees east of north.

3.2. *BEHR Hardness Ratios*

In optical astronomy, *color* can be a useful measure in understanding the properties of various objects, as in a Hertzsprung–Russell diagram for stellar and cluster ages. The *hardness ratio* is the X-ray astronomy equivalent, but instead of calculating it from the magnitudes in different wavelengths, it is calculated by the number of counts in the "soft" and "hard" energy ranges. We adopt energy ranges of 0.3 - 2 keV and 2 - 8 keV for the soft and hard X-ray bands, respectively. These are typical for *Chandra*, since above 8 keV, the X-ray background is very high and makes it difficult to do analyses. For sources with low counts, the hardness ratio (HR) is particularly useful in understanding the emission mechanisms and obscuration of a source. There are three types of hardness ratios (described in Park et al.

(2006)) simple, color, and fractional difference:

$$\mathcal{R} = \frac{S}{H} \tag{4}$$

$$\mathcal{C} = \log_{10}\left(\frac{S}{H}\right) \tag{5}$$

$$\mathcal{HR} = \frac{H - S}{H + S} \tag{6}$$

Since 3C 220.3 has very few X-ray counts, we use the fractional difference ($\mathcal{HR}$) as our measure of hardness. A more detailed discussion of when to use the three measures can be found in Park et al. (2006). To calculate the hardness ratios, we used the Fortran- and C-based program BEHR (Bayesian Estimation of Hardness Ratios). Using the X-ray count extraction regions listed in Table 5, BEHR performs a background subtraction and calculates errors for the hardness ratios.

The hardness ratios calculated for the regions are given in Table 6. Figure 16 shows the calculated values in comparison to the predicted hardness ratio based on PIMMS simulations. We can see that all of the entries are negative, which means that overall, the components of 3C 220.3 have soft X-ray emission. For comparison, the hardness ratios for an unobscured AGN with a typical slope of $\Gamma \sim 1.9$ range from $\mathcal{HR} \sim -0.5$ (for quasars) to $-0.7 < \mathcal{HR} < 0.7$ (for NLRGs) (Wilkes et al. 2013). Since soft X-rays are lower energy X-rays, they are quickly absorbed by surrounding mediums, and so the detection of soft counts indicates an unobscured region. Conversely, when a source is obscured, we expect hard X-rays to dominate. As a result, the hardness ratio should increase as a source becomes more obscured. Since edge-on (or approximately edge-on) NRLGs like 3C 220.3 are highly obscured (see Section 1.2), the hardness ratio for the AGN core should be higher.

As shown in Figure 16, the predicted hardness ratios from the PIMMS calculator indicate that soft X-ray spectra correspond to material with low column density (i.e. low redshifted N_H values). While this may seem contradictory to the high column density of a Compton thick source, the soft X-ray counts can originate from either X-ray scattering off electrons

near the AGN core or from some extended, unobscured structure farther away from the core. In the first case, the scattered X-rays are not affected by absorption (since they are scattered), which results in an apparently low N_H. In the second case, emission from an extended and more diffuse component becomes visible when the stronger emission from the core is obscured by Compton-thick material. Since we see almost no counts from the AGN core itself (e.g. Figure 13) and since the counts we do see are soft, we believe the AGN core of 3C 220.3 is Compton thick. This softness is consistent with what has been found in other low X-ray flux, edge-on, Compton-thick NLRGs in the 3CR sample (Wilkes et al. 2013).

Table 6: Hardness ratios (median value and asymmetric lower and upper bounds)[a]

Region	Hardness	Lower Bound	Upper Bound
Core	-0.61	-0.85	-0.41
Einstein ring (thick)	-0.69	-0.85	-0.55
Einstein ring (thin)	-0.72	-0.94	-0.59
Galaxy (no core)	-0.67	-0.90	-0.51
Galaxy (with core)	-0.531	-0.73	-0.37
NW lobe	-0.32	-0.45	-0.20
SE lobe	-0.46	-0.58	-0.30
Source B	-0.74	-1.00	-0.57
Core ($1''$ circle)	-0.36	-0.58	-0.15
Source B ($1''$ circle)	-0.53	-1.00	-0.36

[a]The corresponding counts for these regions are listed in Table 7.

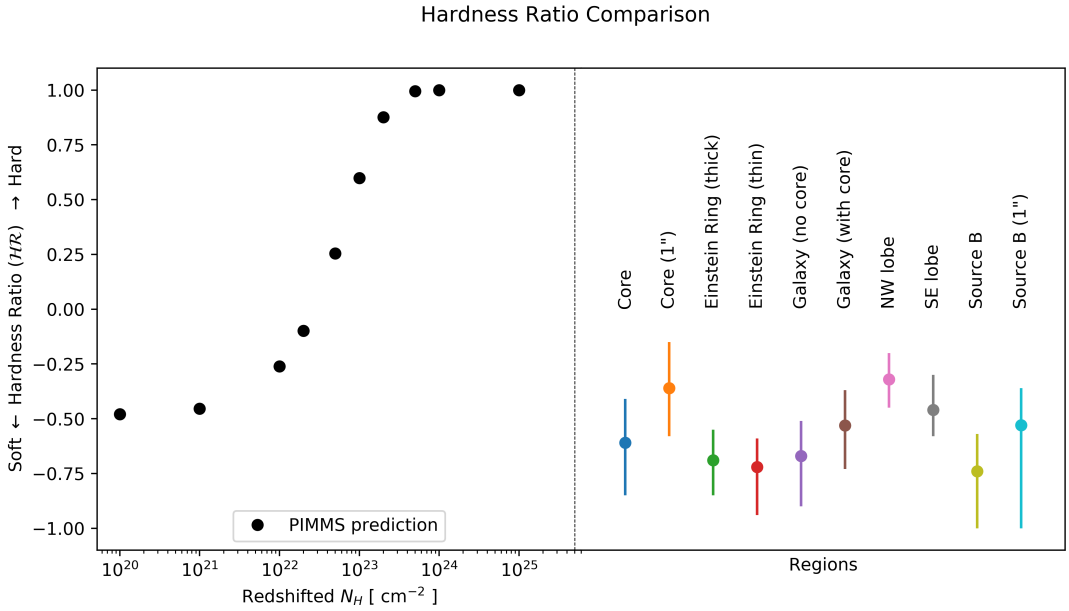

Figure 16: Comparison of predicted hardness ratios for various redshifted N_H values[a] (left, black points) to the calculated hardness ratios (Table 6) for the various regions (right, colored points).

[a]The predicted values were calculated with the PIMMS calculator (http://cxc.harvard.edu/toolkit/pimms.jsp) for the Cycle 16 Mission on the ACIS-S (with no grating or filter) with input energies from 0.3 - 10 keV. Output energy bands were defined to be either soft (0.3 - 2 keV) or hard (2 - 8 keV). We used a power law model with a galactic N_H of 3.26×10^{20} cm^{-2}, redshift of $z = 0.685$, photon index of $\Gamma = 1.9$, and count rate of 0.0001 counts per second. We varied the redshifted N_H values from 10^{20} cm^{-2} to 10^{25} cm^{-2} to determine the predicted hard and soft counts for the hardness ratio calculation (Equation 6).

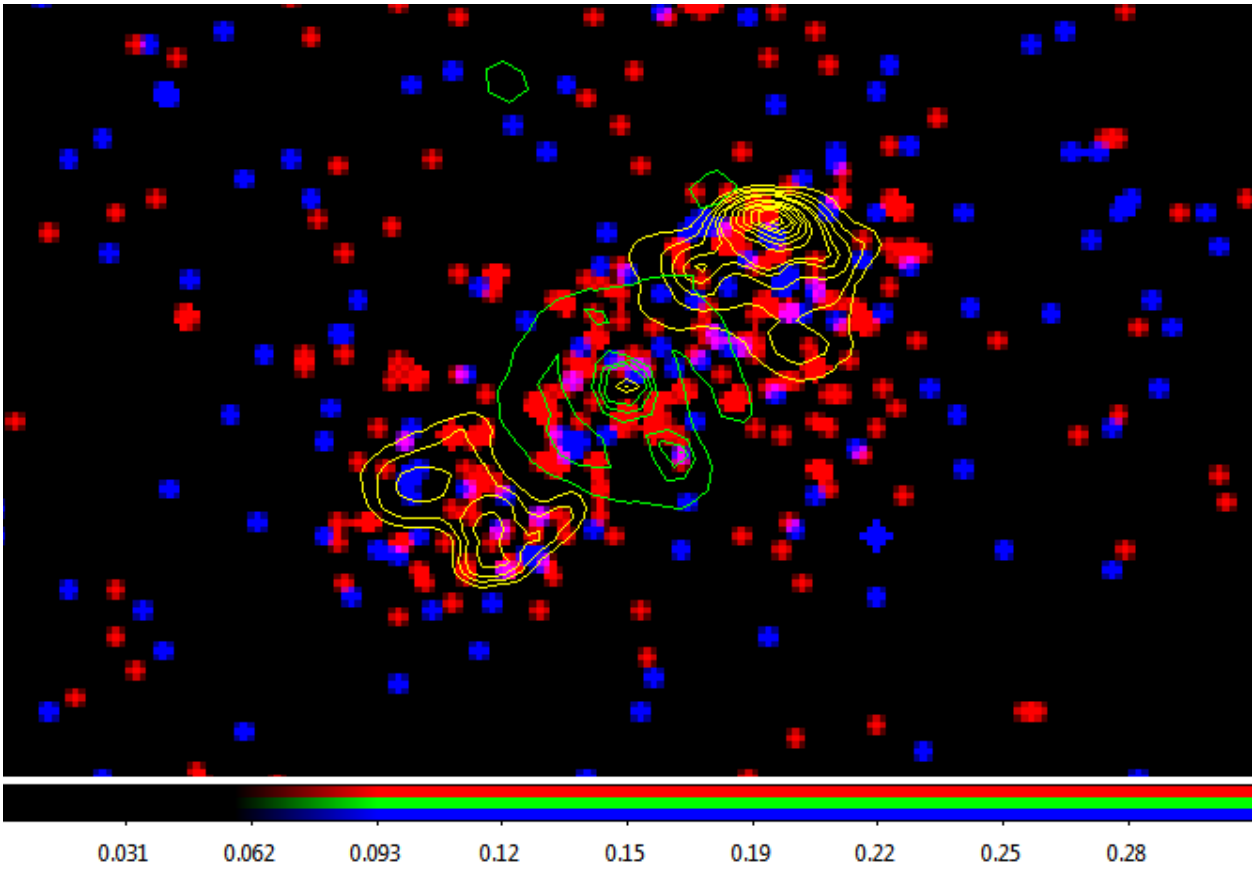

Figure 17: *Chandra* image of 3C 220.3 showing the soft X-rays (red, 0.3 - 2 keV) and hard X-rays (blue, 2 - 8 keV). Radio contours are shown in yellow and *HST* F160W contours are shown in green. The data are eighth-size sub-pixel binned and Gaussian smoothed ($r = 2$, $\sigma = 1.5$).

3.3. CIAO *Analysis*

Developed by the *Chandra* X-Ray Center (CXC), CIAO is a software package designed for analyzing *Chandra* data (Fruscione et al. 2006). In addition to its own version of DS9, which has certain X-ray specific tools, it has many analysis tools for extracting counts and spectra, fitting spectra with one or more standard X-ray components, and calculating fluxes with the appropriate X-ray statistics, among other tasks. For the X-ray analysis in this thesis, we used CIAO v.4.10.

3.3.1. *Count extraction with* `dmextract`

The flux values for the regions (Section 3.1) are calculated using both the Sherpa spectral fit method and the `srcflux` single-bin method (discussed in Sections 3.3.2 and 3.3.3). For regions with low counts (e.g. less than 10 photons), the `srcflux` tends to give a more reliable calculation.

To aid in determining these appropriate flux values, the CIAO tool `dmextract` is useful. Table 7 lists the count numbers and errors, as well as the background-subtracted counterparts for each of the regions defined in Section 3.1. The net counts and errors are calculated in `dmextract` as follows:

$$C_{net} = C_{reg} - \left(\frac{A_{reg}}{A_{bkg}} \cdot \mathrm{C}_{bkg}\right) \tag{7}$$

$$\sigma_{net} = \sqrt{\sigma_{reg}^2 + \left(\frac{\mathrm{A}_{reg}}{\mathrm{A}_{bkg}} \cdot \sigma_{bkg}\right)^2} \tag{8}$$

where C_{reg}, σ_{reg}, and A_{reg} are the respective counts, error, and pixel area extracted from a region and C_{bkg}, σ_{bkg}, and A_{bkg} are the respective counts, error, and pixel area of the background region.

3.3.2. Sherpa *Spectral Analysis*

Since 3C 220.3 has very low counts, it is difficult (and not always particularly useful) to try to fit a spectral model to the data for certain regions (such as the core or source B). For these cases, the tool `srcflux` is used (Section 3.3.3). Nonetheless, the visualization and

Table 7: Region counts and errors with background subtraction.

Region name	Counts	Error	Area [a]	Area ratio[b]	Net counts	Net error
Background	101.0	10.05	841.38			
Core	14.0	3.74	6.29	133.8	13.24	3.74
Einstein ring (thick)	38.0	6.16	44.19	19.0	32.70	6.19
Einstein ring (thin)	29.0	5.39	39.13	21.5	24.30	5.41
Galaxy (no core)	16.0	4.0	7.94	106.0	15.05	4.00
Galaxy (with core)	24.0	4.90	12.61	66.7	22.49	4.90
NW lobe	72.0	8.49	63.07	13.3	64.43	8.52
SE lobe	53.0	7.28	50.46	16.7	46.94	7.31
Source B	6.0	2.45	6.33	132.9	5.24	2.45
Core (1″ circ.)	21.0	4.58	12.94	65.0	19.45	4.59
Source B (1″ circ.)	10.0	3.16	12.98	64.8	8.44	3.17

[a]Areas are given in units of pixels.
[b]Area ratio is defined as the ratio of the background area (in pixels) to the region area (in pixels).

parameters from spectral fits with Sherpa (Freeman et al. 2001) can be useful in determining whether there are particular counts or energy ranges that are skewing the fit. For 3C 220.3, we assume a power law model with galactic absorption (N_H). In X-ray astronomy, N_H is called the *equivalent* hydrogen column number density, since the X-ray absorption by the galaxy is dominated by heavy elements, rather than hydrogen.[19] The resulting spectral model is:

$$N(E) = A \left(\frac{E}{E_{\rm ref}} \right)^{-\Gamma} e^{-N_H \sigma(E)} \tag{9}$$

where A is the normalization amplitude (typically the flux at 1 keV), E is the energy, $E_{\rm ref}$ is a normalization factor, Γ is the photon index and slope,[20] N_H is the equivalent hydrogen column density, and $\sigma(E)$ is the photoelectric cross section. Since we have relatively few

[19]When converting to N_H, solar abundances are assumed.
[20]The photon index, Γ, is defined as α+1, where α is the spectral index, or the slope of the graph in a log/log energy spectrum plot. Γ is the slope of the power law component of the $N(E)$ function in the energy spectrum plot.

counts, we do not try to fit the slope of the spectrum; rather, we fix the photon index value and shift the spectrum up and down to find the best flux calculation. For active galaxies, the photon index is typically fixed to $\Gamma = 1.9$ because the measured slopes show a narrow distribution around this value (Ishibashi & Courvoisier 2010).[21] The N_H value for 3C 220.3 is 3.26×10^{20} atoms/cm^2.[22]

Sherpa is the main modelling and fitting package within the CIAO suite. It has the option of pre-defined functions, as well as user-defined ones, and is able to calculate confidence intervals, among other things. The power law/absorption model discussed above can be specified with the `powlaw1d` and `xsphabs` functions.

Before attempting to fit data with Sherpa, the spectra must be extracted from the background and source regions (e.g. core, NW lobe, etc.), which is done using the CIAO tool `specextract`. However, since `specextract` only works on event data sets (rather than merged data sets) because the calibration is different for each observation and it must generate an RMF and ARF file for each extracted dataset, we cannot combine the five *Chandra* observations before extracting the spectrum. As a result, we first perform the spectra extraction on the individual data sets (which produces the OBSID-specific response files). The tool `combine_spectra` then uses the response files of the individual datasets to merge the five spectra into a single one, which can be inputted to Sherpa for fitting.

We can judge the goodness of the resulting fits by looking at several aspects: the fit parameters, the confidence intervals, and how well the spectral shape fits the data points. In each spectrum, we specify a bin number, which refers to the minimum number of photons per bin. Sherpa determines the bin sizes needed to achieve this. For fits in which the data

[21] This photon index corresponds to a spectral index of $\alpha = -0.9$ for a power law in the form of $F_\nu \propto C \cdot \nu^\alpha$. We find this estimated value for 3C 220.3 to be consistent with the best-fit spectral index for the radio continuum in Section 4.4, where the emissions from synchrotron and inverse-Compton scattering in the radio lobes are expected to have the same spectral index.

[22] The N_H value for 3C 220.3 was found using the Colden Galactic Neutral Hydrogen Density Calculator (http://cxc.harvard.edu/toolkit/colden.jsp) with NRAO data compilation by (Dickey & Lockman 1990).

appears to have many spikes or appears to go outside the specified energy range, a larger bin size should be used. See Figure 18 for an example. Typically, odd-numbered bin sizes work well.

In general, the lowest energy bin (corresponding to 0.3 keV) seemed to be consistently higher than expected in all of the graphs, which pulls the fit up at low energies. This type of behavior is not unexpected, since *Chandra*'s low energy measurements have greater errors due to the rapidly decreasing effective area at low energies. As a result, we performed our fits for the broadband energy range from 0.5 keV to 8 keV, rather than from 0.3 keV to 8 keV. The calculated fluxes and their errors for the regions with bin sizes of 3 and 5 are given in Tables 8 and 9.

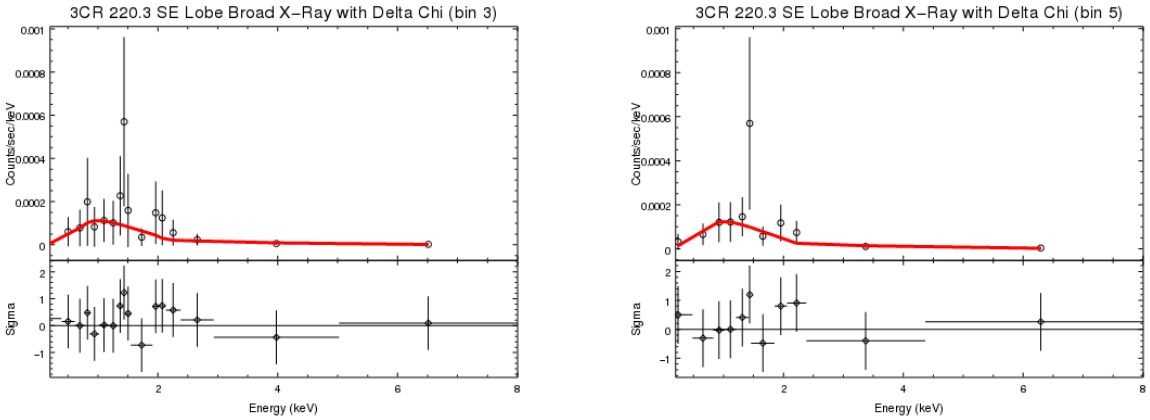

Figure 18: Left: Sherpa fit of SE radio lobe with bin size 3. The upper plot shows the data in counts per second per keV as a function of energy, with a minimum of 3 counts per bin in black and the fitted spectrum in red. The lower plot shows the residuals of the fit plotted in term of the $\Delta\chi$ residuals (residuals/uncertainty). Right: Sherpa fit of SE radio lobe with bin size 5. The upper plot shows the data in counts per second per keV as a function of energy, with a minimum of 5 counts per bin in black and the fitted spectrum in red. The lower plot shows the residuals of the fit plotted in term of the $\Delta\chi$ residuals (residuals/uncertainty).

Table 8: Sherpa spectral analysis fluxes (bin 3) from 0.5 keV to 8 keV.

Region name	Model Flux (erg/cm^2/s)[a]	68% Conf. Interval
Core	2.242e-15	(1.128e-15, 3.167e-15)
Einstein ring (thick)	1.264e-15	(7.953e-16, 1.772e-15)
Einstein ring (thin)	1.177e-15	(6.497e-16, 1.565e-15)
Galaxy (no core)	1.586-e15	(6.926e-16, 2.315e-15)
Galaxy (with core)	1.363e-15	(7.851e-16, 1.766e-15)
NW lobe	1.838e-15	(2.442e-15, 1.129e-15)
SE lobe	1.640e-15	(2.157e-15,1.168e-15)
Source B	8.873e-16	(3.234e-16, 1.587e-15)
Core ($1''$ circle)	1.035e-15	(6.052e-16, 1.496e-15)
Source B ($1''$ circle)	6.634e-16	(3.443e-16, 1.024e-15)

[a]Fluxes calculated assuming a power-law spectral form with $\Gamma = 1.9$ and the galactic N_H towards 3C 220.3 of 3.26×10^{20} atoms/cm^2 (calculated using Colden[22])

Table 9: Sherpa spectral analysis fluxes (bin 5) from 0.5 keV to 8 keV.

Region name	Model Flux (erg/cm^2/s)[a]	68% Conf. Interval
Core	2.727e-15	(1.203e-15, 3.473e-15)
Einstein ring (thick)	1.271e-15	(7.645e-16, 1.717e-15)
Einstein ring (thin)	1.225e-15	(7.404e-16, 1.749e-15)
Galaxy (no core)	1.601e-15	(8.098e-16, 2.278e-15)
Galaxy (with core)	1.419e-15	(9.254e-16, 1.797e-15)
NW lobe	2.120e-15	(1.744e-15, 2.851e-15)
SE lobe	1.790e-15	(1.336e-15, 2.145e-15)
Source B	6.884e-16	(2.894e-16, 1.541e-15)
Core ($1''$ circle)	1.348e-15	(8.393e-16, 1.781e-15)
Source B ($1''$ circle)	5.766e-16	(2.398e-16, 9.080e-16)

[a]Fluxes calculated assuming a power-law spectral form with $\Gamma = 1.9$ and the galactic N_H towards 3C 220.3 of 3.26×10^{20} atoms/cm^2 (calculated using Colden[22])

3.3.3. *Determining X-ray Flux using* `srcflux`

As mentioned at the beginning of Section 3.3.2, spectral fitting with Sherpa is not useful when a region extracts only a few counts (e.g. fewer than 10 photons). In this case, the CIAO tool `srcflux` is effective, since it groups all of the counts into one bin and fits the flux with the same model used in Section 3.3.2. However, like `specextract`, `srcflux` is incapable of processing merged events files. Ideally, we would be able to use the outputs from the `combine_spectra` operation described in Section 3.3.2, but `srcflux` also requires a FITS file in addition to the outputted response files. Since it will not accept any sort of combined FITS file, we ran `srcflux` separately for the five different *Chandra* observations on the different regions and averaged the flux results. The averaged confidence intervals were calculated using propagation of errors.[23] The calculated flux values for the "Model Flux" (which takes absorption into account) are given in Table 10.

[23]In the propagation of errors, if n values with errors ϵ_1, ϵ_2, etc. are averaged, the resulting error becomes:

$$\delta\epsilon_{\text{avg}} = \sqrt{(\delta\epsilon_1)^2 + (\delta\epsilon_2)^2 + \ldots + (\delta\epsilon_n)^2}$$

3.4. *X-Ray Fluxes*

As discussed in Section 3.3.3, `srcflux` is useful in situations where there are very few counts. However, upon comparing the calculated fluxes for the `srcflux` and Sherpa methods (Sections 3.3.3 and 3.3.2), we found that the `srcflux` values were generally much lower than the Sherpa values and had very large error bars, particularly for the low count regions. The reason for this is that since `srcflux` analyzed each OBSID dataset separately, in cases of very low counts (e.g. the elliptical source B region) there are often one or two counts per observation, and so the calculated flux values are dramatically affected by the energies of the individual photons (which can be evaluated using CIAO's `eff2evt` function). With this knowledge, we will exclude all of the `srcflux` values from the final X-ray fluxes for all regions.

Table 10: `srcflux` analysis fluxes

Region name	Model Flux (erg/cm^2/s)[a]	68% Conf. Interval
Core	5.224e-16	(nan, 1.021e-15)
Einstein ring (thick)	1.374e-15	(1.206e-15, 1.604e-15)
Einstein ring (thin)	9.988e-16	(1.0136e-15, 1.407e-15)
Galaxy (no core)	5.968e-16	(6.998e-16, 1.103e-15)
Galaxy (with core)	8.856e-16	(8.623e-16, 1.253e-15)
NW lobe	2.800e-15	(1.766e-15, 2.136e-15)
SE lobe	1.856e-15	(1.384e-15, 1.756e-15)
Source B	2.592e-16	(nan, 9.099e-16)
Core (1″ circle)	8.036e-16	(8.214e-16, 1.210e-15)
Source B (1″ circle)	3.758e-16	(5.729e-16, 9.842e-16)

[a]Fluxes calculated assuming a power-law spectral form with $\Gamma = 1.9$ and the galactic N_H towards 3C 220.3 of 3.26×10^{20} atoms/cm^2 (calculated using Colden[22])

Instead, since the Sherpa values for the different regions are fairly close to each other, we average the flux values for the different binnings in the energy range of 0.5 keV to 8 keV (avoiding the larger uncertainties at lower energies). Table 11 shows a summary of the averaged X-ray fluxes. The corresponding luminosities (which are also given in Table 11) all have values on the order of 10^{42} erg s^{-1}. For an AGN core, the values for both the AGN core of 3C 220.3 and source B (if it does have an AGN core) are on the lower side of the typical range of $10^{42} - 10^{46}$ erg s^{-1} (Gandhi 2005).

3.5. *Optical Analysis and Fluxes*

Unlike with X-rays, finding the fluxes for the *HST* observations of the 3C 220.3 system is much simpler. In order to perform flux ratio comparisons to determine the dominant radiative processes (described in Chapter 4), we used the same regions that were defined in the X-ray analysis (Section 3.1). However, due to several bright optical sources near 3C

Table 11: Averaged Sherpa analysis fluxes and luminosities

Region	Avg. flux (erg/cm^2/s)[a]	68% Conf. Interval	Luminosity (erg/s)
Core	2.469e-15	(0.000e+00, 4.420e-15)	5.183e+42
Einstein ring (thick)	1.537e-15	(2.915e-16, 2.725e-15)	3.226e+42
Einstein ring (thin)	1.261e-15	(4.266e-16, 2.008e-15)	2.648e+42
Galaxy (no core)	1.593e-15	(4.001e-16, 2.588e-15)	3.345e+42
Galaxy (w core)	1.391e-15	(6.310e-16, 1.944e-15)	2.920e+42
NW lobe	2.060e-15	(1.164e-15, 3.187e-15)	4.324e+42
SE lobe	1.743e-15	(9.610e-16, 2.545e-15)	3.658e+42
Source B	7.878e-16	(9.706e-17, 1.891e-15)	1.654e+42
Core (1″circle)	1.192e-15	(5.255e-16, 1.824e-15)	2.501e+42
Source B (1″circle)	6.200e-16	(1.560e-16, 1.110e-15)	1.301e+42

[a]Fluxes calculated assuming a power-law spectral form with $\Gamma = 1.9$ and the galactic N_H towards 3C 220.3 of 3.26×10^{20} atoms/cm^2 (calculated using Colden[22])

220.3 that fall inside the large elliptical annulus used as the background region for the X-ray analysis, we defined a new background region comprised of nine circles with radii of 0.670″ each. Figure 19 compares these two background regions.

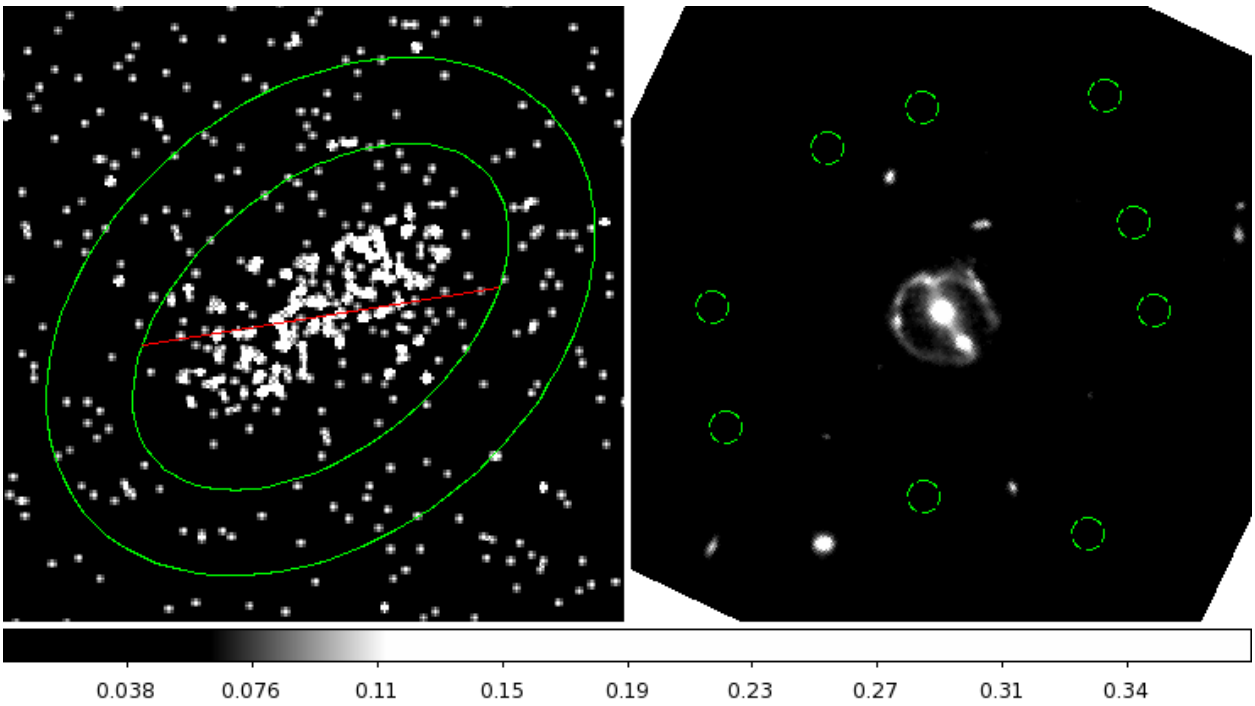

Figure 19: Left: X-ray analysis background region (green) overlaid on merged broadband *Chandra* data with eighth-size sub-pixel binning and Gaussian smoothing ($r = 2$, $\sigma = 1.5$). Right: Optical analysis background regions (dotted green) overlaid on *HST* F160W image.

Fluxes (in counts) were calculated using the Funtool `funcnts` ("Counts in Regions") in the CIAO version of DS9.[24] Using the counts of the source region (C_S), the background region(s) (C_B), and the areas of the source and background regions (A_S and A_B), `funcnts` evaluates the background-subtracted source counts (C_{BS}) with the following formula:

$$C_{BS} = C_S - C_B \cdot \frac{A_S}{A_B} \tag{10}$$

[24]See http://hea-www.harvard.edu/RD/funtools/programs.html#funcnts for more information about the CIAO/DS9 Funtools.

Table 12: *HST* Conversion factors

Filter	Conversion factor
F160W	0.1519 μJy·s/e$^-$
F606W	0.1364 μJy·s/e$^-$
F814W	0.3289 μJy·s/e$^-$

Necessary errors are calculated using propagation of error. Tables 13 through 15 list the counts, areas, and errors for the various regions for the three *HST* filter observations.

Since the raw *HST* data values have units of electrons per second,[25] we convert to flux using the filter-specific inverse sensitivity factor (`PHOTFNU`), which has units of Jansky-seconds per electron. The conversion factors for the three filters are listed in Table 12. The calculated fluxes for the various regions in the different filters are listed in Tables 13 through 15.

[25]These units are defined in the *HST* FITS file headers with the keyword `BUNIT` ("brightness units").

Table 13: *HST* F160W region counts and errors with background subtraction

Region	Counts[a]	Area [b]	Area ratio[c]	Net Counts[d]	Net error[e]
Background (HST)	-0.123	12.77			
Core	216.924	1.48	8.628	216.939	14.728
Einstein ring (thick)	362.945	10.61	1.204	363.047	19.049
Einstein ring (thin)	336.959	9.54	1.339	337.051	18.355
Galaxy (no core)	99.68	1.95	6.549	99.699	9.984
Galaxy (with core)	292.817	3.08	4.146	292.847	17.112
NW lobe	158.617	15.27	0.836	158.765	12.587
SE lobe	67.057	12.21	1.046	67.174	8.182
Source B	117.792	1.54	8.292	117.807	10.853
Core ($1''$ circle)	291.145	3.13	4.08	291.175	17.063
Source B ($1''$ circle)	176.546	3.14	4.067	176.576	13.287

[a]Counts are given in units of e^-/s.
[b]Areas are given in units of $arcsec^2$. For F160W observations, 1 arcsec = 0.1 pixels.
[c]Area ratio is defined as the ratio of the background area (in $arcsec^2$) to the region area (in $arcsec^2$).
[d]Net counts are given in units of e^-/s.
[e]Net errors are given in units of e^-/s.

Table 14: *HST* F814W Region counts and errors with background subtraction

Region	Counts[a]	Area [b]	Area ratio[c]	Net Counts[d]	Net error[e]
Background (HST)	5.38	12.68			
Core	23.271	1.52	8.342	22.624	4.832
Einstein ring (thick)	38.697	10.59	1.197	34.203	6.516
Einstein ring (thin)	36.057	9.56	1.326	31.999	6.254
Galaxy (no core)	13.472	1.92	6.604	12.657	3.687
Galaxy (with core)	33.173	3.05	4.157	31.881	5.786
NW lobe	26.506	15.27	0.83	20.027	5.857
SE lobe	9.358	12.21	1.038	4.175	3.788
Source B	11.472	1.54	8.234	10.82	1.54
Core (1″ circle)	33.368	3.14	4.038	32.034	5.805
Source B (1″ circle)	18.973	3.14	4.038	17.642	4.393

[a]Counts are given in units of e^-/s.
[b]Areas are given in units of $arcsec^2$. For F8140W observations, 1 arcsec = 0.0396197 pixels.
[c]Area ratio is defined as the ratio of the background area (in $arcsec^2$) to the region area (in $arcsec^2$).
[d]Net counts are given in units of e^-/s.
[e]Net errors are given in units of e^-/s.

Table 15: *HST* F606W Region counts and errors with background subtraction

Region	Counts[a]	Area [b]	Area ratio[c]	Net Counts[d]	Net error[e]
Background (HST)	5.634	12.71			
Core	15.724	1.53	8.307	15.048	3.976
Einstein ring (thick)	46.22	10.6	1.199	41.527	7.08
Einstein ring (thin)	43.418	9.56	1.329	39.186	6.826
Galaxy (no core)	11.109	1.92	6.62	10.258	3.352
Galaxy (with core)	23.974	3.06	4.154	22.621	4.929
NW lobe	29.659	15.26	0.833	22.903	6.145
SE lobe	14.348	12.22	1.04	8.937	4.421
Source B	7.624	1.54	8.253	6.944	2.776
Core ($1''$ circle)	23.982	3.14	4.048	22.592	4.932
Source B ($1''$ circle)	15.573	3.14	4.048	14.181	3.99

[a]Counts are given in units of e^-/s.
[b]Areas are given in units of arcsec^2. For F660W observations, 1 arcsec = 0.0396192 pixels.
[c]Area ratio is defined as the ratio of the background area (in arcsec^2) to the region area (in arcsec^2).
[d]Net counts are given in units of e^-/s.
[e]Net errors are given in units of e^-/s.

Table 16: Optical fluxes (in μJy) from *HST* Observations

Region	F160W	F814W	F606W
Background (HST)	0.011 ± 0.041	0.422 ± 0.373	0.144 ± 0.14
Core	32.948 ± 2.237	7.442 ± 1.589	2.053 ± 0.542
Einstein ring (thick)	55.138 ± 2.893	11.25 ± 2.143	5.666 ± 0.966
Einstein ring (thin)	51.19 ± 2.788	10.525 ± 2.057	5.346 ± 0.931
Galaxy (no core)	15.142 ± 1.516	4.163 ± 1.213	1.400 ± 0.457
Galaxy (with core)	44.476 ± 2.599	10.486 ± 1.903	3.086 ± 0.672
NW lobe	24.112 ± 1.912	6.587 ± 1.927	3.125 ± 0.838
SE lobe	10.202 ± 1.243	1.373 ± 1.246	1.219 ± 0.603
Source B	17.892 ± 1.648	3.559 ± 1.118	0.947 ± 0.379
Core ($1''$ circle)	44.222 ± 2.591	10.537 ± 1.909	3.082 ± 0.673
Source B ($1''$ circle)	26.818 ± 2.018	5.803 ± 1.445	1.935 ± 0.544

4. DISCUSSION

The main goal of this analysis of the 3C 220.3 system is to understand both its mass distribution (i.e. the masses of source A and source B) and its radiation processes. Using the X-ray and optical fluxes that were calculated in Chapter 3, we present four areas of analysis: an updated spectral energy distribution for the combined system (i.e. 3C 220.3, source B, and SMMJ0939) (Section 4.1), updated mass calculations of 3C 220.3 and source B using the broadband (optical and IR) fluxes (Section 4.2), magnetic field calculations of the radio lobes of 3C 220.3 (Section 4.4), and updated lens modeling using the newer *HST* and *Chandra* data (Section 4.3).

4.1. *Spectral Energy Distribution*

For unresolved or barely resolved galaxies, calculating star population masses and dust masses can be difficult. However, similar to the signatures that active galaxies leave in their emission across the electromagnetic spectrum, properties such as mass, age, metallicity, and star formation rates (SFRs) can also be inferred from the spectral energy distributions (SEDs) of galaxies (Walcher et al. 2011).

The updated SED for the 3C 220.3 system, which includes our flux measurements of the system for the 2014 *HST* data (in filters F606W, F814W, and F160W), was adapted from several sources. The original SED for the system was shown in Haas et al. (2014) and lists the fluxes for their *HST*, *Herschel*, Spitzer, Keck, and SMA data. A second SED was made by Leung & Riechers (2016) and includes the radio continuum measurements. Values from other papers have also been included. Tables 18 and 19 indicate the flux values used to construct the updated SED shown in Figure 20. With the X-ray fluxes included, it is easier to visualize the SED in terms of a ν vs. $\nu \cdot F_\nu$ plot, as show in Figure 21. For these SEDs (Figures 20 and 21), the full-system optical fluxes include 3C 220.3 (source A), source B, and the lensed SMG (Einstein ring). The full-system X-ray flux includes the NW and SE radio lobe regions as well. The X-ray fluxes for these components were derived from their average

flux densities through the Sherpa analysis (Section 3.3.2). The average flux densities for the X-ray components are given in Table 17.

The SED has several prominent features. First, the sharp bump in the IR/FIR region is unusually high for a radio galaxy and is what caught the attention of Haas et al. (2014) (see Section 1.6 and Chapter 2). This excess emission is due to the lensed SMG. Second, the rapid drop of the radio continuum at long wavelengths indicates that the radio core of 3C 220.3 is very faint (agreeing with observations). Since the primary radiation process in radio lobes is typically synchrotron radiation, the radio continuum represents the non-thermal emission of the system.

Using the broadband (i.e. optical and IR) fluxes of the updated SED, we performed blackbody fits to determine a rough estimate of the temperature of the dominant components for a given wavelength (Figure 22). The resulting observed temperatures for 3C 220.3 (source A), source B, and the SMG are $T_{A,\mathrm{obs}} \sim 2630$ K, $T_{B,\mathrm{obs}} \sim 2570$ K, and $T_{\mathrm{SMG,obs}} \sim 2660$ K. Correcting for the redshifts of the source (and assuming the redshift of source B is the same as 3C 220.3), the restframe temperatures become $T_{A,\mathrm{rest}} \sim 4430$ K, $T_{B,\mathrm{rest}} \sim 4340$ K, and $T_{\mathrm{SMG,rest}} \sim 8570$ K. For sources A and B, these temperatures roughly correspond to the temperatures of the starlight (i.e. infrared). Since the SMG is at a much higher redshift, its restframe temperature corresponds to the restframe UV emission that may be attributed to the beginnings of an unobscured quasar phase (Section 4.3).

Table 17: Average X-ray flux densities by component

Region	Flux density (erg/cm^2/s/keV)
Core	7.273e-16
Einstein ring (thick)	4.67e-16
NW lobe	6.52e-16
SE lobe	5.46e-16
Source B	1.63e-16

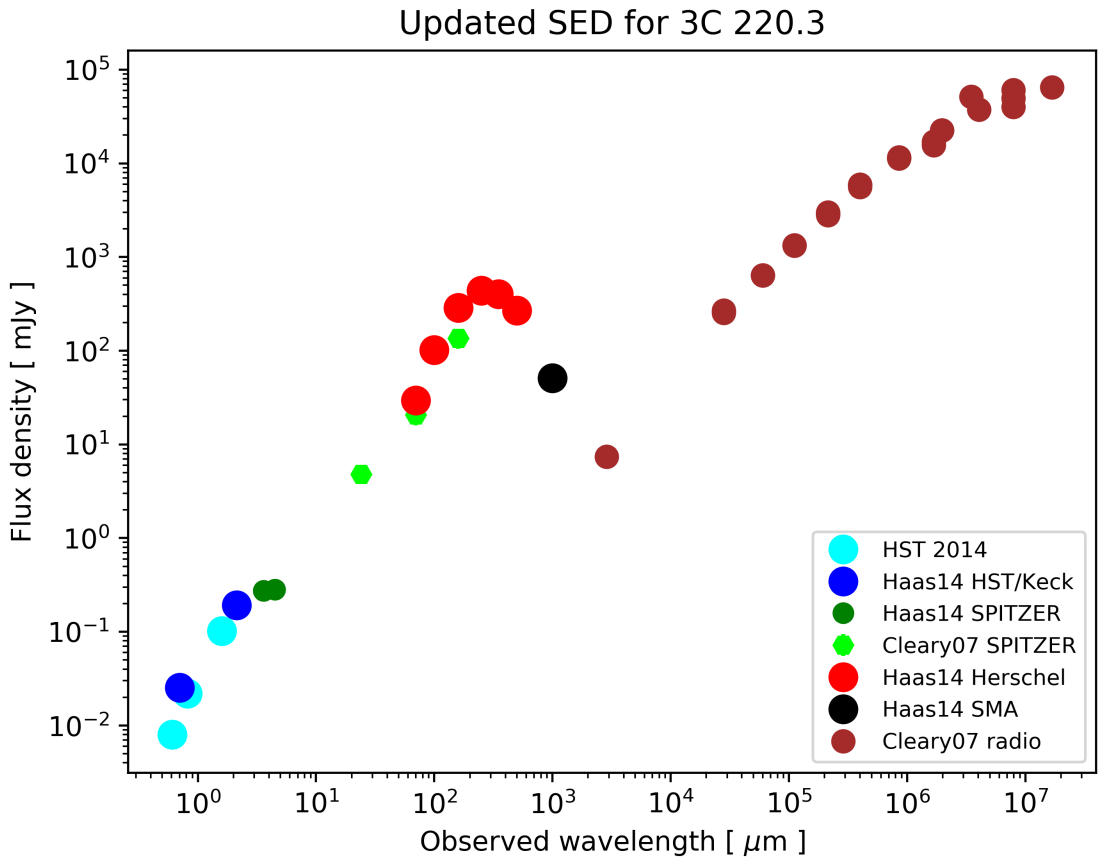

Figure 20: Updated SED of the entire 3C 220.3 system (i.e. sum of fluxes from 3C 220.3, source B, and SMMJ0939). Cyan dots indicate our new *HST* flux measurements (F606W, F814W, F160W) while blue dots indicate the *HST* F702W and Keck 2.124 μm fluxes (Haas et al. 2014). Dark green circles indicate the Spitzer 3.6 μm and 4.5 μm fluxes determined by Haas et al. (2014), while light green hexagons indicate the fluxes listed in Cleary et al. (2007). The red and black dots show the *Herschel* and SMA fluxes determined by Haas et al. (2014). The brown dots at long wavelengths are fluxes taken from various surveys as listed in Leung & Riechers (2016) and indicate the radio continuum emission. The errorbars for the measurements are small compared to the size of the markers used and are not visible.

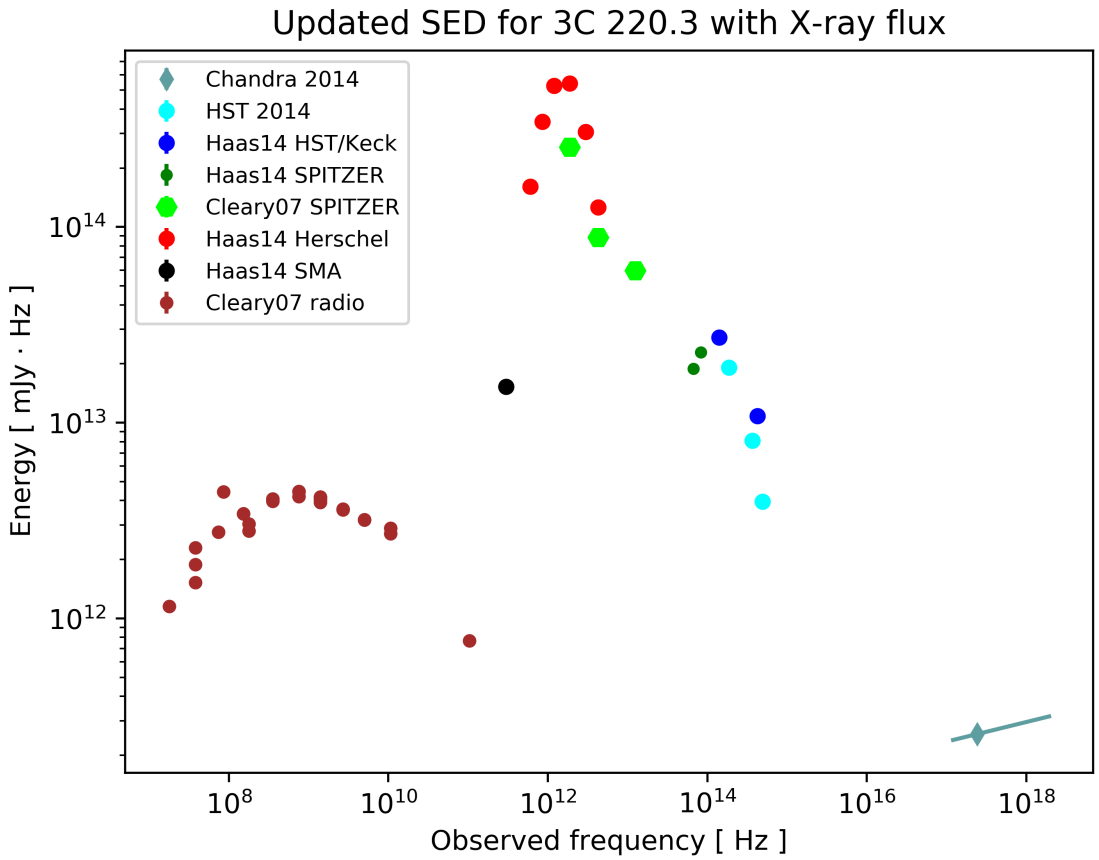

Figure 21: Updated SED of the entire 3C 220.3 system (i.e. sum of fluxes from 3C 220.3, source B, and SMMJ0939), shown as a ν vs. $\nu \cdot F_\nu$ plot. Cyan dots indicate our new *HST* fluxes (F606W, F814W, F160W) while blue dots indicate the *HST* F702W and Keck 2.124 μm fluxes (Haas et al. 2014). Dark green circles indicate the Spitzer 3.6 μm and 4.5 μm fluxes determined by Haas et al. (2014), while light green hexagons indicate the fluxes listed in Cleary et al. (2007). The red and black dots show the *Herschel* and SMA fluxes determined by Haas et al. (2014). The brown dots at high frequencies are fluxes taken from various surveys as listed in Leung & Riechers (2016) and indicate the radio continuum emission. The gray-blue point at the highest frequency corresponds to the *Chandra* X-ray flux at an energy of 1 keV and a power law with spectral index of $\alpha = -0.9$ ($\Gamma = 1.9$). The line intersecting the X-ray flux point shows the corresponding power law ($\alpha = -0.9$) extending from 0.5 keV to 8 keV (the energy range used for our flux analysis). The errorbars for the measurements are small compared to the size of the markers used and are not visible.

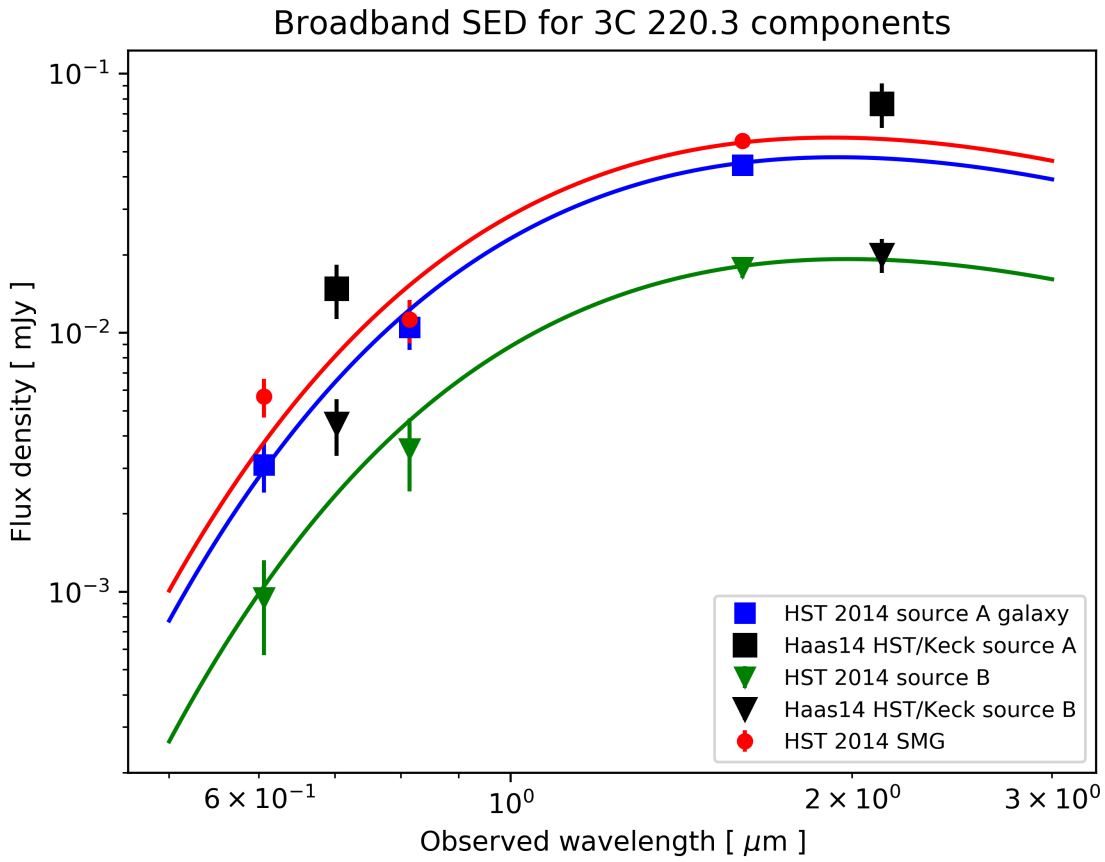

Figure 22: Broadband SED of the 3C 220.3 (blue), source B (green), and SMG (red) components of the 3C 220.3 system. The *HST* F702W and Keck fluxes from Haas et al. (2014) are marked in black. The blackbody fits for the three sources are given in corresponding colors and have temperatures of $T_{A,\mathrm{obs}} \sim 2630$ K, $T_{B,\mathrm{obs}} \sim 2570$ K, and $T_{\mathrm{SMG,obs}} \sim 2660$ K. The approximate restframe temperatures ($T_{\mathrm{rest}} = (1+z)T_{\mathrm{obs}}$) of the three components are as follows: $T_{A,\mathrm{rest}} \sim 4430$ K, $T_{B,\mathrm{rest}} \sim 4340$ K, and $T_{\mathrm{SMG,rest}} \sim 8570$ K.

Table 18: SED values for total fluxes of entire 3C 220.3 system[a]

Wavelength (μm)	Flux Density (mJy)	Instrument	Reference[b]
0.0012	5.65×10^{-7}	Chandra/ACIS-S	NEW
0.606	0.008 ± 0.001	HST/WFC3	NEW
0.702	0.0253 ± 0.00	HST/WFPC2	1
0.814	0.022 ± 0.003	HST/WFC3	NEW
1.6	0.102 ± 0.004	HST/WFC3	NEW
2.124	0.193 ± 0.03	Keck/NIRC2	1
3.6	0.275 ± 0.028	Spitzer/IRAC	1
4.5	0.283 ± 0.028	Spitzer/IRAC	1
24	4.8 ± 0.5	Spitzer/MIPS	3
70	29.5 ± 5	Herschel/PACS	1,2
70	20.7 ± 4.8	Spitzer/MIPS	3
70	26 ± 3	Herschel/PACS	4
100	102 ± 7	Herschel/PACS	1,2
100	99 ± 4	Herschel/PACS	4
160	289 ± 9	Herschel/PACS	1,2
160	136.3 ± 31.1	Spitzer/MIPS	3
160	259 ± 11	Herschel/PACS	4
250	440 ± 15	Herschel/SPIRE	1,2
250	452 ± 9	Herschel/SPIRE	4
350	403 ± 20	Herschel/SPIRE	1,2
350	412 ± 8	Herschel/SPIRE	4
500	268 ± 30	Herschel/SPIRE	1,2
500	259 ± 7	Herschel/SPIRE	4
1000	51 ± 12	SMA	1,2

[a]This is defined as the sum of the fluxes for 3C 220.3, source B, and SMMJ0939.

[b]Reference labels: 1 = Haas et al. (2014), 2 = Leung & Riechers (2016), 3 = Cleary et al. (2007), 4 = Westhues et al. (2016)

Table 19: SED values for radio continuum (includes both lobes and core, if resolved)[a]

Frequency	Wavelength	Flux Density (mJy)
17.8 MHz	16.8 m	64900.0 ± 6490.0
37.8 MHz	7.93 m	60700.0 ± 6070.0
38 MHz	7.89 m	40200.0 ± 6300.0
38 MHz	7.89 m	49600.0 ± 4960.0
73.8 MHz	4.06 m	37500.0 ± 3820.0
86 MHz	3.49 m	51600.0 ± 9900.0
152 MHz	1.97 m	22500.0 ± 40.0
152 MHz	1.97 m	22600.0 ± 80.0
178 MHz	1.68 m	17100.0 ± 1710.0
178 MHz	1.68 m	15700.0 ± 2350.0
352 MHz	85.1 cm	11600.0 ± 464.0
352 MHz	85.1 cm	11300.0 ± 453.0
750 MHz	40.0 cm	5600.0 ± 840.0
750 MHz	40.0 cm	5940.0 ± 210.0
750 MHz	40.0 cm	5940.0 ± 280.0
1.4 GHz	21.4 cm	2890.0 ± 90.0
1.4 GHz	21.4 cm	2800.0 ± 140.0
1.4 GHz	21.4 cm	2990.0 ± 60.0
1.4 GHz	21.4 cm	2950.0 ± 90.0
2.7 GHz	11.1 cm	1340.0 ± 100.0
2.7 GHz	11.1 cm	1330.0 ± 70.0
5.0 GHz	6.00 cm	636.0 ± 50.0
5.0 GHz	6.00 cm	640.0 ± 100.0
10.7 GHz	2.80 cm	253.0 ± 28.0
10.7 GHz	2.80 cm	270.0 ± 30.0
104.2 GHz	2.88 mm	7.39 ± 1.42

[a]Adapted from Leung & Riechers (2016); references for flux values listed in Leung & Riechers (2016)

4.2. *Stellar Mass Determinations from Broadband Fluxes*

SED modeling typically focuses on the emission from stellar populations and the interstellar medium (ISM) of a galaxy. Since both sources typically have the strongest emission in the UV to FIR range, codes that fit SED models usually focus only on the UV-FIR section of the SED. At their simplest, SED models sum together the emissions from stellar populations of different ages, types, and compositions. While the most basic model, the single-stellar population (SSP) model, assumes a stellar population of a single age and composition, more robust models incorporate a variety of stellar populations. Initial parameters for an SED model will include a library of stellar populations, initial mass function (IMF), star formation history (SFH), and dust extinction law. For a detailed review on SED modeling, see Walcher et al. (2011).

For our SED modeling, we used the publicly-available FAST (Kriek et al. 2009) code to calculate the stellar and dust masses of 3C 220.3, source B, and the lensed SMG. FAST has three main input files: a photometry catalog which defines the fluxes for a number of sources in various filters, a redshift catalog that defines the previously-determined redshifts of the sources, and a parameter file. There is a library of the available filters for FAST simulations that has information about the peak wavelength and spectral response of a variety of broadband filters for different telescopes. In the parameter file, the user chooses from the following:

- Stellar population library (Bruzual & Charlot 2003; Maraston 2005; Conroy et al. 2009)
- Stellar IMF (Chabrier 2003; Salpeter 1955; Kroupa 2002)
- SFH (exponential decline; delayed exponential decline; truncated)[26]

[26]The star formation history describes the star formation rate (SFR) over time. For exponential decline, the SFR decreases exponentially from the beginning of the model. In delayed exponential decline, the SFR remains constant for some time before undergoing exponential decline. With a truncated SFH, the SFR stops altogether after a certain time.

- Dust attenuation law (Calzetti et al. 2000; Cardelli et al. 1989; Kriek & Conroy 2013; Noll et al. 2009)

To fit the model, FAST creates a cube of the input filter fluxes and the stellar population model and minimizes the χ^2 value for each point on the cube. Specified confidence intervals are calculated through Monte Carlo simulations (Kriek et al. 2009).

Since the FAST filter library only has entries for the *HST* filters, our simulations are based off the *HST* observations only. Although the true redshift of source B is unknown, the lens modeling presented in Haas et al. (2014) indicates that source B is likely close to the redshift of 3C 220.3 ($z = 0.685$) and so we approximate the redshift of source B as $z = 0.685$.

As is visible in Figure 22, the F702W fluxes from Haas et al. (2014) appear to be somewhat higher than the F606W and F814W fluxes. Several attempts have been made to understand this discrepancy, but for the purpose of the mass determinations discussed here, we exclude the F702W fluxes. Using the FAST default settings of a delayed exponential SFH model, Charbrier stellar IMF, and Kriek & Conroy (2013) dust law, we find the stellar mass of 3C 220.3 (source A) to be $M_A^* \sim \left(1.1^{+17}_{-0.17}\right) \times 10^{10} M_\odot$ and the stellar mass of source B to be $M_B^* \sim \left(5.4^{+90}_{-1.1}\right) \times 10^9 M_\odot$.[27] Although these are considerably lower than the stellar mass values of $M_A^* \sim 2.2 \times 10^{11} M_\odot$ and $M_B^* \sim 5.5 \times 10^{10} M_\odot$ as calculated by Haas et al. (2014), the difference is reasonable since the higher F702W fluxes suggest more starlight. For comparison, if the F702W fluxes are included in the FAST calculations, the resulting stellar masses are $M_A^* \sim \left(1.3^{+0.45}_{-1.2}\right) \times 10^{11} M_\odot$ and $M_B^* \sim \left(6.8^{+1.0}_{-6.3}\right) \times 10^{10} M_\odot$, which are consistent with the stellar masses calculated by Haas et al. (2014). However, as Haas et al. (2014) discuss in Section 5 of their paper, their masses should be treated as upper limits and so the masses without the F702W filter are fully consistent with Haas et al. (2014). Since we have three-color *HST* data (compared to the one filter used by Haas et al. (2014)), we expect the

[27] The errors given for the FAST stellar masses are 1σ uncertainties.

true masses of sources A and B to be closer to the masses we calculated. Figure 23 shows the simulated FAST spectra with the real fluxes of source A and B overplotted.

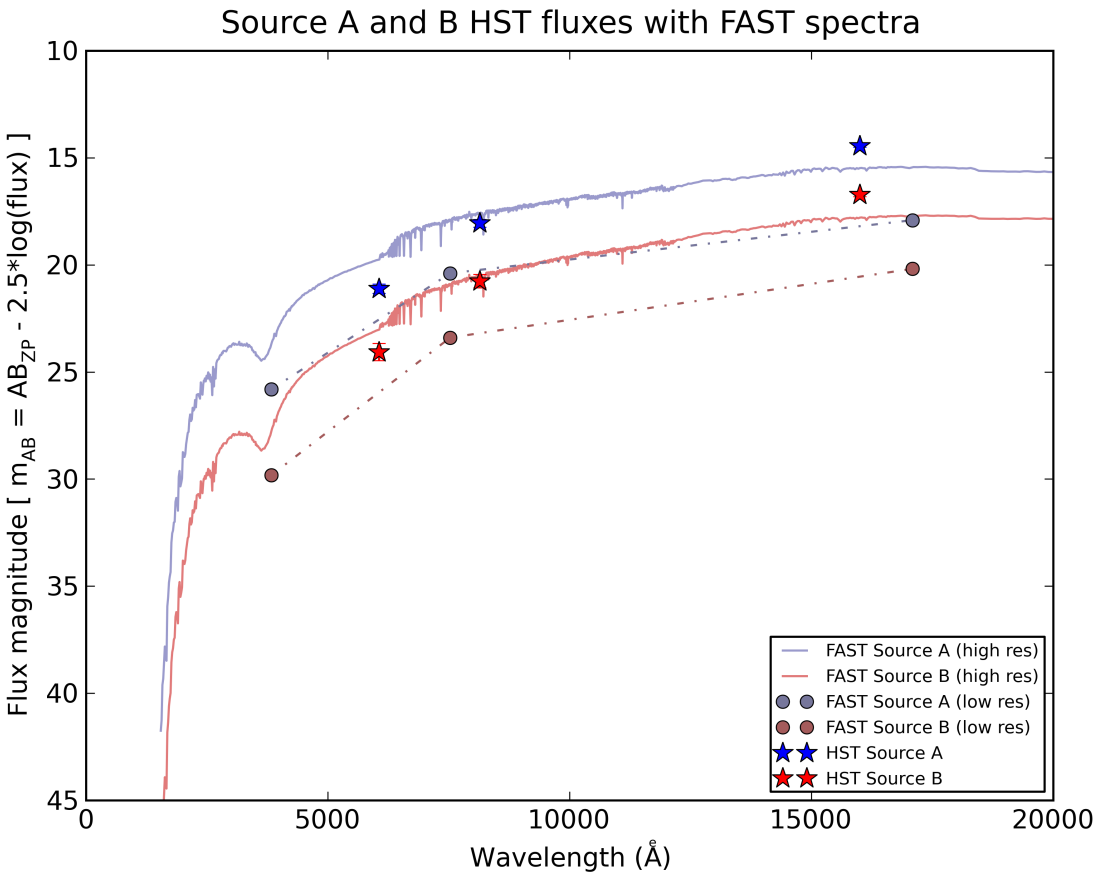

Figure 23: Broadband SED of source A (blue) and source B (red) fluxes for *HST* F606W, F814W, and F160W bands (indicated by stars). The simulated FAST spectra are shown in corresponding colors, with the dots indicating the coarser, low resolution spectra and the solid lines representing the finer, high resolution spectra.

4.3. *Lens Modeling*

As discussed in Section 1.5, the image in a lensing system depends on the mass distribution of both the source and the lens. However, since there are many free parameters in lensing systems, reconstructing the source can be very difficult and computationally taxing.

The updated lens modeling for the *HST* and *Chandra* data is being carried out by our collaborator, Simona Vegetti, who did the original modeling of the 3C 220.3 system in Haas et al. (2014) and has extensive experience in modeling strongly lensed systems (Vegetti & Koopmans 2009; Rizzo et al. 2018). In essence, the code inputs are a surface brightness map (i.e. flux map) of a source in each waveband, a corresponding PSF, and a root mean square (RMS)/error map or an average background error value.

Since the *HST* data were already exposure corrected (in units of electrons/s), we simply cropped the drizzled images to include less background and extracted a PSF of a point-like source in the field for each filter (Figure 24). However, in the drizzling process during the original data reduction, the information on the errors were lost, and so the background error value will be determined from the average RMS for each filter (as was done in the Haas et al. (2014) modeling).

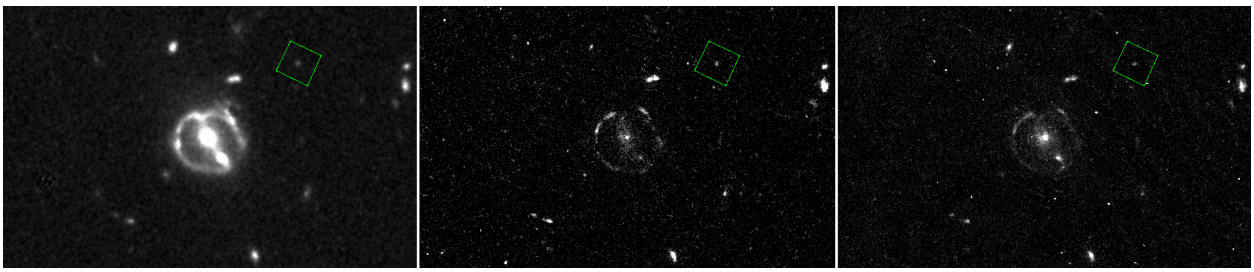

Figure 24: Left to right: *HST* F160W, F606W, and F814W exposures. The PSF extraction region is indicated by the green box.

For the *Chandra* data, we needed to produce an exposure-corrected dataset (i.e. a flux map). To do so, we used the CIAO function `make_instmap_weights` to render a spectral weights map (using the absorption-corrected power law model discussed in Section 3.3 and

using an energy range of 0.5-8 keV). We then used this weights map to generate an exposure map for each of the five observations using the CIAO `fluximage` function (Figure 25). After merging the exposure maps via the `reproject_image` function, we divided the merged dataset by the merged exposure map to produce a flux map and cropped it to the 3C 220.3 system. Even with the merged data, the X-ray background is very low and we were unable to produce an RMS error map of the observations. Instead, we use the error of the counts for the X-ray background region (Table 7), which has an RMS error of 10% of the background.

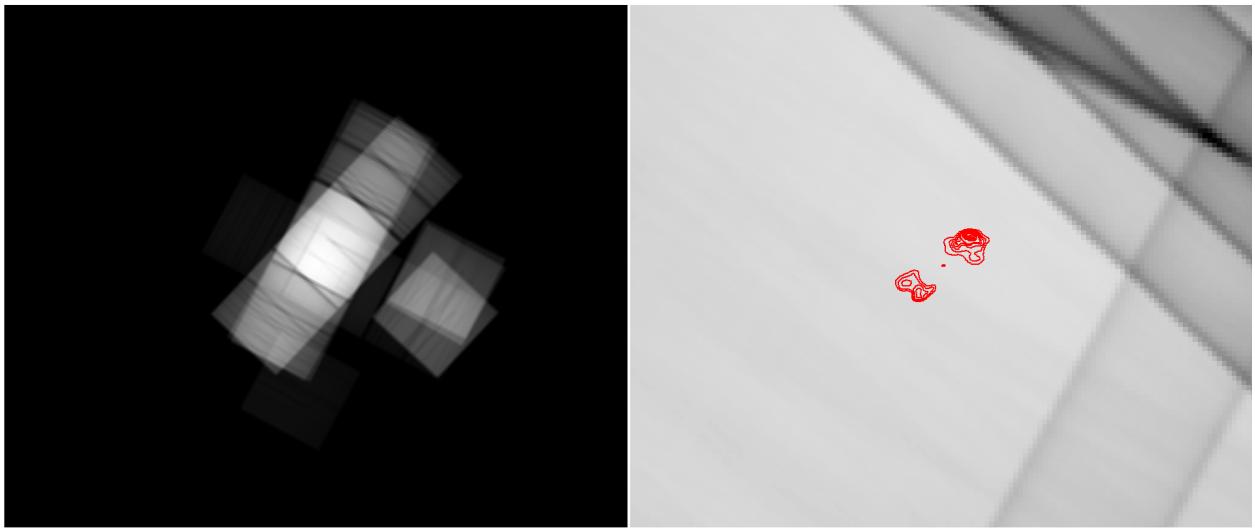

Figure 25: Left: Merged exposure map of the five *Chandra* observations. Right: Zoomed-in view of the merged *Chandra* exposure map. The red contours are the JVLA radio data.

The lensing code developed by Rizzo et al. (2018) (used in this analysis) is a 3D extension of the Bayesian code developed by Vegetti & Koopmans (2009). In both cases, the code uses two main sparse-matrix[28] operators: a blurring operator (derived from the PSF file) and a lensing operator (which contains the lens parameters $\eta_{\rm lens}$ and the lens potential $\psi(\eta_{\rm lens})$). The lensing operator maps points from the source plane, which is constructed to be a triangular grid using Delaunay triangulations, to the image plane, where the data

[28]Sparse matrices are matrices in which most of the elements are zeros.

lies. In order to simultaneously model both the lens potential and the surface brightness distribution of the source, the code assumes that correlated features in the image correspond to features of the source, while uncorrelated features correspond to perturbations in the lens potential. The optimization is done through an iterative process that finds the best-fit parameters by taking into account the smoothness of the source and the perturbations from the lensing potential, minimizing the defined penalty function, and, finally, comparing the Bayesian evidence values of the smooth and perturbed models. Detailed descriptions of these procedures are given in Vegetti & Koopmans (2009) and Rizzo et al. (2018).

For their lens modeling of the 3C 220.3 system, Haas et al. (2014) used the Keck data to find the optimized parameters for the lens model, since the Keck data had the highest signal-to-noise ratio and exhibited the most structure of the optical, infrared, or submillimeter data available at the time. The resulting lens model from this analysis was then used for modeling the *HST* F702W and SMA data. Figure 26 shows the reconstructed image of the lensed SMG from Haas et al. (2014).

Through this lens model, Haas et al. (2014) also determined the total (baryonic + dark matter) masses of sources A and B to be $M_A \sim 3.5 \times 10^{11} M_\odot$ and $M_B \sim 1.2 \times 10^{11} M_\odot$. Comparing these masses to the stellar masses they calculated, they found the dark matter fractions ($f_{\rm DM}$) to be $\sim 40\%$ and $\sim 55\%$, respectively. Using the stellar masses calculated with our FAST SED fitting (Section 4.2) and the total masses calculated in Haas et al. (2014), we determined our dark matter fractions to be $f_A \sim 0.97^{+0.01}_{-0.48}$ and $f_B \sim 0.96^{+0.01}_{-0.75}$. This is considerably higher than the values calculated by Haas et al. (2014) and the typical range of dark matter fractions for galaxies of similar masses and redshifts ($0.25 < f_{\rm DM} < 0.75$) (Haas et al. 2014, Section 5). Based on the lower fluxes from the new *HST* data, however, the total masses of sources A and B are likely to change with the updated lens modeling.

Haas et al. (2014) also calculated the de-magnified FIR luminosity of the SMG to be $\sim 1 \times 10^{13} L_\odot$, based off the total magnification factor of the lensing ($\mu \sim 10$). While the rest-frame UV fluxes from the *HST* data are lower than those used in the original lens

modeling, the overall luminosity for the SMG will probably not change significantly since the FIR peak dominates the SED (Figures 20 and 21).

Updated lens models with the more recent *Chandra* and three-color *HST* data (in addition to the older Keck, *HST* F702W, and SMA data) are forthcoming. Besides reconstructing an image of the SMG, the modeling will also determine the total galaxy masses for 3C 220.3 and source B, which will then be compared to the stellar masses determined in Section 4.2 to estimate the dark matter content of the lensing sources.

The addition of the new *HST* and *Chandra* data to the lens modeling raises some questions about what the updated SMG reconstruction might look like. Since a full Einstein ring is now visible, it is possible it will show restframe UV emission spread around the entire SMG instead of being concentrated only in the northern region.

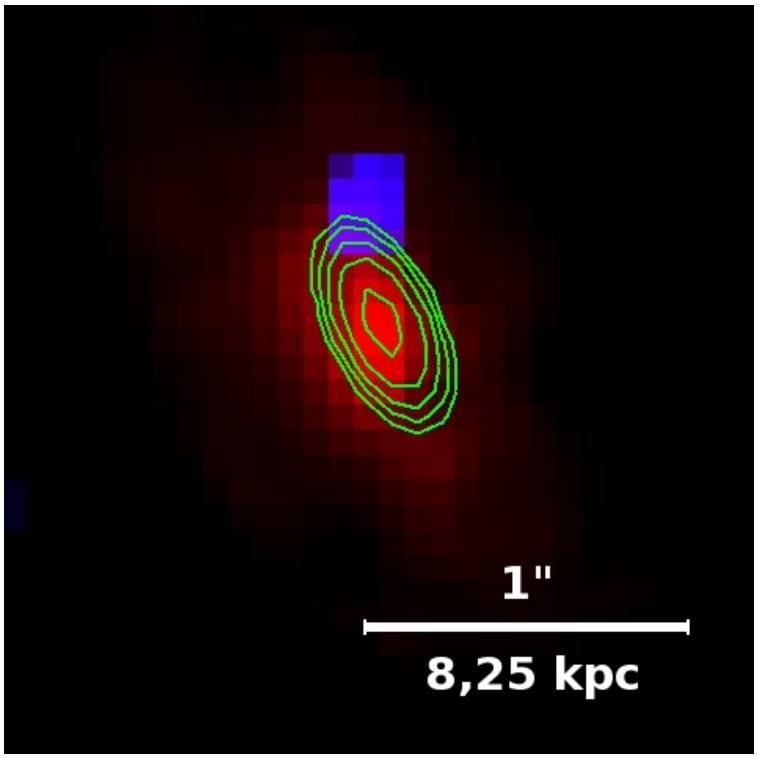

Figure 26: Reconstructed image of SMMJ0939 from Haas et al. (2014) with the following dataset: Keck (red), *HST* F702W (blue), and SMA (green contours). North is up and east is to the left. The blue region (from the *HST* data) in the northern part of the image is thought to indicate the beginning of an unobscured quasar AGN in SMMJ0939. Since the SMG lies at a redshift of $z = 2.221$, the restframe wavelength of the *HST* F702W data is about 218 nm.

4.4. *Flux Ratios and Magnetic Field Strengths*

Another important analysis of the 3C 220.3 system is to understand what radiation processes dominate in various areas of the system. Here, we consider the radiation in the radio lobes of 3C 220.3 by considering radio and X-ray fluxes that correspond to synchrotron radiation and the inverse-Compton scattering processes, respectively.

Before high-accuracy X-ray astronomy, there was no way to measure the magnetic fields of radio lobes directly. Until then, magnetic field estimations assumed that the energy of the system was at a minimum, with the energy in the magnetic field equal to that in the particles (i.e. relativistic electrons and relativistic but non-radiating particles like protons). This is known as the equipartition or minimum energy field ($B_{\rm me}$), and can be estimated using by using the synchrotron emission from a radio lobe. Synchrotron radiation occurs when charged particles are accelerated by a magnetic field (via a force of $\vec{v}\times\vec{B}$) to relativistic speeds and radiate energy (Rybicki & Lightman 1979). Although the electrons in a magnetic field emit a spectrum of frequencies, the power emitted by a synchrotron electron with energy E_e is given in Equation 1 of Govoni & Feretti (2004) as

$$-\frac{dE_e}{dt} = c_2(B_{\rm int}\sin\theta)^2 E_e^2 \tag{11}$$

where m_e is the electron mass, $B_{\rm int}$ is the internal magnetic field of the radio lobe, θ is the angle between the electron's movement and the magnetic field, and the coefficient c_2 is defined as $c_2 = (2e^4)/(3m_e^4c^7)$. The electron energy is defined as $E = \gamma m_e c^2$, where γ is the Lorentz factor and is given in Worrall & Birkinshaw (2006) as $\gamma = E_e/(m_e c^2)$. The "critical frequency" (the emission frequency at which the power spectrum peaks), as defined by Govoni & Feretti (2004) (Equation 2) is:

$$\nu_c = c_1(B\sin\theta)E_e^2 \tag{12}$$

where the coefficient c_1 is defined to be $c_1 = (3e)/(4\pi m_e^3 c^5)$. In SI units, Equation 12 can be written as:

$$\nu_c \approx 16.1\times10^{11}(B_{\rm int}\sin\theta)E_e^2 \tag{13}$$

where ν_c is in MHz, $B_{\rm int}$ is in nanoteslas, and E_e is in GeV. Although the peak frequency for synchrotron emission can fall at a range of energies, for AGN, it falls primarily in the radio regime. A basic method of determining the equipartition field is given in Section 3.2 of Govoni & Feretti (2004).

With X-ray data, however, we can make more direct calculations of the dynamics in the radio lobes. By comparing the relative strength of the synchrotron radiation emitted at radio frequencies to the X-ray emission, which is generated by inverse-Compton scattering from the same electron population, it is possible to determine the internal magnetic field ($B_{\rm int}$) of a lobe. Unlike synchrotron radiation, which involves the electrons in the radio lobes, inverse-Compton scattering occurs when a photon scatters off an electron, often gaining significant energy as a result. In the radio lobes, this process typically occurs between a cosmic microwave background (CMB) photon ($T \sim 2.7$ K) that is scattered to higher energies (i.e. X-ray energies) by a relativistic electron in the lobes. As described in Section 3.3 of Govoni & Feretti (2004), this inverse Compton-CMB (iC-CMB) up-scattering is described as:

$$\nu_x = \frac{4}{3}\gamma^2 \nu_{\rm CMB} \tag{14}$$

where $\nu_{\rm CMB}$ is the frequency of a CMB photon (before iC-CMB scattering), γ is the Lorentz factor of the relativistic electron, and ν_x is the X-ray frequency of the photon after scattering. Equation 14 can then be rewritten as:

$$\frac{E_x}{h} = \frac{4}{3}\left(\frac{E_e}{m_e c^2}\right)^2 \nu_{\rm CMB} \tag{15}$$

which simplifies to:

$$E_e = \sqrt{\frac{3 m_e^2 c^4}{4 h \nu_{\rm CMB}}}\sqrt{E_x} \tag{16}$$

Derivations of the internal magnetic field from X-ray and radio fluxes are given in Gursky & Schwartz (1977), Govoni & Feretti (2004), Worrall & Birkinshaw (2006), and Worrall (2009), among others.

Although the magnetic fields of radio lobes are often found not to be at minimum energy (Worrall 2009), it is still typical to calculate both internal and equipartition fields. In this thesis, we used three different methods – with increasing sophistication and differing assumptions – of calculating the minimum energy and internal magnetic fields to understand the underlying physics. We begin with the simple case of a single electron that up-scatters a CMB photon to X-ray energies (Method 1a) and then progress to more complex formulations that take into account the redshift, angular size, etc. and integrate over a spectrum of electron energies (Methods 2 and 3).

4.4.1. *Method 1a: Gursky & Schwartz (1977)*

Typically, the ratio between the X-ray and radio fluxes relates to the internal magnetic field of an AGN, while the equipartition field is calculated from the synchrotron radiation only. Gursky & Schwartz (1977) describe a method for approximating the internal magnetic field ($B_{\rm int}$). To do this, they calculate the frequency of the synchrotron emission to the X-ray energy through the electron energy by the following formulae:

$$E_e = 0.558\sqrt{E_x} \tag{17}$$

$$\nu_r = 16.1 \times 10^{11} B_{\rm int} E_e^2 \tag{18}$$

where E_e is the energy in GeV of an electron in a magnetic field $B_{\rm int}$ in nanoteslas, ν_r is the frequency in MHz of synchrotron radiation from an electron at E_e, and E_x is the X-ray energy in keV. Note that Equation 17 derives from a numerical approximation of Equation 16 and Equation 18 is an approximation of Equation 13 when the motion of the electron and the magnetic field are perpendicular ($\theta = 90°$). Although these two equations are approximations for the actual emission spectrum of a synchrotron electron, Gursky & Schwartz (1977) note that they are adequate in the case of the power law spectrum of the electrons (i.e. $dN/dE = KE^{-(2\alpha+1)}$). The ratio of the power of the inverse-Compton

emission (P_c) to the synchrotron emission (P_s) is then given as:[29]

$$R = \frac{P_c}{P_s} = \frac{aT^4}{B_{\rm int}^2/2\mu_0} \tag{19}$$

where a is the radiation density constant (7.5659×10^{-15}erg cm^{-3} K^{-4}), T is the temperature of the CMB photons (2.7 K), μ_0 is the permeability of free space ($4\pi \times 10^{-7}$ H/m), and $B_{\rm int}$ is the magnetic field in teslas.

We can convert the X-ray to radio power ratio (described by Gursky & Schwartz (1977) as the ratio of the energy densities in the magnetic and particle fields) to a flux ratio by:

$$\frac{P_c}{P_s} = \frac{F_x[\text{erg cm}^{-2}\text{ s}^{-1}\text{ keV}^{-1}] \cdot E_x[\text{keV}] \cdot A[\text{cm}^2]}{F_r[\text{erg cm}^{-2}\text{ s}^{-1}\text{ Hz}^{-1}] \cdot \nu_r[\text{Hz}] \cdot A[\text{cm}^2]} = \frac{F_x \cdot E_x}{F_r \cdot \nu_r} \tag{20}$$

where A is the area of the source in cm^2, F_x is the X-ray flux density, and F_r is the radio flux density. Since we only have measurements at specific radio frequencies (Table 19), we estimated the radio flux density for a given frequency by least-square fitting the power law $F_\nu \propto C \cdot \nu^\alpha$ to the continuum data. Doing so provides a best-fit spectral index of $\alpha = -0.9$ (in good agreement with the value used for our X-ray flux calculations in Section 3.4).

Since the synchrotron and inverse-Compton emission originate from the same system of relativistic electrons in the radio lobes, they have the same spectral index, and so this best-fit spectral index is in good agreement with the value used for our X-ray flux calculations (Section 3.4). The agreement of this best-fit radio spectral index with the power law slope used for the X-ray analysis in Section 3.3 indicate that the typical spectral index assumption of $\alpha = -0.9$ ($\Gamma = 1.9$) is a good approximation.

For the X-ray flux density, we averaged the X-ray flux at 1 keV (as determined by Sherpa for bin sizes of 3, 5, and 7) for both the northwest and southeast radio lobes. Values for these are given in Table 20. The total flux density for the two lobes (summed together) is 1.198×10^{-15} erg cm^{-2} s^{-1} keV^{-1}. As with the radio emissions, we calculate the flux at a

[29]There is some confusion about the use of H in this method, since the Gursky & Schwartz (1977) use $H^2/8\pi$ in the denominator of their P_c/P_s equation. However, calculations, dimensional analysis, and comparison with equations from other papers indicate that it should actually be $B^2/2\mu_0$.

Table 20: Sherpa flux densities for NW and SE lobes; all values in erg cm^{-2} s^{-1} keV^{-1}

Region	Bin 3	Bin 5	Bin 7	Average
NW Lobe	5.810e-16	6.811e-16	6.934e-16	6.518e-16
SE Lobe	5.045e-16	5.581e-16	5.760e-16	5.462e-16

particular energy by the power law (using the same spectral index calculated earlier)

$$F_x = \left(1.198 \times 10^{-15} \text{erg cm}^{-2} \text{ s}^{-1}\right) E_x^{\alpha} \tag{21}$$

Combining Equations 19 and 20, we obtain an expression for the internal magnetic field:

$$B_{\text{int}} = 10^9 \sqrt{2\mu_0 a T^4 \frac{F_r \cdot \nu_r}{F_x \cdot E_x}} \text{ nT} \tag{22}$$

Since the ratio given by Gursky & Schwartz (1977) relies on equivalent inverse-Compton and synchrotron energies and frequencies, we stay as close to both the radio continuum data (Table 19) and the X-ray data (with an energy range of 0.3 keV to 8 keV) by using an X-ray energy of $E_x = 4$ keV and the corresponding synchrotron frequency of $v_r = 20$ MHz. With these values, we calculate the inverse-Compton radiation to synchrotron ratio (P_c/P_s) and the internal magnetic field (B_{int}) to be $P_c/P_s \approx 0.0275$ (Equation 20), which corresponds to an internal magnetic field of $B_{\text{int}} \approx 19.2$ μG, or $B_{\text{int}} = 1.92$ nT (Equation 22).

4.4.2. *Method 1b: Govoni & Feretti (2004)*

As previously mentioned, one method of calculating the minimum energy field is derived in Section 3.2 of Govoni & Feretti (2004) and is given in Equation 26 as:

$$B_{\text{me}} = 10^5 \left(\frac{24\pi}{7} u_{\text{min}}\right)^{1/2} \text{ nT} \tag{23}$$

where B_{me} is in units of nanoteslas and u_{min} is the energy density of the magnetic field. The energy density defined in units of erg cm^{-3} in Equation 25 of Govoni & Feretti (2004) as:

$$u_{\text{min}} = \xi(\alpha', \nu_1, \nu_2)(1+K)^{4/7}(\nu_0)^{4\alpha'/7}(1+z)^{(12+4\alpha')/7} \left(\frac{F_0}{\theta_x \theta_y d}\right)^{4/7} \tag{24}$$

where z is the redshift, F_0 is the flux density in mJy at a frequency of ν_0 (in MHz), θ_x and θ_y are the angular sizes (in arcseconds) of the emitting region, d is the depth of the radio lobes along our line of sight, α' is the positive spectral index of the radio continuum (such that $\alpha' \equiv -\alpha$ when α is the spectral index convention used in this thesis), and $\xi(\alpha', \nu_1, \nu_2)$ is a constant that depends on the spectral index and a frequency range of synchrotron emission. For this analysis, we define the emitting region to be the sum of the NW and SE radio lobes, which allows us to calculate the average equipartition magnetic field strength ($B_{\rm me}$). Here, we assume a range of 10 MHz - 10 GHz. Values of ξ are given in Table 1 of Govoni & Feretti (2004). We assume that the ratio K of heavy, non-radiating relativistic particles (e.g. protons) to electrons is zero and that the size of the radio lobes along our line of sight is approximately that of the shorter dimension of the projected area we see such that $d = 25.8$ kpc.[30] For the constant ξ, we use the value that corresponds to a positive spectral index of $\alpha' = 0.9$ and a frequency range of $\nu_1 = 10$ MHz to $\nu_2 = 10$ GHz. Using a redshift of $z = 0.685$, angular sizes of $\theta_x = 4.86''$ and $\theta_y = 3.60''$, and a flux density of 64.9 Jy at a frequency of 17.8 MHz, we calculate the minimum energy of the magnetic field in the 3C 220.3 radio lobes to be $B_{\rm me} = 4.19$ nT (see summary in Table 21). This equipartition field value is a factor of ~ 3 above the internal field value calculated in Method 1a.

4.4.3. *Method 2: Miley (1980)*

Miley (1980) gives a second method of determining both the minimum energy field ($B_{\rm me}$) and the internal magnetic field ($B_{\rm int}$) of 3C 220.3. The equipartition field is determined by the geometry of the radio lobes, the redshift, the radio spectral index, and the synchrotron radio flux. Equation 2 in Miley (1980) defines the minimum energy field as:[31]

$$B_{\rm me} = 5.69 \left(\frac{1+K}{\eta} (1+z)^{3-\alpha} \frac{1}{\theta_x \theta_y s \sin^{3/2}\phi} \frac{F_0}{\upsilon_0^{\alpha}} \frac{\nu_2^{\alpha+1/2} - \nu_1^{\alpha+1/2}}{\alpha + 1/2} \right)^{2/7} \text{nT} \qquad (25)$$

[30] Calculated using Ned Wright's Cosmology Calculator (Wright 2006) and adopting a standard ΛCDM cosmology with $H_0 = 70.0$ km s^{-1} Mpc^{-1}, $\Omega_\Lambda = 0.721$, and $\Omega_m = 0.279$ (Bennett et al. 2013).

[31] For convenience, the equation for $B_{\rm me}$ has been converted from its original units of gauss to units of nanoteslas.

where z is the redshift of the source, θ_x and θ_y are the angular sizes (in arcseconds) of the emitting region, s is the size of the lobe along our line-of-sight in kpc (which we assume to be equal to the smaller dimension of the summed radio lobe in the plane of the sky), F_0 is the flux density (in Jy) at a frequency of ν_0 (in GHz), ν_1 and ν_2 are the lower and upper limits of the radio spectrum (also in GHz), and α is the spectral index of the radio spectrum. $B_{\rm me}$ is in units of nanoteslas. We take the ratio between the energy of the heavy non-radiating particles to the radiating electrons in the radio lobes to be $K = 0$ and the volume filling factor of the particles in the radio lobes to be $\eta = 1$. Using a redshift of $z = 0.685$, angular size of $\theta_x = 4.86''$ by $\theta_y = 3.60''$, line-of-sight size of $s = 25.8$ kpc,[32] flux density at 64.9 Jy at a frequency of 17.8 MHz, and spectral index of $\alpha = -0.9$ for $\nu_1 = 5$ MHz to $\nu_2 = 10$ GHz, we calculate the minimum energy field of 3C 220.3 to be $B_{\rm me} = 4.87$ nT (see summary in Table 21).

To estimate the internal magnetic field, we used Equation 5 from Miley (1980), which is in itself an approximation of a formulation in Harris & Grindlay (1979). As with the $B_{\rm int}$ approximation in Gursky & Schwartz (1977), this calculation also uses the ratio of X-ray to radio fluxes (i.e. inverse-Compton scattering to synchrotron radiation):[33]

$$B_{\rm int} = 10^5 \left[6.6 \times 10^{-40} (4800)^{\alpha} (1+z)^{3-\alpha} \frac{F_r}{F_x} \left(\frac{E_x^{\alpha}}{\nu_r^{\alpha}} \right) \right]^{1/(1-\alpha)} \ {\rm nT} \qquad (26)$$

where F_r is the radio flux density (in Jy) at a frequency of ν_r (in GHz) and F_x is the X-ray flux density (in erg cm^{-2} s^{-1} Hz^{-1}) at an energy of E_x (in keV). $B_{\rm int}$ is in units of nanoteslas. Flux densities for different X-ray and radio energies may be used, since the equation has a power law correction for the frequencies (i.e. the $E_x^{\alpha}/\nu_r^{\alpha}$ factor). As before, we use a redshift of $z = 0.685$, spectral index of -0.9, and $F_r = 64.9$ Jy at $\nu_r = 17.8$ MHz. We use the (converted) X-ray flux density of 1.198×10^{-15} erg cm^{-2} s^{-1} keV^{-1} at $E_x = 1$ keV (discussed

[32]Calculated using Ned Wright's Cosmology Calculator (Wright 2006) and adopting a standard ΛCDM cosmology with $H_0 = 70.0$ km s^{-1} Mpc^{-1}, $\Omega_\Lambda = 0.721$, and $\Omega_m = 0.279$ (Bennett et al. 2013).

[33]For convenience, the equation for $B_{\rm int}$ has also been converted from its original units of gauss to units of nanoteslas.

in Method 1a). The resulting internal magnetic field is $B_{\rm int} = 1.69$ nT (see summary in Table 21). Compared to its minimum energy counterpart for this method ($B_{\rm me} = 4.87$ nT), Method 2 is consistent with Method 1 in that the magnetic field of 3C 220.3 is a factor of ~ 3 below the equipartition field.

4.4.4. *Method 3: Worrall (2009)*

A more sophisticated method for calculating the internal and minimum energy field for a source is described in Worrall (2009) and Worrall & Birkinshaw (2006). As before, the minimum energy field is calculated only through the synchrotron emissions, while the internal magnetic field of the lobe is determined through a ratio of inverse-Compton scattering off CMB photons (i.e. X-ray emissions) to synchrotron (i.e. radio emissions). Since this method defines the radio spectral index as a positive number (opposite of the convention used in Method 2), we define $\alpha' \equiv -\alpha$ to avoid confusion.

For the minimum energy field calculation, we use Equation 57 in Worrall & Birkinshaw (2006):[34]

$$B_{\rm me} = 10^9 \left[\frac{(\alpha'+1)C_1}{2C_2} \frac{1+K}{\eta V} L_\nu \nu^{\alpha'} \frac{\gamma_{\rm max}^{1-2\alpha'} - \gamma_{\rm min}^{1-2\alpha'}}{1-2\alpha'} \right]^{1/(\alpha'+3)} \quad \text{nT} \tag{27}$$

As in Method 2, K is the ratio of non-radiating heavy particles to radiating electrons and η is the volume filling factor in the radio lobes. L_ν is the luminosity of the radio lobes at a synchrotron emission frequency of ν. However, rather than integrating over a range of synchrotron emission frequencies, this method integrates over an assumed electron energy distribution. L_ν is defined as:

$$L_\nu = (1+z)^{\alpha'-1} F_\nu 4\pi D_L^2 \tag{28}$$

where F_ν is the radio flux density and D_L is the luminosity distance of the source in meters (Worrall 2019, private communication).

[34]For convenience, the equation for $B_{\rm me}$ has also been converted from its original units of gauss to units of nanoteslas.

The volume V is defined for an equivalent spherical approximation as:

$$V = \frac{4}{3}\pi\theta^3 \left(\frac{D_L}{(1+z)^2}\right)^3 \tag{29}$$

where θ is the equivalent angular size of the summed radio lobes (in radians) and D_L is the luminosity distance (in meters).

The $\gamma_{\rm max}$ and $\gamma_{\rm min}$ terms are the minimum and maximum Lorentz factors for the synchrotron electrons and are related to their energy and frequency in Worrall & Birkinshaw (2006) by:

$$\gamma = \frac{E}{m_e c^2} = \frac{h\nu}{m_e c^2} \tag{30}$$

where h is Planck's constant, ν is the frequency of the synchrotron radiation from the electron, m_e is the mass of the electron, and c is the speed of light.

The coefficients C_1 and C_2 are defined in Worrall (2019, private communication) as:

$$C_1 = \left(\frac{c}{r_e F(\alpha')}\right)\left(\frac{\nu_g}{B_{\rm int}}\right)^{-(\alpha'+1)} \tag{31}$$

$$C_2 = \frac{u_B}{B_{\rm int}^2} \tag{32}$$

where r_e is the classical electron radius, ν_g is the gyration frequency of a synchrotron electron in a magnetic field, $B_{\rm int}$ is the internal magnetic field of the lobe, and u_B is the magnetic field energy density. The gyration frequency ν_g is defined in Worrall (2009) to be:

$$\nu_g = \frac{eB_{\rm int}}{2\pi m_e} \tag{33}$$

where e is the charge of the electron, $B_{\rm int}$ is the magnetic field, and m_e is the mass of the electron. As mentioned in Equation 6 of Worrall (2009), an electron with a Lorentz factor of γ then radiates at a frequency of:

$$\nu_e = \gamma^2 \nu_g \tag{34}$$

Using the definition of the gyration frequency (Equation 33), Equation 32 can be further simplified to:

$$C_1 = \left(\frac{c}{r_e F(\alpha')}\right)\left(\frac{e}{2\pi m_e}\right)^{-(\alpha'+1)} \tag{35}$$

Similarly, since the energy density is defined as $u_B = B_{\text{int}}^2/2\mu_0$, Equation 32 becomes:

$$C_2 = \frac{1}{2\mu_0} \tag{36}$$

The function $F(\alpha')$ in the coefficient C_1 is also defined in Worrall (2019, private communication) as:

$$F(\alpha') = \frac{3^{(2\alpha'+1)/2}2\pi}{2\alpha'+2}\Gamma\left(\frac{3\alpha'+11}{6}\right)\Gamma\left(\frac{3\alpha'+1}{6}\right)\frac{\sqrt{\pi}\Gamma[(\alpha'+3)/2]}{2\Gamma[(\alpha'+4)/2]} \tag{37}$$

where Γ is the standard gamma function.

For our approximation, we take the ratio of non-radiating heavy particles to radiating electrons to be $K = 0$, the volume filling factor to be $\eta = 1$, and the range of electron energies (in terms of Lorentz factors) to be $\gamma_{\text{min}} = 10$ and $\gamma_{\text{max}} = 10^6$. Using the previously-calculated internal magnetic field of $B_{\text{int}} = 3.01$ nT, a spectral index of $\alpha' = 0.9$, a radio flux density of $F_\nu = 64.9$ Jy at $\nu = 17.8$ MHz, and an angular size of $\theta = 4.183\,''$, and a luminosity distance of $D_L = 4188.1$ Mpc,[35] we calculate the equipartition field to be $B_{\text{me}} = 6.35$ nT (see summary in Table 21).

For the internal magnetic field (B_{int}), we use a modified version of Equation 7 from Worrall (2009). The original version, which uses flux densities that correspond to a fixed frequency in the observer's frame (Worrall 2009), is as follows:

$$\frac{F_{\text{iC-CMB}}}{F_{\text{syn}}} = \frac{3}{4}\delta^{1+\alpha'}(1+z)^{3+\alpha'}\left(\frac{1+\cos\theta}{1+\beta}\right)^{1+\alpha'}\frac{u_{\text{CMB}}}{u_B}\left(\frac{\nu_{\text{CMB}}}{\nu_g}\right)^{\alpha'-1} \tag{38}$$

where $F_{\text{iC-CMB}}$ is the X-ray flux density from inverse-Compton scattering off the CMB, F_{syn} is the radio flux density from the synchrotron radiation, δ is the relativistic Doppler factor

[35]Calculated using Ned Wright's Cosmology Calculator (Wright 2006) for a redshift of $z = 0.685$ and adopting a standard ΛCDM cosmology with $H_0 = 70.0$ km s^{-1} Mpc^{-1}, $\Omega_\Lambda = 0.721$, and $\Omega_m = 0.279$ (Bennett et al. 2013).

of the emitting electrons that incorporates the orientation of the radio jets with respect to the observer (θ) and the speed of the source (βc), $u_{\rm CMB}$ is the energy density of the CMB, u_B is the energy density of the internal magnetic field, $\nu_{\rm CMB}$ is the peak frequency of the CMB, and ν_g is the gyration frequency (Equation 33).

Since the 3/4, δ, and $(1+\cos\theta)/(1+\beta)$ relate to the effects of anisotropies and relativistic beaming (Worrall 2019, private communication), we can set them equal to one, as we take their effects to be negligible in this case.[36] Thus, we have the resulting modified equation:

$$\frac{\nu_x^{\alpha'}}{\nu_r^{\alpha'}}\frac{F_{\text{iC-CMB}}}{F_{\rm syn}} = (1+z)^{3+\alpha'}\left(\frac{u_{\rm CMB}}{u_B}\right)\left(\frac{\nu_{\rm CMB}}{\nu_g}\right)^{\alpha'-1} \tag{39}$$

We also add an additional factor of $\nu_x^{\alpha'}/\nu_r^{\alpha'}$ (Worrall 2019, private communication), which is a power law correction for the different X-ray and radio frequencies of the flux densities we used (as discussed in Method 2). The energy density of the CMB is defined as $u_{\rm CMB} = aT^4$ (where a is the radiation density constant and T is the temperature of the CMB) and the energy density of the magnetic field is defined as $u_B = B^2/2\mu_0$ (as discussed in Method 1a). Using the definition of the gyration frequency (Equation 33), we can rewrite Equation 39 as:

$$\left(\frac{\nu_x^{\alpha'}}{\nu_r^{\alpha'}}\right)\frac{F_{\text{iC-CMB}}}{F_{\rm syn}} = (1+z)^{3+\alpha'}\left(\frac{aT^4}{B_{\rm int}^2/2\mu_0}\right)\left(\frac{\nu_{\rm CMB}}{eB_{\rm int}/2\pi m_e}\right)^{\alpha'-1} \tag{40}$$

Solving for $B_{\rm int}$ gives us:[37]

$$B_{\rm int} = 10^9\left[\left(\frac{\nu_x^{\alpha'}}{\nu_r^{\alpha'}}\right)\frac{F_{\text{iC-CMB}}}{F_{\rm syn}}\frac{(1+z)^{-(3+\alpha')}}{2\mu_0 aT^4}\left(\frac{2\pi m_e\nu_{\rm CMB}}{e}\right)^{1-\alpha'}\right]^{-1/(1+\alpha')} \text{ nT} \tag{41}$$

For convention, we take the peak frequency of the CMB as $\nu_{\rm CMB} = 282$ GHz and the temperature of the CMB as $T = 2.7$ K. For 3C 220.3, we use the following parameters: a redshift of $z = 0.685$, spectral index of $\alpha' = 0.9$, X-ray flux density of $F_{\text{iC-CMB}} = 1.198\times10^{-15}$ erg cm^{-2} s^{-1} keV^{-1} at an X-ray energy of $E_x = 1$ keV, and radio flux density of $F_{\rm syn} = 64.9$

[36]Regarding the relativistic Doppler factor, we assume that there is no relativistic motion (i.e. $\delta = 1$) in the radio lobes since the plasma has slowed down and is no longer in a jet.

[37]For convenience, the equation for $B_{\rm int}$ has also been converted from its original units of gauss to units of nanoteslas.

Jy at a frequency of $\nu_r = 17.8$ MHz. The resulting internal magnetic field is 2.92 nT (see summary in Table 21). Compared to the calculated equipartition field of $B_{\rm me} = 6.35$ nT, this is consistent with the conclusions of Method 1 and Method 2, in that the magnetic field of 3C 220.3 is a factor of $\sim 2-3$ below the equipartition field.

4.4.5. *Summary of Magnetic Field Calculations*

As seen in Table 21, the three methods presented above all indicate that the magnetic field of the radio lobes of 3C 220.3 is not at minimum energy. In both Methods 2 and 3, the internal field is a factor of roughly 3 or 2 smaller than the equipartition field, respectively. The discrepancies in these numbers most likely originate from the varying assumptions and approximations that resulted in the different formulations. As previously mentioned, Method 1 (Gursky & Schwartz 1977) uses a simple ratio of X-ray to radio fluxes for a single electron energy. There is no consideration of the redshift, distance, or the spectrum and full energy range of the emission of the radio lobes, which affect the radiation of the iC-CMB scattering.

The formulations in Method 2 (Miley 1980) and Method 3 (Worrall 2009; Worrall & Birkinshaw 2006) are similar. Both account for the source size and redshift and integrate over a range of the synchrotron emission spectrum. However, while Method 2 has several pre-calculated constants in Equation 25 and 26, Method 3 is more generalized and includes relativistic effects. Unlike Method 2, which integrates over the synchrotron frequencies that result from a certain electron energy range, the Method 3 integrates directly over the electron

Table 21: Calculated $B_{\rm int}$ and $B_{\rm me}$ values

Method	$B_{\rm int}$	$B_{\rm me}$
Gursky & Schwartz	1.48 nT	
Govoni & Feretti		4.19 nT
Miley	1.69 nT	4.87 nT
Worrall	2.92 nT	6.35 nT

energies (in the form of their Lorentz factors), staying closer to the actual physics of the system.

While many radio sources have been observed to have equipartition fields that are a factor of a few lower than their equipartition field (Croston et al. 2005; Wilkes et al. 2012), it is useful to discuss the disagreement between the calculated $B_{\rm int}$ and $B_{\rm me}$ fields for 3C 220.3. Our uncertainties for the $B_{\rm me}$ calculations come from several main assumptions. First, we assume that the relativistic particles radio lobes are entirely composed of electrons (i.e. $K = 0$), rather than being some mix of heavy, non-radiating particles like protons. We also assume that volume of the radio lobes is completely filled by the magnetic field (i.e. $\eta = 0$). However, both of these assumptions minimize the equipartition fields in Methods 2 and 3 (Equations 25 and 27), and the disagreement between $B_{\rm int}$ and $B_{\rm me}$ would actually *increase* if $K > 0$ or $\eta < 1$. If, on the other hand, the range of integration over the electron energies or synchrotron frequencies was increased, the equipartition field would decrease and could be brought into agreement with the calculated internal field.

Other uncertainties in our calculations of the equipartition fields stem from our volume approximation. In Method 2, we approximate the line-of-sight size (s) of the summed radio lobes to be equal to the smaller dimension of the lobes in the plane of the sky. In Method 3, we approximate the summed lobes as a sphere with an equivalent volume (V) of an ellipsoid with the line-of-sight size equal to the smaller sky-plane dimension. Since the volume is on the denominator of the equations for the equipartition field in both Equations 25 and 27, the assumption of the smallest volume would cause an overestimation of the field strength. Although another uncertainty may lie in the calculation of the power law slope for the radio and X-ray fluxes (particularly since there appears to be a turnover at low frequencies in the radio data), there error in the slope is fairly small and likely does not drastically affect the calculations.

Overall, since the equipartition fields and internal fields differ by a factor of only $\sim 2-3$, the disagreement is well within the range of observed $B_{\rm me}/B_{\rm int}$ ratios and the field strengths

given in Table 21 seem to be reasonable. Figure 27 shows the predicted X-ray fluxes based off the calculated $B_{\rm int}$ and $B_{\rm me}$ values for our most sophisticated method (Method 3, Section 4.4.4). The predicted iC-CMB X-ray fluxes are determined by solving Equation 39 for $F_{\text{iC-CMB}}$ such that

$$F_{\text{iC-CMB}} = (1+z)^{3+\alpha'} \left(\frac{u_{\rm CMB}}{u_B}\right) F_{\rm syn} \left(\frac{\nu_r^{\alpha'}}{\nu_x^{\alpha'}}\right) \left(\frac{\nu_{\rm CMB}}{\nu_g}\right)^{\alpha'-1} \tag{42}$$

In Figure 27, we can see that the stronger equipartition field predicts lower X-ray fluxes than we actually observe.

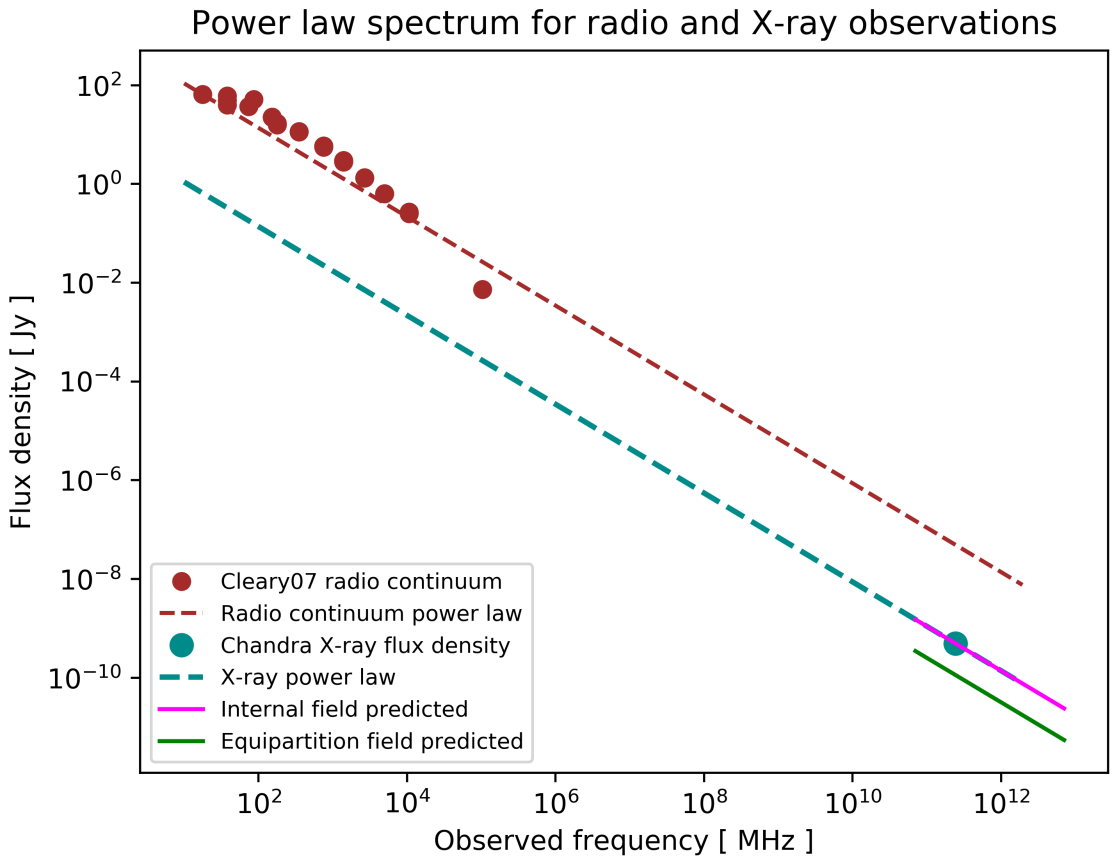

Figure 27: Plot showing the parallel power laws with spectral index $\alpha = -0.9$ for the radio and X-ray fluxes that correspond to the synchrotron radiation and inverse-Compton scattering in the radio lobes of 3C 220.3. The single X-ray point (turquoise) corresponds to the calculated flux at 1 keV (listed in Table 20). The radio continuum data (brown) are drawn from the compilation by Leung & Riechers (2016) (listed in Table 19). The pink line shows the predicted X-ray fluxes (from 0.5 - 8 keV) based on the internal magnetic field ($B_{\rm int} = 2.92$ nT) calculated in Method 3 (Section 4.4.4). The green line shows the predicted X-ray fluxes (from 0.5 - 8 keV) based on the equipartition magnetic field ($B_{\rm me} = 6.35$ nT) calculated in the same method.

5. CONCLUSIONS

Gravitational lensing systems are always of interest, as they give clues about the mass distributions and dark matter contents of objects and regions in our universe. Since lensing magnifies the source objects, the phenomenon also allows us to study very faint, high-redshift sources that we would otherwise not be able to study in such detail. Submillimeter galaxies are one type of source, and the strongly lensed SMMJ0939 in the 3C 220.3 system provides an excellent opportunity to analyze a member of a typically elusive class of objects. The primary lens, 3C 220.3, is also a powerful radio galaxy, which allows us to study its magnetic field (in the radio lobes), its dark matter content, and its relation to source B.

3C 220.3 was discovered to be a gravitational lens by a *Herschel* survey and was the subject of an extensive analysis by Haas et al. (2014). Since then, we have obtained deeper data from *Chandra* and additional observations with *HST* in three different filters. Focusing on the newer data, this follow-up analysis of the 3C 220.3 system is many-fold: (1) to calculate the X-ray and optical fluxes for the various components of the galaxy system (Chapter 3), (2) to model the spectral energy distribution in order to calculate stellar mass of 3C 220.3 and source B (Section 4.2), (3) to model the X-ray and radio emission and determine the magnetic field properties of the radio lobes (Section 4.4), and (4) to reconstruct the lensed SMG via lens modeling with the more recent *HST* and *Chandra* data (Section 4.3). The conclusions of our analysis are given below.

1. **New *Chandra* and *HST* Data** — The deeper *Chandra* and *HST* data from 2014 have given us new insights into the fascinating 3C 220.3 system (Chapters 2 and 3). First, the newer *HST* data reveal a full Einstein ring of the lensed SMG in all three filters (F606W, F814W, F160W), while only an arc was visible in the archival data. Second, with sub-pixel binning, the recent *Chandra* data seem to show a ring-like structure that overlaps (spatially) with the Einstein ring visible in the HST exposures, which would support the hypothesis from Haas et al. (2014) and Leung & Riechers

(2016) that SMMJ0939 is transitioning from a starburst phase to an unobscured quasar phase. More analysis needs to be done to determine if this ring-like structure is more than diffuse emission from the 3C 220.3 galaxy. The X-ray observations also have counts that coincide with the location of source B in the *HST* exposures, which suggests that it could also have an AGN. If source B does have the same redshift as 3C 220.3, the two could form a binary quasar system. Finally, there is a diffuse, extended X-ray emission from 3C 220.3 that encompasses all components of the system. This is unusual for a source and makes it challenging to identify which X-rays originate from which components, even with this long, 198 ks exposure.

2. **New X-Ray and Optical Fluxes** — With the new *Chandra* and *HST* data, we defined count-extraction regions for the components of the 3C 220.3 system (Table 5). In the X-ray analysis, we calculated hardness ratios for each region (Section 3.2) and fluxes for each component (Section 3.3). The hardness ratios and fluxes are listed in Tables 6 and 11, respectively. We used the same regions for the optical flux calculations (Section 3.5), which are listed in Table 16.

3. **Updated SED** — Using the optical and X-ray fluxes we calculated in Chapter 3, we were able to construct updated SED plots (Section 4.1) of the full 3C 220.3 system. Although there are some discrepancies between the *HST* F702W fluxes and the fluxes that we calculated for the F606W, F814W, and F160W filters, the new observations have allowed us to better define the SED components of source B and SMMJ0939. Blackbody restframe temperature calculations of 3C 220.3 (source A), source B, and the SMG are $T_{A,\mathrm{rest}} \sim 4430$ K, $T_{B,\mathrm{rest}} \sim 4340$ K, and $T_{\mathrm{SMG,rest}} \sim 8570$ K, respectively. These calculations provide new and previously unknown values for the sources. Additional work will be done to understand the disagreement between the F702W fluxes and our measurements and to calculate the overall bolometric luminosity for the 3C 220.3 system and its components.

4. **Stellar Mass Determinations** — Stellar mass determinations of 3C 220.3 (source A) and source B were done with the FAST SED code (Kriek et al. 2009) using the fluxes from three 2014 *HST* observations (Section 4.2). The stellar masses of the two sources were calculated to be $M_A^* \sim \left(1.1^{+17}_{-0.17}\right) \times 10^{10} M_\odot$ and the stellar mass of source B to be $M_B^* \sim \left(5.4^{+90}_{-1.1}\right) \times 10^9 M_\odot$. These are lower than the masses calculated by Haas et al. (2014) since the higher fluxes in the F702W band were excluded from the fit. However, since Haas et al. (2014, Section 5) consider their mass determinations for source A and B to upper limits, our calculated masses are fully consistent with those reported in Haas et al. (2014). For these calculations, the redshift of source B was assumed to be equal to that of 3C 220.3. Further work will be done to attempt to determine the redshift of the source using the EAZY photometric redshift code (Brammer et al. 2008). Using the total masses of sources A and B from Haas et al. (2014), preliminary dark matter fractions of the two sources are $f_A \sim 0.97^{+0.01}_{-0.48}$ and $f_B \sim 0.96^{+0.01}_{-0.75}$.

5. **Flux Ratios and Magnetic Field Strengths** — Using the X-ray fluxes determined in Chapter 3 and radio fluxes collected from the literature, we considered three methods of increasing sophistication for calculating the strengths of the equipartition and internal magnetic fields of the radio lobes of 3C 220.3 (Section 4.4). All three methods indicate that the magnetic field of the lobes is a factor of $\sim 2-3$ lower than the equipartition field, with a $B_{\rm int} \approx 1.5 - 3.0$ nT. These calculations are a new addition to the existing literature on 3C 220.3, as well as the ongoing work of understanding the relationship between the equipartition field approximation to the internal magnetic field strength of radio lobes. However, since these measurements considered the entire emitting region of the radio lobes (i.e. the average of the NW and SE lobes), more work should be done to calculate the magnetic field strengths of the individual lobes and possibly even the hotspots. Future work should also include ratios of optical and

X-ray fluxes to determine in which regions photoionization or collisional ionization is dominant.

6. **Updated Lens Modeling** — The lens modeling is currently underway with the additional *HST* and *Chandra* data and we are awaiting the updated model from our collaborator. The reconstructed image of SMMJ0939 and the calculated masses of 3C 220.3 and source B from the modeling will be incorporated once they are available. Since the 2014 *HST* data show a full Einstein ring rather than the partial arc seen in the archival *HST* data, it is possible the updated image will show UV emission spread around the SMG, rather than being concentrated in a single area.

Between a powerful radio galaxy, an Einstein ring of a lensed submillimeter galaxy, and an additional galaxy of unknown redshift, the 3C 220.3 system invites questions and analyses from all different angles. Recent, deeper data from the *Chandra X-Ray Observatory* and the *Hubble Space Telescope* have contributed significant information to our knowledge of the system, but many intriguing questions remain. What is the true redshift of source B? Does it comprise a binary quasar system with 3C 220.3, or does it lie in the foreground or background of the radio galaxy? Why is there diffuse X-ray emission from the system? Time will tell, but for now, the enigmatic 3C 220.3 system retains many mysteries that are yet to be uncovered.

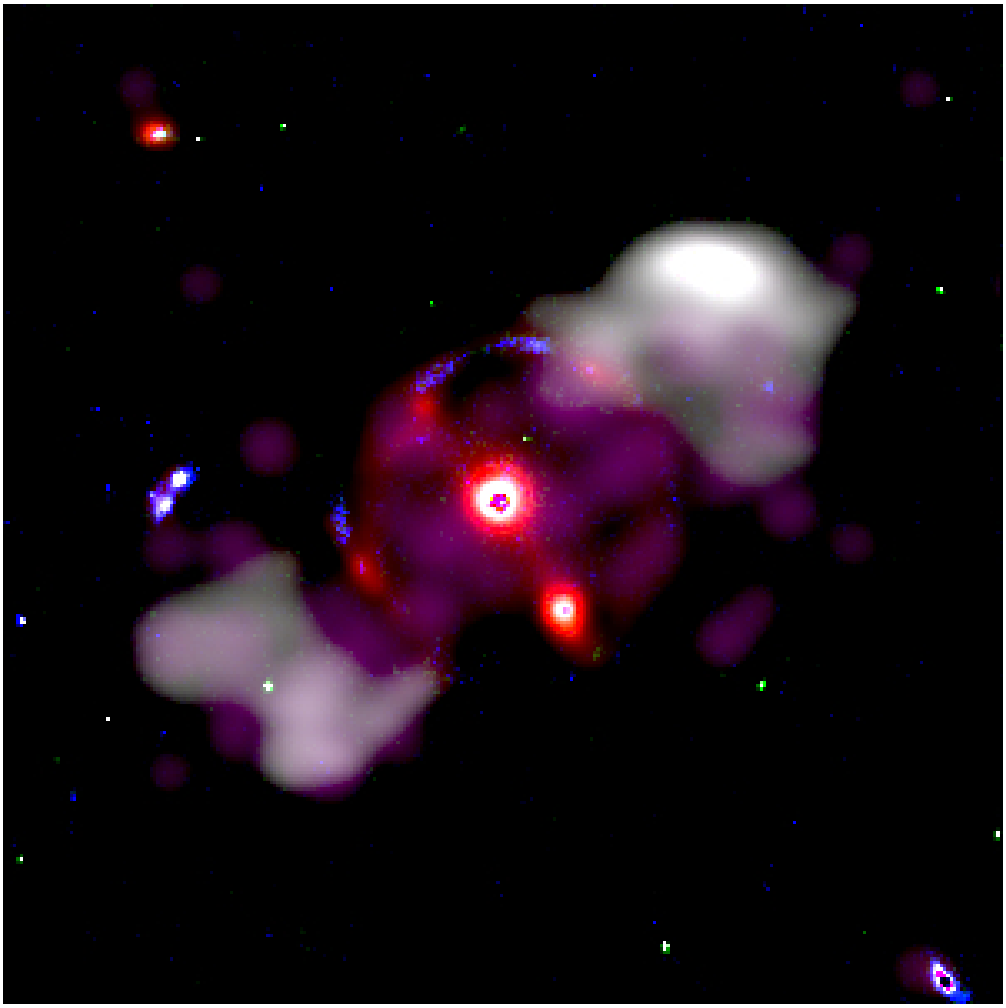

Figure 28: A new, composite-color look at the 3C 220.3 system. JVLA radio data are shown in white, *HST* F160W, F814W, and F606W exposures are shown in red, green, and blue (respectively), and the smoothed *Chandra* observations are shown in purple.

REFERENCES

Antonucci, R. 1993, Annual Review of Astronomy and Astrophysics, 31, 473

Arnaud, K., Smith, R., & Siemiginowska, A. 2011, Handbook of X-ray Astronomy

Barnacka, A. 2018, PhR, 778, 1

Bennett, A. S. 1962, Memoirs of the Royal Astronomical Society, 68, 163

Bennett, C. L., Larson, D., Weiland, J. L., et al. 2013, The Astrophysical Journal Supplement Series, 208, 20

Bertoldi, F., Menten, K. M., Kreysa, E., Carilli, C. L., & Owen, F. 2000, arXiv e-prints, astro

Blain, A. W., Smail, I., Ivison, R. J., Kneib, J. P., & Frayer, D. T. 2002, PhR, 369, 111

Brammer, G. B., van Dokkum, P. G., & Coppi, P. 2008, ApJ, 686, 1503

Bruzual, G., & Charlot, S. 2003, MNRAS, 344, 1000

Calzetti, D., Armus, L., Bohlin, R. C., et al. 2000, ApJ, 533, 682

Cardelli, J. A., Clayton, G. C., & Mathis, J. S. 1989, ApJ, 345, 245

Chabrier, G. 2003, Publications of the Astronomical Society of the Pacific, 115, 763

Chapman, S. C., Blain, A. W., Smail, I., & Ivison, R. J. 2005, ApJ, 622, 772

Cleary, K., Lawrence, C. R., Marshall, J. A., Hao, L., & Meier, D. 2007, ApJ, 660, 117

Conroy, C., Gunn, J. E., & White, M. 2009, ApJ, 699, 486

Croston, J. H., Hardcastle, M. J., Harris, D. E., et al. 2005, ApJ, 626, 733

Dickey, J. M., & Lockman, F. J. 1990, Annual Review of Astronomy and Astrophysics, 28, 215

Dodelson, S. 2017, Gravitational Lensing

Edge, D. O., Shakeshaft, J. R., McAdam, W. B., Baldwin, J. E., & Archer, S. 1959, Memoirs of the Royal Astronomical Society, 68, 37

Einstein, A. 1936, Science, 84, 506

Fanaroff, B. L., & Riley, J. M. 1974, MNRAS, 167, 31P

Freeman, P., Doe, S., & Siemiginowska, A. 2001, in Proc. SPIE, Vol. 4477, Astronomical Data Analysis, ed. J.-L. Starck & F. D. Murtagh, 76–87

Fruscione, A., McDowell, J. C., Allen, G. E., et al. 2006, in Proc. SPIE, Vol. 6270, Society of Photo-Optical Instrumentation Engineers (SPIE) Conference Series, 62701V

Gandhi, P. 2005, Asian Journal of Physics, 13, 90

Garmire, G. P., Burrows, D., Feigelson, E., et al. 1986, in Society of Photo-Optical Instrumentation Engineers (SPIE) Conference Series, Vol. 597, X-ray instrumentation in astronomy, ed. J. L. Culhane, 261–266

Giacconi, R., Gursky, H., Paolini, F. R., & Rossi, B. B. 1962, PhRvL, 9, 439

Giacconi, R., Kellogg, E., Gorenstein, P., Gursky, H., & Tananbaum, H. 1971, ApJ, 165, L27

Giacconi, R., Branduardi, G., Briel, U., et al. 1979, ApJ, 230, 540

Govoni, F., & Feretti, L. 2004, International Journal of Modern Physics D, 13, 1549

Gursky, H., & Schwartz, D. A. 1977, Annual Review of Astronomy and Astrophysics, 15, 541

Haas, M., Leipski, C., Barthel, P., et al. 2014, ApJ, 790, 46

Hardcastle, M. J., & Worrall, D. M. 1999, MNRAS, 309, 969

Harris, D. E., & Grindlay, J. E. 1979, MNRAS, 188, 25

Hewish, A., & Ryle, M. 1955, Memoirs of the Royal Astronomical Society, 67, 97

Hewitt, J. N., Turner, E. L., Schneider, D. P., Burke, B. F., & Langston, G. I. 1988, Nature, 333, 537

Holland, W. S., Robson, E. I., Gear, W. K., et al. 1999, MNRAS, 303, 659

Ishibashi, W., & Courvoisier, T. J. L. 2010, A&A, 512, A58

Jones, M. H., Lambourne, R. J. A., & Serjeant, S. 2015, An Introduction to Galaxies and Cosmology
Kembhavi, A. K., & Narlikar, J. V. 1999, Quasars and active galactic nuclei : an introduction
Kriek, M., & Conroy, C. 2013, ApJ, 775, L16
Kriek, M., van Dokkum, P. G., Labbé, I., et al. 2009, ApJ, 700, 221
Kroupa, P. 2002, Science, 295, 82
Laing, R. A., Riley, J. M., & Longair, M. S. 1983, MNRAS, 204, 151
Leung, T. K. D., & Riechers, D. A. 2016, ApJ, 818, 196
Lilly, S. J., & Longair, M. S. 1984, MNRAS, 211, 833
Maraston, C. 2005, MNRAS, 362, 799
Miley, G. 1980, Annual Review of Astronomy and Astrophysics, 18, 165
Mills, B. Y., Little, A. G., Sheridan, K. V., & Slee, O. B. 2005, in Astronomical Society of the Pacific Conference Series, Vol. 345, From Clark Lake to the Long Wavelength Array: Bill Erickson's Radio Science, ed. N. Kassim, M. Perez, W. Junor, & P. Henning, 25–42
Mills, B. Y., & Slee, O. B. 1957, Australian Journal of Physics, 10, 162
Mills, B. Y., Slee, O. B., & Hill, E. R. 1958, Australian Journal of Physics, 11, 360
Noll, S., Pierini, D., Cimatti, A., et al. 2009, A&A, 499, 69
Norris, R. P. 2017, Nature Astronomy, 1, 671
Park, T., Kashyap, V. L., Siemiginowska, A., et al. 2006, ApJ, 652, 610
Rizzo, F., Vegetti, S., Fraternali, F., & Di Teodoro, E. 2018, MNRAS, 481, 5606
Rosswog, S., & Brüggen, M. 2007, Introduction to High-Energy Astrophysics
Rybicki, G. B., & Lightman, A. P. 1979, Radiative processes in astrophysics
Salpeter, E. E. 1955, ApJ, 121, 161
Shakeshaft, J. R., Ryle, M., Baldwin, J. E., Elsmore, B., & Thomson, J. H. 1955, Memoirs of the Royal Astronomical Society, 67, 106
Simpson, C., Rawlings, S., & Lacy, M. 1999, MNRAS, 306, 828
Spinrad, H., Djorgovski, S., Marr, J., & Aguilar, L. 1985, Publications of the Astronomical Society of the Pacific, 97, 932
Tacconi, L. J., Genzel, R., Smail, I., et al. 2008, ApJ, 680, 246
Truemper, J. 1990, Sterne und Weltraum, 29, 222
Vegetti, S., & Koopmans, L. V. E. 2009, MNRAS, 392, 945
Veron, P. 1977, The Messenger, 10, 12
Walcher, J., Groves, B., Budavári, T., & Dale, D. 2011, Ap&SS, 331, 1
Walsh, D., Carswell, R. F., & Weymann, R. J. 1979, Nature, 279, 381
Weisskopf, M. C., Tananbaum, H. D., Van Speybroeck, L. P., & O'Dell, S. L. 2000, in Society of Photo-Optical Instrumentation Engineers (SPIE) Conference Series, Vol. 4012, X-Ray Optics, Instruments, and Missions III, ed. J. E. Truemper & B. Aschenbach, 2–16
Westhues, C., Haas, M., Barthel, P., et al. 2016, AJ, 151, 120
White, S. D. M., & Rees, M. J. 1978, MNRAS, 183, 341
Wilkes, B. J., Lal, D. V., Worrall, D. M., et al. 2012, ApJ, 745, 84
Wilkes, B. J., Kuraszkiewicz, J., Haas, M., et al. 2013, ApJ, 773, 15
Wizinowich, P., Acton, D. S., Shelton, C., et al. 2000, PASP, 112, 315
Wizinowich, P. L., Le Mignant, D., Bouchez, A. H., et al. 2006, PASP, 118, 297
Worrall, D. M. 2009, Astronomy and Astrophysics Review, 17, 1
Worrall, D. M., & Birkinshaw, M. 2006, Multiwavelength Evidence of the Physical Processes in Radio Jets, ed. D. Alloin, 39
Wright, E. L. 2006, Publications of the Astronomical Society of the Pacific, 118, 1711
Zwicky, F. 1937, Physical Review, 51, 290